5-14-2023

MULTIFUNCTIONAL NANOCHANNEL WICKS FOR SURFACE WETTABILITY AND THERMAL MANAGEMENT

Durgesh Ranjan
Syracuse University

Abstract

Surface texturing to create artificially engineered surfaces is a well-researched field in heat transfer. Depending on the surface energy, further texturing can drastically alter the wettability to obtain hydrophobic, superhydrophobic, or hydrophilic surfaces. These properties can then be used in a variety of practical applications such as water harvesting through evaporation and condensation, self-cleaning properties, and thermal management of electronic chips. In this work, wettability features of nanochannel wicks are experimentally tested and explored for applications ranging from creation of robust slippery surfaces to cooling of electronic chip.

First, to advance dropwise condensation heat transfer, a process for creating a liquid infused surface (LIS) was developed; such surfaces have the ability to diminish the depletion of lubricant during condensation. The retention of silicon oil, used as a lubricant, was due to plasma treatment of the porous nanochannel sample prior to oil infusion, as well as strong capillarity because of the geometry of the nanochannels. While lower viscosity oil (5 cSt) provides high condensate drop mobility, it suffers faster depletion. So, 50 cSt was found to be a trade-off between drop mobility and oil depletion. Further, even the depleted LIS resulted in heat transfer coefficient (HTC) ~ 2.33 $kWm^{-2}K^{-1}$, which is ~ 162% improvement over flat silicon LIS. During condensation, rapid drop shedding on depleted nanochannel LIS with 50 cSt oil observed from little change in fraction of drops with diameter < 500 μm from ~ 98 % to only ~ 93 % after 4 hours of condensation. Durability of LIS was confirmed by total of 3 days of condensation on fresh LIS over an 18-day period. The sample still maintained the hydrophobic characteristic with a water contact angle ~104^{o} after 18 days.

In the next study, the porous nanochannel sample was treated and baked at high temperature with silicon oil, and subsequently depleted and coated with candle soot to obtain a superhydrophobic

surface (SHS). This SHS was then subjected to over 20 durability tests including extreme exposure to water (30 days submersion). Usually, a few days of water exposure or high humidity deteriorates the superhydrophobic surfaces, rendering them inappropriate for prolonged underwater applications. However, SHS fabricated in present study did not exhibit any significant degradation and remained superhydrophobic even after 5 months in open laboratory environment. Further, it demonstrated self-cleaning properties, organic compatibility (honey, soy sauce, chocolate syrup, all-purpose flour) and superoleophilicity, thus exhibiting potential real-world applications. Another feature of this SHS was its ability to restore superhydrophobicity from a forced degraded state.

Next, hydrophilic properties of porous nanochannels were explored in designing a solar flux-based vapor generation system. An unconventional approach to separate heating side and vapor generating side yielded significantly higher vapor generation rate ~ 1.18 $kgm^{-2}h^{-1}$ even in the absence of heat supply. Testing under solar heat flux of 1.25 sun resulted in vapor generation rate of 4.87 $kgm^{-2}h^{-1}$ at surface temperature below 35ºC. The flexibility of the system, in regard to the choice of energy source apart from solar flux, was shown by using a resistive heater on the heating side. The maximum vapor generation rate of 17.12 $kgm^{-2}h^{-1}$ was achieved with resistive heat input of 5.08 W at low temperature of 62°C. These findings could guide the vapor generation systems towards achieving higher vapor generation rate at low power and temperature thresholds.

In the later part of the work, performance of a device-scale nanochannel (122 nm depth and 10 µm width) based evaporator with FC72 as working fluid was demonstrated. FC72 is an ideal fluid for electronics cooling as it is nonpolar and dielectric with a low boiling point. The 1 mm thick evaporator provides a low form factor cooling solution desired in electronic cooling. The

steady-state wicking distance of FC72 in the nanochannels varied from 21 mm to 8 mm depending on the evaporator's working temperature. A new method to directly measure the evaporation of FC72 was developed to estimate the interfacial evaporative heat flux which eliminated the need for the contact angle measurement in nanochannels. The maximum evaporative heat flux was 0.93 $kWcm^{-2}$ at ~ 65 ºC hot spot temperature. Numerical simulations were performed to quantify the heat losses from different components of the evaporator arrangement. This study provides a systematic approach to design thin film evaporators while delineating important parameters to help develop effective thermal management strategies for high-performance electronics.

MULTIFUNCTIONAL NANOCHANNEL WICKS FOR SURFACE WETTABILITY AND THERMAL MANAGEMENT

by

Durgesh Ranjan

B.S., Cochin University of Science and Technology, 2017

M.S., Indian Institute of Technology Patna, 2019

DISSERTATION

Submitted in partial fulfillment of the requirements for the degree of

Doctor of Philosophy in Mechanical & Aerospace Engineering

Syracuse University

May 2023

Dedicated to my parents for their sacrifices, support, and endless love.

Acknowledgements

First, I express my sincere gratitude to my supervisor, Dr. Shalabh Maroo, for the continuous support, his patience, motivation, enthusiasm, and his active involvement and guidance. He has also been extremely helpful in research and even matters outside of academics. For his immense support and supervision throughout my Ph.D., I will always be grateful. Without his guidance and persistent help, this dissertation would not have been possible.

I am deeply grateful to the thesis committee members Dr. Ashok Sangani, Dr. Quinn Qiao, and Dr. Jianshun Zhang, for their support and valuable comments which helped to improve my dissertation.

I wish to thank Dr. An Zou for the insightful discussions and valuable feedbacks regarding sample fabrication and experiments. His fabrication of porous nanochannel samples was an integral part of my research work. I would like to offer my thanks to my research group members, Dr. Sajag Poudel, Maheshwar Chowdhary, and Ashok Thapa, with whom I performed my work in the Multiscale Research and Engineering Lab (MREL). They have unconditionally helped me during experiments and discussions.

Finally, I want to express my heartfelt gratitude to my family members for all the hardships they endured in order to provide a better life for me. I wish to thank my wife, Rashmi, who has always stood by me and given me all the help and support I have needed. I would like to thank all my teachers and mentors throughout my academic career. I thank all the faculties and staff of MAE Department, and people of MAE workshop as well as Syracuse University Administration for providing me all necessary facilities required for the successful completion of this dissertation.

Table of Contents

List of Figures

Chapter 1

Chapter 2

List of Tables

Chapter 1: Introduction

Heat transfer is governed by three basic modes, namely, conduction, convection, and radiation[1]. These are ubiquitous in nature and can be observed from their application in electricity generation to maintaining atmospheric temperature, which is essential for our survival. Depending on the number of phases (solid, liquid, gas) involved in the heat transfer process, it is denoted as single or multiphase heat transfer. The latter is primarily seen in condensation, evaporation, and boiling, and is considered an extremely efficient mode due to utilization of high latent heat resulting in better heat transfer performance[2]. Accordingly, multiphase heat transfer is widely used in various practical applications[1,3–8] such as refrigeration and air conditioning, thermal power plant, petrochemical industries, water purification, cooling of high-performance electronics, and micro/nano-scale thermal management, among others. It promises very high heat transfer coefficient (HTC) over single phase heat transfer. To further enhance the performance, numerous advancements have been made to modify the different components such as working fluid, working environment, and surfaces involved in heat transfer. Improvements in surfaces usually involves micro/nano scale texturing[9–11] of the surfaces where physical properties of the working fluid such as surface tension, viscosity and latent heat govern the mechanism of heat transfer. These techniques for enhancing heat transfer and thermal management are the new frontier in the heat transfer field. While the performance and heat generation in next-generation chips of computing equipment (Figure 1.1) are expected to plateau, Moore's law is currently predicting an increasing trend. This work also includes fabrication and testing of a nanochannel-based evaporator to improve the thermal management of electronic devices. Figure 1.2 shows the two types of nanochannel wicks used in this work: (a) nanochannels with micropores, which has been used to study condensation on liquid infused

surface, superhydrophobicity, and vapor generation, (b) nanochannels with microreservoirs, which has been used as an evaporator for thermal management of hot spot.

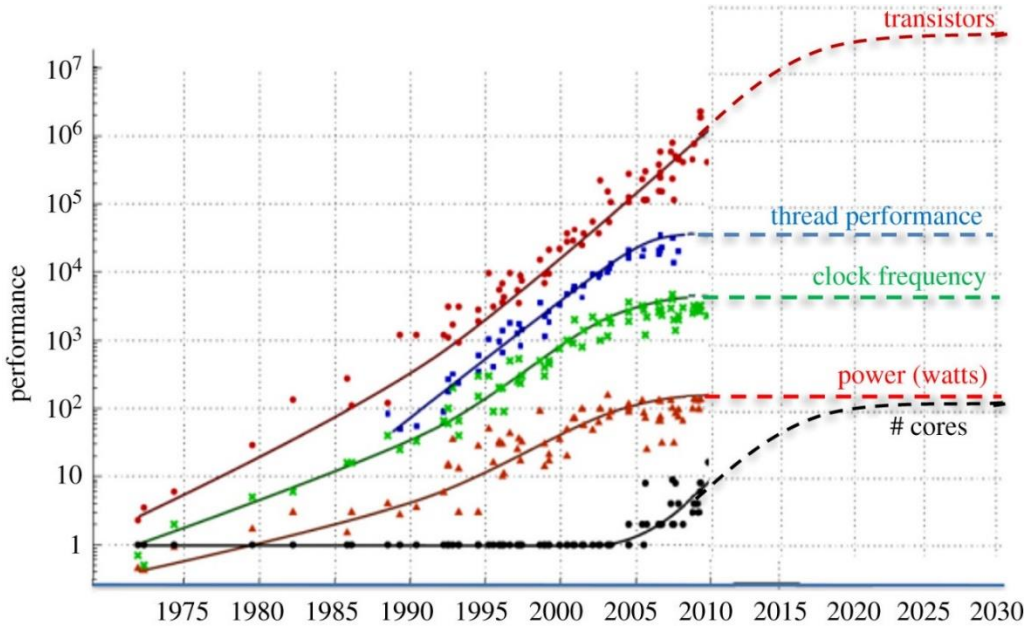

Figure 1.1. Sources of computing performance have been challenged by the end of Dennard scaling in 2004. All additional approaches to further performance improvements end in approximately 2025 due to the end of the roadmap for improvements to semiconductor lithography. Reprinted with permission from Shalf[12] *Copyright (2020) Royal Society.*

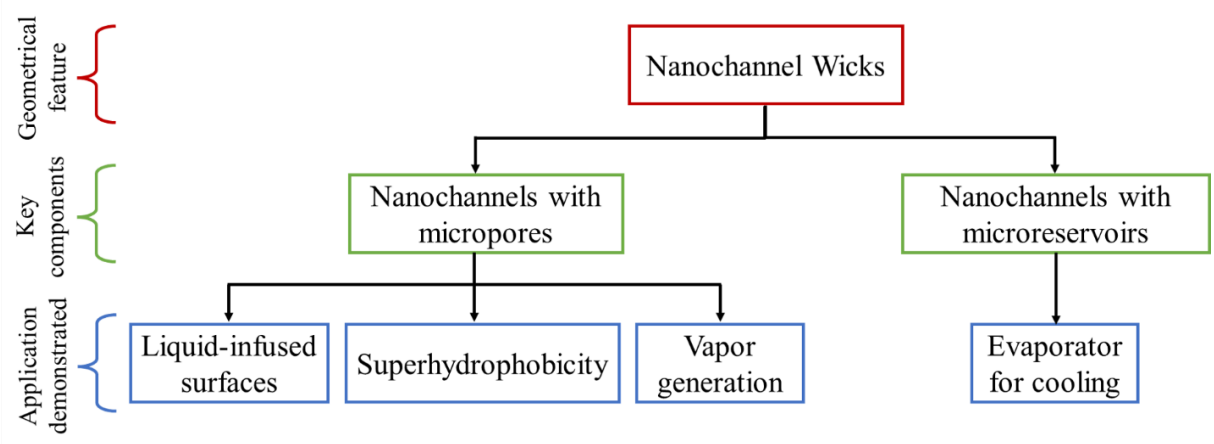

Figure 1.2. Types of surfaces used in the studies and their applications.

1.1 Motivation and Literature Review

1.1.1 **Condensation on Lubricant Infused Micro/Nano Structured Surfaces**

In case of condensation, surface wettability plays a vital role in defining the heat transfer performance. Surface modifications by fabrication of micro/nano textured structures, followed by coating of low surface energy polymers (such as lubricants, Figure 1.3) have been shown to tailor the wetting or dewetting characteristics[13,14] of surfaces. Taking inspiration from nature,[15,16] numerous studies[17–20] have combined engineered surfaces with lubricants to achieve a desired wettability. Such surfaces are often referred to as liquid infused surface (LIS), and have been explored extensively owing to their excellent liquid repellency desired in numerous practical applications such as water harvesting[21], drag reduction[22,23], medical applications[24], corrosion resistance[25,26], condensation-based heat transfer applications[27], among others. Excellent water repellency/hydrophobicity, low drop roll-off angle (ROA < 5^{o}) and lower energy barrier for condensate nucleation[28] make LIS suitable for condensation heat transfer. Consequently, numerous fabrication techniques have been reported to mitigate lubricant depletion and to extend the operational lifespan of LIS such as, utilizing metal oxide nanowires and pores[21,25], trapped air[23], self-functionalizing lubricants[29], among others. However, after prolonged use of LIS, the lubricant layer on such surfaces depletes due to cloaking and wetting ridges (Figure 1.3), causing drop pinning and decline in wetting behavior. Depletion is even more pronounced in condensation-based applications as lubricant layer thickness is small and usually dictated by acceptable limit of oil-contaminant in condensates. Thus, efforts are required to sustain the condensation heat transfer performance on LIS, i.e., have a surface that would perform adequately even in depleted condition as well as in an open environment (i.e., presence of NCGs).

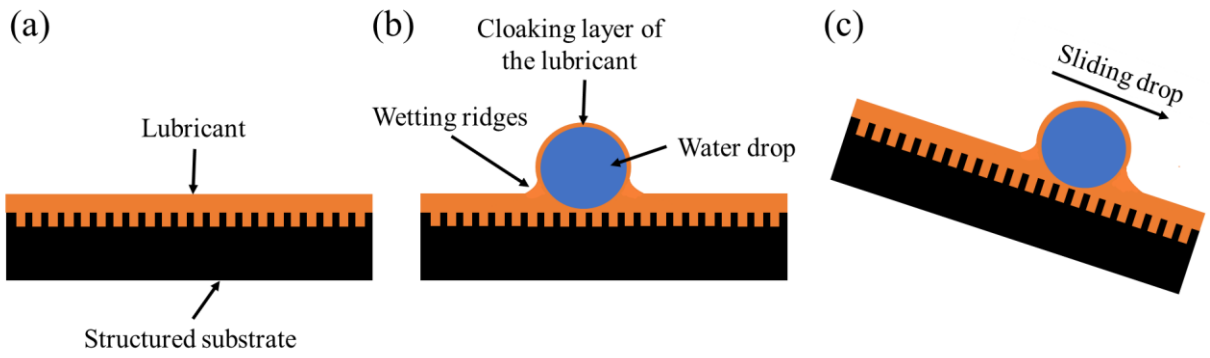

Figure 1.3. Liquid infused surfaces (LIS). (a) Typical infusion of lubricant in an engineering surface. (b) Wetting ridges surrounding the oil-water-air interface and cloaking of the drop with thin lubricant layer. (c) Water drop sliding down the LIS along with cloaked layer and ridges which results in loss of lubricant with each departing drop.

1.1.2 Superhydrophobicity on Micro/Nano Textured Surfaces

While LIS surfaces exhibit hydrophobicity and low roll-off angle, their application is primarily limited to condensation, drag reductions and corrosion resistance. Major drawbacks[30–32] of LIS surfaces are gradual depletion of lubricants, poor surface stability and inadequate performance under shear flow. Another category of multifunctional surfaces is superhydrophobic surfaces (SHS). In addition to having roll off angle lower than 5° for water droplets, as in the case of LIS, these surfaces have exceptional droplet mobility, with apparent contact angle exceeding 150°. Properties of SHS such as self-cleaning[33], corrosion resistance[34], drag reduction[35,36], oil-water separation[37,38], and anti-icing[39] make them potential solution for challenges related to aviation and wind turbines[40], power transmission[41] and, heat transfer[27]. Numerous studies mimicking the naturally evolved surface textures such as in lotus leaf[42], rose petals[43] and butterfly wings[44], with suitable organic and inorganic materials[45], have shown excellent water repellency; the unique feature of SHS is due to air

trapped in micro/nano cavities of the surface which minimizes the contact area between the solid and liquid resulting in Cassie-Baxter (CB) state[46] (Figure 1.4). Various materials such as graphene[47], polymers[48–50], silica[51,52], metal/metal oxides[53–55], and organic materials[56–58] have been studied extensively to fabricate robust, environmentally friendly SHS. Volmer et al.[59] reported Carbon nano-particles (CNPs) obtained from candle soot (CS) as a novel coating for preparation of superhydrophobic surfaces. However, CNPs network in CS are fragile and can't withstand shear stress induced by mobile water drops. Hence, to improve durability, chemical coatings such as polydimethylsiloxane (PDMS), wax or other polymers functioning as binding agents are required. In contrast to nature, artificial superhydrophobic surfaces go through rapid deterioration underwater, which is dependent on both time and depth of immersion[60]. Despite advances in fabrication techniques, unwanted transition from CB state to Wenzel state underwater or surface deterioration due to exposure to high humidity still poses a serious challenge to functionality of SHS (Figure 1.4). Consequently, thermally, mechanically, and chemically stable SHS with extreme durability to prolonged water and air exposure with simple, economical and regenerative coating is desired which can also exhibit multifunctionality.

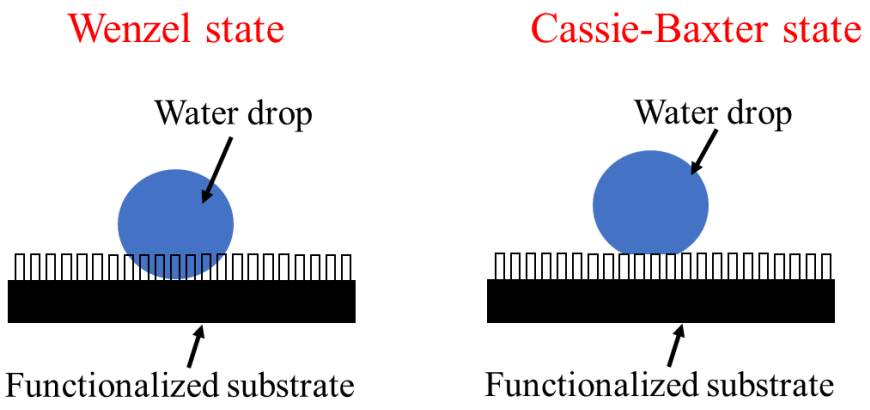

Figure 1.4. States of water drop on a structured surface

1.1.3 Porous Nanochannels for Vapor Generation

In addition to their hydrophobicity and superhydrophobicity, micro/nano textured surfaces have been extensively researched for their remarkable vapor generation ability by harnessing their hydrophilic nature. Vapor generation systems utilize thin-film evaporation[10] at the three phase contact line to improve the vapor generation rate. Ever advancing vapor generation techniques have found their application in areas such as wastewater treatment , desalination of seawater[61,62], low grade waste heat recovery[63,64], humidification[65] and steam sterilization[66] etc. Energy demand of such applications could be met with proper harvesting of renewable energy sources like solar heat flux. Being sustainable and abundant energy source with an average heat flux[67] of almost 1 kWm^{-2}, solar energy is being significantly sought after for reliable and efficient solar thermal technologies[68,69] among which solar vapor generation[70–78] is getting significant attention. Traditional solar vapor generation systems have relied on volumetric photo-thermal materials i.e. heating the liquid throughout the bulk[70,71] by dispersing thermally activated particles into water (Figure 1.5). This causes heat loss in form of sensible heat and convection from the bulk fluid or the container. To minimize such losses usually, interfacial vapor generation (IVG)[79,80] is preferred where heating is done near the liquid-air interface resulting in improved vapor generation efficiency[81] (Figure 1.5).

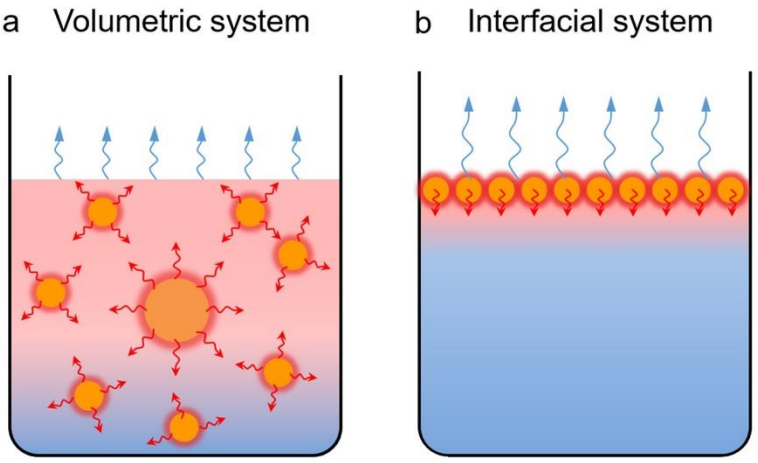

Figure 1.5. Schematic drawing of various photothermal evaporation systems; (a) the volumetric system and (b) the interfacial system. Reprinted with permission from zhu et. al.[82]. *Copyright (2019) Elsevier.*

Owing to significant solar absorbance[83,84] of solar radiation due to the high probability of transition in π band, carbon nanotubes(CNTs)[74], cellulose nanofibrils[75], graphene[85,86] and other carbon based materials[73,87,88] have gained immense attention with reported vapor generation rate rate[89] up to 1.51 $kgm^{-2}h^{-1}$ under 1 sun illumination 1 kWm^{-2}. Plasmonic heating based vapor generators (Figure 1.5) which commonly use nanoparticles[68], carbonaceous materials[90] and semiconductors[91] have been found to achieve solar conversion efficiency up to 97 % with vapor generation rate of 2.08 $kgm^{-2}h^{-1}$. The photothermal materials in electron-hole generation-recombination based devices are metal oxides/complexes[92,93] such titanium oxides, iron oxides, as well as mixed metal oxides which have shown the vapor generation rate[92] up to 2.04 $kgm^{-2}h^{-1}$. Besides maximum absorption of solar flux, an efficient photothermal material requires appropriately designed substrate capable of maintaining water transport rate equal to or above vapor generation rate. Various substrates such as cotton fibre[72], carbon foam[76], vertically aligned CNTs[83] and graphene sheets[86], artificial

sunflower bead[89], bi/trimetaloxide[92] have been investigated (Figure 1.6). There has been numerous study[94–99] on wicking and thin-film evaporation on microstructures, nanostructures and hierarchical surfaces which are mostly focused for thermal management devices such as vapor chambers and heat pipes rather than vapor generation. We can leverage the advantages associated with thin-film evaporation in a vapor generation system (Figure 1.5) to achieve high vapor generation rate using a porous nanochannel sample.

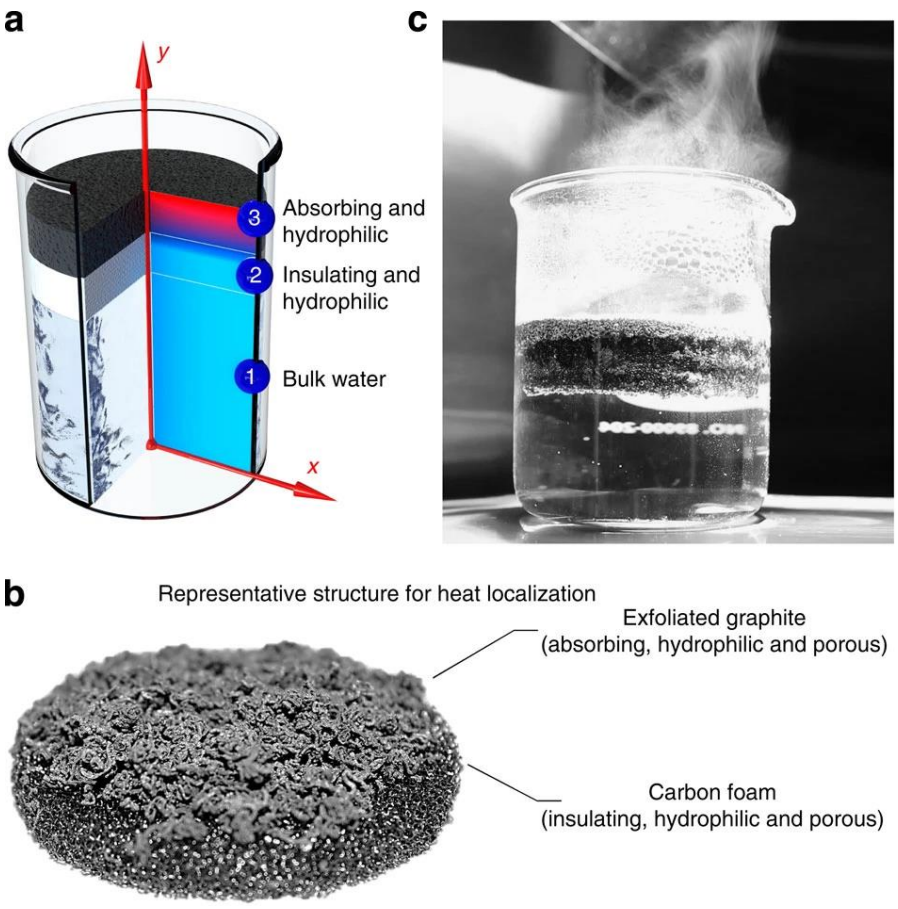

Figure 1.6. Localized heating. (a) A representative structure for localization of heat; the cross section of structure and temperature distribution. (b) The device consists of a carbon foam (10-mm thick) supporting an exfoliated graphite layer (~5-mm thick). Both layers are hydrophilic to promote the capillary rise of water to the surface. (c) A picture of enhanced steam generation by

the device structure under the solar illumination of 10 kWm^{-2}. Reprinted with permission from Ghasemi et. al.[76]. *Copyright (2014) Springer Nature.*

1.1.4 Nanochannels for Thermal Management

Another strategy to utilize the thin-film evaporation (Figure 1.7) is thermal management of integrated circuits (ICs). Ongoing miniaturization[100,101] of ICs requires evolution of effective thermal management strategies to dissipate localized heat generation and attain 1 kWcm^{-2} of heat flux removal in near future. Additionally, space constraints in such devices require small form factor cooling solutions and have led to several approaches including microchannel heat sinks[102–104], embedded cooling,[105] nano/micro structured heat pipes[106,107], and graphene heat spreaders[108] among others. Regardless of device type or design, thin film evaporation-based[10] cooling approach using heat pipes is considered one of the prominent techniques prompting several studies[109–111] to address the on-chip hot spot thermal management. Such devices rely on the passive capillary-driven flow of working fluids, such as water, refrigerants, and alcohol, among others, enabled by porous wicks. Numerous wick materials and fabrication techniques namely metallic pillars[96,112], sintering[113], and 3D printed metal[114] have been investigated to improve the thermal performance of evaporators in heat pipes. Recent studies[109–111] reporting interfacial evaporative heat flux ~ 0.5-11 kWm^{-2}K^{-1} provide insight into the potential of thin-film evaporation-based device for effective thermal management.

Besides the dependability of CA measurement in determining high interfacial heat flux in reported studies, wick distance is typically a few microns[109–111,115–117], which are prone to dry out. Further, the choice of working fluid is dictated by its physical properties, the requirement for heat dissipation, suitability for the application site, and potential risks. Among

these fluids, FC72 with its dielectric properties has been found to be a suitable working fluid in oscillating heat pipes[118,119] and has demonstrated superior heat transfer performance over water thin film using gas assisted evaporation[120]. Therefore, a thin film evaporation-based thermal management device is required which can maintain larger wicking distance at steady-state while demonstrating high evaporative heat estimated by a novel approach that does not depend on contact angle measurements in confined space and associated uncertainties.

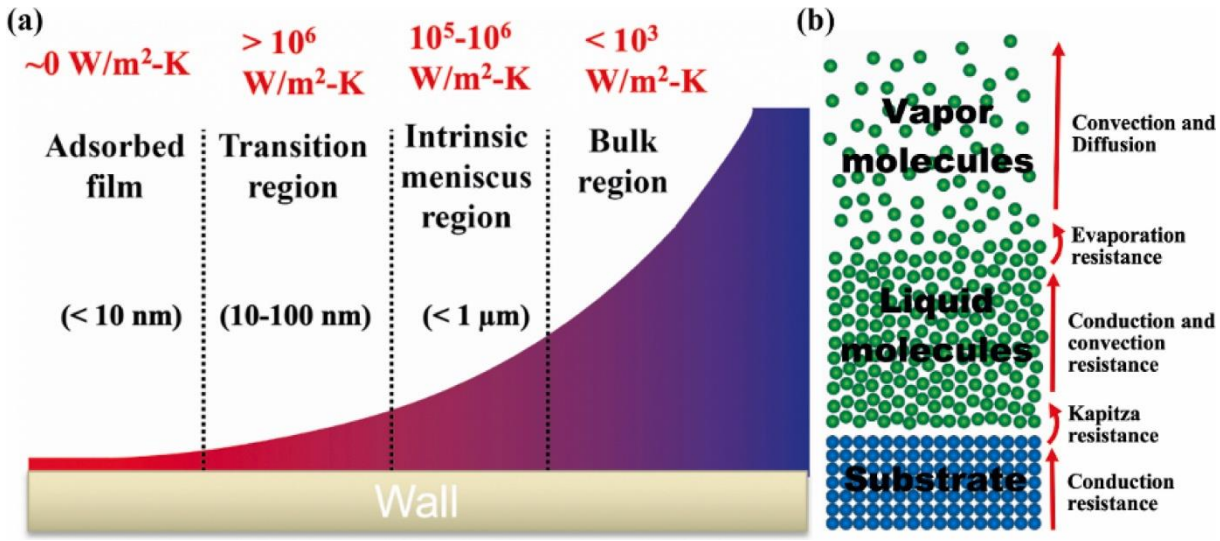

Figure 1.7. Thin-film evaporation. (a) The variation of local film thickness and heat transfer coefficient in different regions of an evaporating thin-film (e.g., water). The heat transfer coefficient at the transition region is over 1000 times greater than that at the bulk region. (b) Schematic illustration of different thermal resistances involved in the thin-film evaporation process. Reprinted with permission from Nahar et.al.[121] *Copyright (2021) Elsevier.*

Chapter 2: Condensation on Porous Nanochannels Based Liquid Infused Surfaces

2.1 Introduction

Durability of lubricant infused surface (LIS) is critical for heat transfer, especially in condensation-based applications. A typical LIS has an underlying micro/nano textured surface coated with low surface energy polymer/chemical which then gets infused with non-toxic, low surface tension and low vapor pressure lubricant.[26–31] Several techniques such as gravimetric draining[128], spin coating[129] or dip coating[130] are used to obtain a desired thickness of lubricant film on the surface. However, functionality of all these surfaces relies on the retention of oil in the surface topography either through active lubricant supply[131] or by special design arrangement which can continuously feed the textured surface[132]. Apart from wetting ridges and condensate cloaking-induced depletion[133], LIS undergo external shear[32] driven drainage during relative motion between the LIS and any fluid.

Condensing vapor on a pristine LIS exhibit extremely mobile and distinct liquid droplets (i.e. dropwise condensation or DWC) which get shed continuously resulting in significantly improved heat transfer performance[134] as compared to condensation on plain surface over which a blanketing liquid film develops (i.e. filmwise condensation or FWC). Although LIS promotes dropwise condensation, each departing droplet condensate acts as a lubricant-depleting agent due to formation of wetting ridge and cloaking layer around the condensate. Consequently, maintaining lasting DWC even on LIS is challenging without any external aid, as the droplet resting on lubricant film gets cloaked and surrounded by lubricant wetting ridges[135] wherein oil rises up along the droplet outer contour causing oil depletion with each shedding condensate droplet[31]. Gradual depletion of lubricant appears to be an inherent issue of LIS resulting in

drop pinning on underlying rough topography. Additionally, heat transfer performance deteriorates[136,137] significantly when condensation is performed in the presence of non-condensable gases (NCGs) or in an open environment, as gases act as a thermal barrier and occupy potential nucleation sites on the lubricant-vapor interface resulting in deterioration of heat transfer performance which explains the relatively few studies[124,137,138] reporting condensation in the presence of NCGs. Further, performing condensation without NCGs also requires additional equipment and design considerations[27,28,31,124,126,139] such as specialized chambers and vacuuming systems to ensure the absence of NCGs at lubricant-vapor interface. Thus, for condensation in the presence of NCGs, both high nucleation rate and rapid droplet departure are desired on the condensing surface.

Study reported in this chapter deals with fabrication of both fresh LIS and lubricant-depleted LIS using silicon porous nanochannel wicks as an underlying substrate. Strong capillarity in the nanochannels helps retain silicone oil (polydimethylsiloxane) on the surface even after it is severely depleted under tap water jet. The effect of oil viscosity was investigated for drop mobility and condensation heat transfer. Fresh LIS prepared using 5 cSt silicone oil exhibited low roll-off angle (~1^{o}) and excellent water drop (5 µl) sliding velocity ~ 66 mm^{-1}; however, such low viscosity oil undergoes rapid depletion. Condensation performed on depleted nanochannel LIS with higher viscosity oil (50 cSt) resulted in heat transfer coefficient (HTC) ~ 2.33 $kWm^{-2}K^{-1}$, which is ~ 162% improvement over flat Si-LIS (50 cSt). Rapid drop shedding on depleted nanochannel LIS with 50 cSt oil resulted in steady condensation as observed from little change in fraction of drops with diameter < 500 µm from ~ 98 % to only ~ 93 % after 4 hours of condensation. Improvement in HTC was also confirmed by performing a total of 3 days of condensation on fresh LIS over an 18-day period, which included a 15-day gap between first day

and last two days of experiments where the sample was kept exposed to ambient conditions. With initial oil depletion, HTC increased by 16% improvement over the first day, and achieved a steady HTC of ~1.46 $kWm^{-2}K^{-1}$ in the last two days. The LIS surface maintained dropwise condensation, never transitioned to film-wise condensation, and retained its hydrophobicity throughout the condensation period. The findings reported in this chapter could be beneficial in designing condensation-based systems with improved heat transfer performance.

2.2 Methodology

LIS sample preparation starts with fabrication of porous nanochannel sample[140,141] on a 500 μm thick silicon wafer involves dedicated photolithography procedures using sacrificial chromium and copper layer. The detailed procedure and methodology are provided in Appendix A1. Nanochannels fabricated orthogonally on silicon wafer have both width and pitch of ~5.75 μm, and height of ~728 nm creating numerous intersections and trenches. At each intersection, a pore of diameter ~2 μm was fabricated which allows oil to wick into the nanochannels. Figure 2.1 shows the nanochannel sample used in current study with a hydrophilic (WCA ~ 10ºC) porous nanochannel region. The porous region is 14 mm by 14 mm and the surrounding surface on the outside is flat silicon wafer with porosity of ~0.75. The three-dimensional schematic (Figure 2.1b) shows interconnected nanochannels where pores have been fabricated at each intersection, allowing lubricant to wick into the nanochannels. Details on surface morphology can be found in micrograph and atomic force microscope of the sample as presented in Figures 2.1c and 2.1d, respectively. Figures 2.1e through 2.1g depict the preparation of nc-LIS, starting from flooding the plasma-treated nanochannel sample with adequate silicone oil (Figure 2.1f), baking in a convective oven overnight at 150℃. This process of baking was found to be beneficial in keeping the surface hydrophobic and ensuring proper infusion of oil in the channels

even for high viscosity oil. This was followed by 4 hours of oil draining under gravity (Figure 2.1g) resulting in fresh nanochannel LIS (nc-LIS). An image captured during spreading of silicone oil drop (η_o= 5 cSt) on the plasma treated nanochannel sample is shown in Figure 2.1i. Such four different nc-LIS samples were obtained using different silicone oils (viscosity η_o= 5 cSt, 50 cSt, 500 cSt and 1000 cSt; for reference DI water has viscosity 2.1 cSt). To attain depleted nanochannel LIS sample (dep-nc-LIS), nc-LIS was kept horizontally under tap water jet to further deplete oil under shear imparted by running tap water (jet velocity ~ 0.4 ms^{-1}) for 20 minutes from a nozzle of diameter 4.6 mm, followed by 30 minutes in convection oven at 150°C. Keeping sample in oven is important as presence of water would hamper the weight measurement of depleted LIS sample to obtain the amount of oil present in the sample. Another reason to keep sample in oven was to have uniform contact angle at various locations on the surface by inducing uniform oil infusion and baking. All contact angle measurements were repeated six times in ambient condition (23^{o}C, 40 % relative humidity) with water drop volume of 3±1 µl on VCA optima goniometer. High-speed camera captured water droplet motion which was later used to obtain sliding velocity by performing image analysis through a custom MATLAB script.

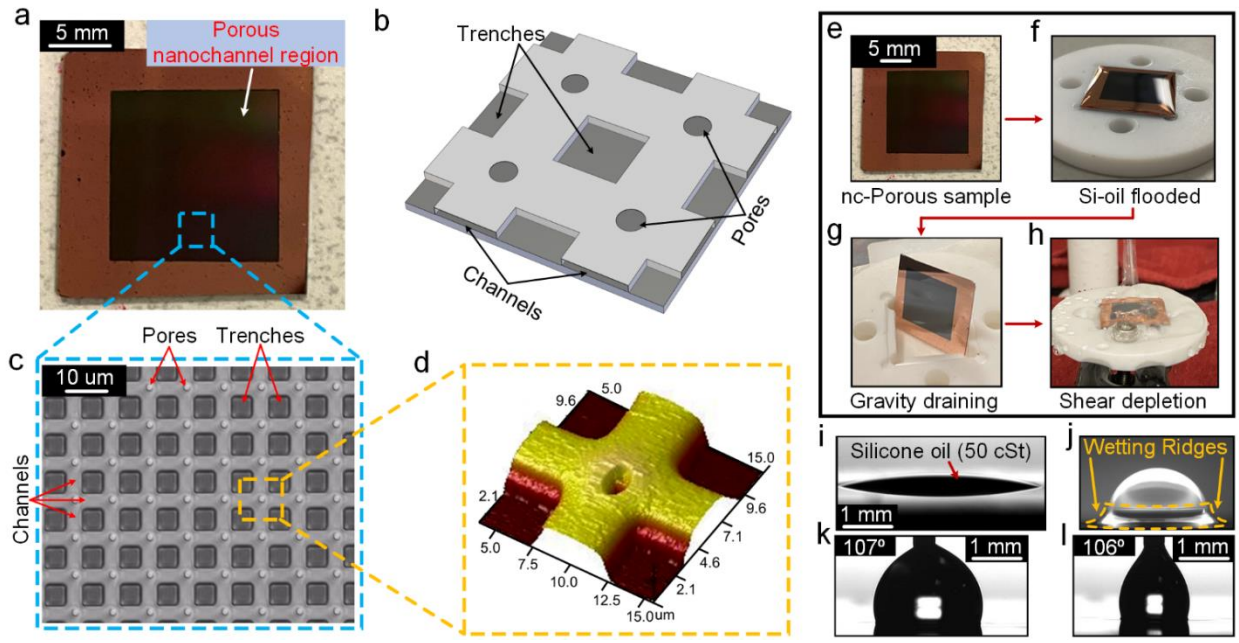

Figure 2.1. Sample details, morphology characterization and LIS Preparation: (a) silicon base showing nanochannel porous region, (b) three-dimensional schematic of a sample unit cell in porous region comprising intersecting channels (height ~ 728 nm, width ~ 5.75 µm), four pores (diameter ~ 2 µm) at each channel intersection, and trenches (c) micrograph of porous nanochannel sample, (d) Atomic force microscope (AFM) image of a pore fabricated at channels intersection, (e-f) nanochannel depleted lubricant infused surface preparation stages: pristine sample followed by flooding with silicone oil, gravimetric depletion and shear depletion under tap water at 0.4 ms^{-1} (i) snapshot of silicone oil (50 cSt) spreading on porous nanochannel wicks sample (j) wetting ridges around fluorescence dissolved-water drop on (nanochannel) nc-LIS 50 cSt (k-l) advancing and receding contact angle on nc-LIS 5 cSt, respectively.

Further, freshly prepared nc-LIS surface was found to exhibit wetting ridges as seen around a florescence water drop (Figure 2.1j) similar to numerous reported studies[18,31,45,126,135].

Despite being not clearly visible from Figure 2.1j, theoretical prediction criteria given in Equation 2.1 suggest presence of cloaking around drop shown in figure 2.1j.

$$S = \gamma_{wa} - \gamma_{oa} - \gamma_{wo} \qquad \textit{Equation 2.1}$$

where, S is the spreading coefficient (S > 0 signifies cloaking), γ_{wa}= 72.7 mNm^{-1} is the interfacial tension between water and air, γ_{ow} = 6 mNm^{-1} is the interfacial tension between oil and air[135] and γ_{oa}= 21 mNm^{-1} is the interfacial tension between water and oil. Positive value for spreading coefficient is obtained for all four-silicone oil used in present study. Water contact angle hysteresis (CAH) measured on freshly prepared nc-LIS with 5 cSt oil shows very low difference (~ 0.6^o) between advancing and receding contact angle (Figure 2.1k,l), which is a desired characteristic of any LIS. Tap water jet (Figure 2.1h) on the nc-LIS sample was used to obtain dep-nc-LIS sample, as explained in section 2.2. Although shear imparted by flowing water did result in severe depletion of oil, all the surfaces remained hydrophobic with WCA >100^o In addition to reported studies[142–144] on plasma treated surface activating enhanced hydrophilization and improving adhesive strength of siloxane, strong capillarity within the nanochannels and micropores appears to be responsible for retaining oil and thus sustaining surface hydrophobicity even after severe water shear depletion. Condensation was performed on LIS in presence of non-condensable gases. Schematic of condensation experiment setup is shown in Figure 2.2 while actual experimental setup can be referred from Appendix A1. The condensation chamber was open to atmosphere with average relative humidity inside the chamber being ~87 %. Back side of LIS was attached to an aluminum cold plate through which a thermal fluid (ethylene glycol-deionised water mixture) was allowed to flow. The temperature of thermal fluid was controlled by a recirculating chiller and flow rate was maintained by a custom-built flow rate control circuit. A video camera was used to record condensate drop size

distribution at different time intervals. These recorded frames were then analyzed for the droplet size distribution through a custom written MATLAB script. Drops are converted into binary form by choosing a threshold value of inbuilt MATLAB function parameters followed by creating circles incapsulating individual droplets. Pixels corresponding to each drop in the images give the respective diameter.

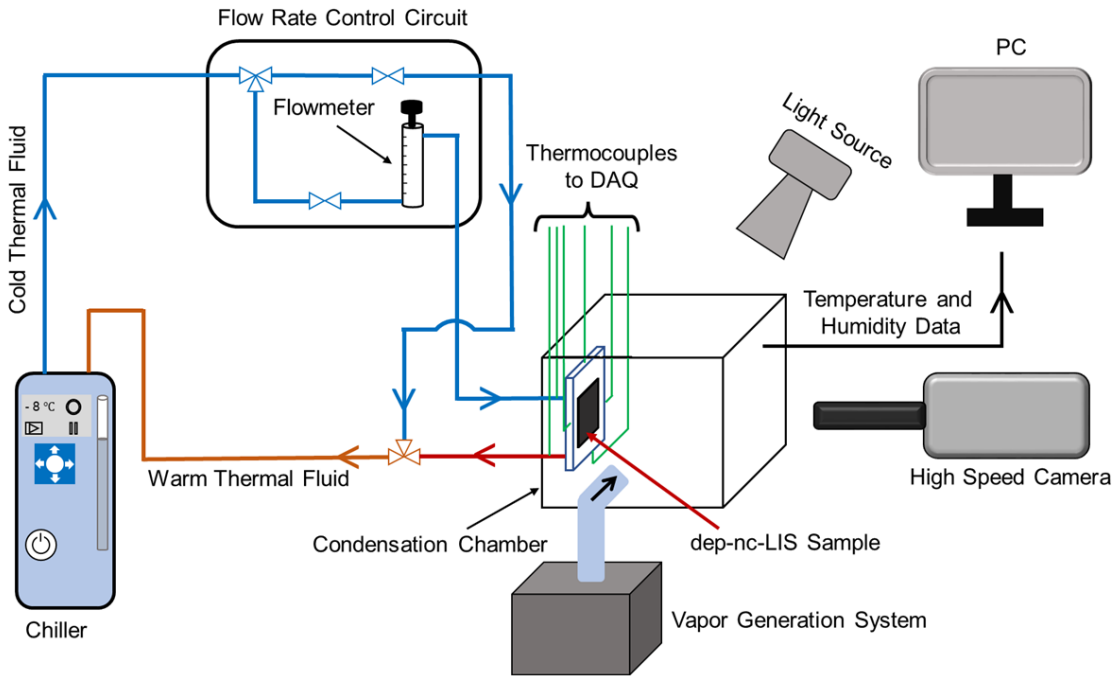

Figure 2.2. Schematic of custom-built condensation experiment setup.

2.3 Results

2.3.1 Effect of Viscosity on Drop Roll-off Angle and Oil Thickness

Roll-of-angle (ROA) measured with 5 µl water drop for nc-LIS surfaces prepared from 5 cSt, 50 cSt, 500 cSt and 1000 cSt were ~1º, ~1º, ~4º, ~6º respectively. High viscosity accounts for increased friction at drop-oil interface during sliding, resulting in the observed increment in ROA with oil viscosity[145]. Oil thickness (t_o) on the surface of fresh nc-LIS was obtained using mass change technique[21,146] using following equation:

$$t_o = \frac{\Delta w - w_{o,nc}}{\rho_o A_s}$$ *Equation 2.2*

where, Δw is the difference between weight of dry sample (w_{dry}) measured before oil infusion and weight after gravimetric draining (w_g), and ($w_{o,nc}$)is the theoretical weight of oil in present within the channels and pores (~ 0.1 mg), ρ_o is oil density, and A_s is the projected area of the porous region of the sample. $w_{o,nc}$ is obtained from the volume of the nanochannels and the density of silicone oil. Oil thickness was obtained as 0.98 µm, 4.01 µm, 7.47 µm, 10.04 µm, respectively with increasing viscosity of oils.

2.3.2 Effect of Viscosity on Drop Mobility

Freshly prepared nc-LIS for all four-silicone oil viscosities were subjected to water drop mobility test by measuring velocity of various drop sizes at multiple angles of inclination. Figure 2.3a shows water drop (with dissolved fluorescence salt) sliding down the nc-LIS prepared with 5 cSt silicone oil kept at 5º inclination. An image processing algorithm which tracks the drop contour during motion is implemented to determine the average drop velocity with very high accuracy (Appendix A1). Variation of water drop sliding velocity (V_s) on nc-LIS with surface angle of inclination for different drop volume (5 µl – 50 µl) and oil viscosity is shown in Figures 2.3b through 2.3e. Similar to previously reported studies,[124,145,147] V_s is observed to be inversely proportional to oil viscosity and increases with both angle of inclination and drop volume. Thus, as far as drop mobility is concerned in freshly prepared state, nc-LIS behaves like reported LIS surfaces. V_s obtained on nc-LIS with 5 cSt oil was an order of magnitude higher than those observed with 500 cSt or 1000 cSt oils. Although high V_s associated with low viscous lubricant is a desirable characteristic, it undergoes rapid oil depletion as reported in the next section.

Therefore, choosing suitable viscosity lubricant becomes critical in maintaining durability of LIS properties.

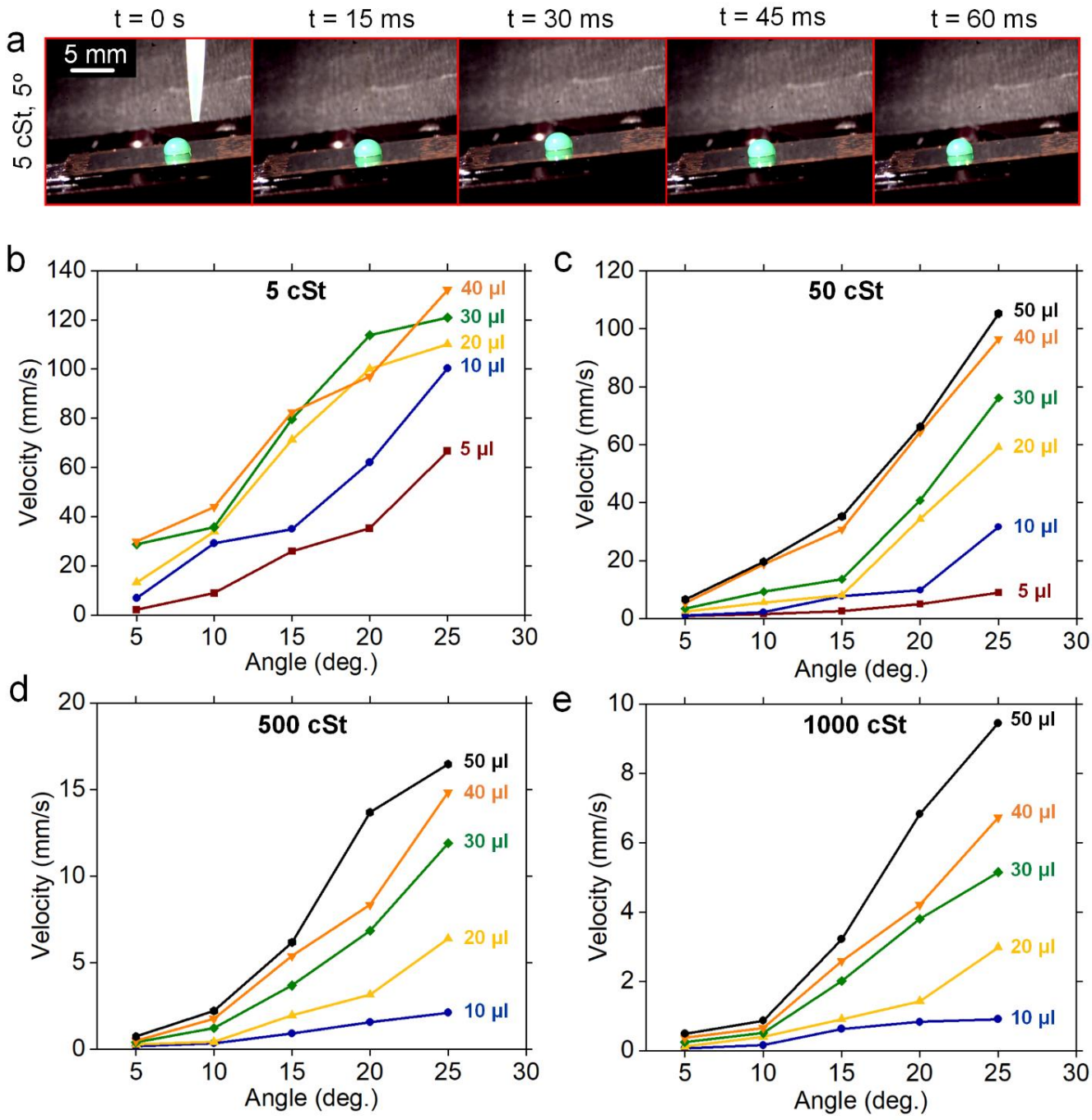

Figure 2.3. Sliding velocity (V_s) for water drop of various volume on freshly-prepared nanochannel lubricant infused surface (nc-LIS): (a) a series temporal images depicting 10 µl drop

sliding on a nc-LIS with 50 cSt at 5º angle of inclination during velocity measurement test, (b-e) variation of water (volume: 5 µl – 50 µl) droplet velocity for different angle of inclination and all four prepared nc-LIS with different silicone oil viscosity (5 cSt, 50 cSt, 500 cSt, 1000 cSt).

2.3.3 Effect of Viscosity on Lubricant Depletion

Presence of the silicone oil in dep-nc-LIS, following water shear depletion (Figure 2.1h), was confirmed by quantifying the weight change (Δw_d, Figure 2.3a) given by following equation:

$$\Delta w_d = w_{dep} - w_{dry} \qquad \text{Equation 2.3}$$

where, w_{dep} is weight of dep-nc-LIS sample and w_{dry} is weight of dry sample measured before oil infusion. The silicone oil retention in nanochannels can be attributed to: (1) capillarity, and (2) combined effect of improved adhesion (of silicone oil due to plasma cleaning), van der Waals or any other intermolecular interaction[148] as oil is confined at the nanoscale. FT-IR (Appendix A1) spectrum of dep-nc-LIS surfaces confirms the presence of C-H, Si-O-Si present in silicone oil. Oil thickness in dep-nc-LIS following the water jet shear induced depletion was found to be ~ 245 nm, ~ 601 nm, ~1.36 µm, ~2.11 µm for 5 cSt, 50 cSt, 500 cSt and 1000 cSt, respectively as evaluated using Equation 2.2. Figure 2.3b shows changes in surface appearance under microscope with time of shear depletion under tap water jet and their respective WCA. Detailed temporal variation of apparent WCA due to shear depletion for 5 cSt, 50 cSt, 500 cSt and 1000 cSt oil samples is presented in Figure 2.3c-f. While apparent WCA increased at first, depletion of oil is found to be relatively higher[32,149] in low viscous lubricants based on the observed decline in apparent WCA after ~ 240 s for 5 cSt due to droplet pinning, and ~540 s for 50 cSt due to higher contact angle hysteresis (Figure 2.3c-d). With gradual depletion of oil, contact line concealed within the lubricating meniscus progressively becomes observable and, LIS moves from excess-oil to oil-starved state, thus shifting observable water drop contact line close to true

contact line on the surface (unaffected by oil ridges), and hence measured WCA is observed to increase[150] for all four cases up to certain duration depending on the oil viscosity. Conversely, 500 cSt (Figure 2.3e) and 1000 cSt (Figure 2.3f) oil samples show increment in WCA till 1200 s as the depletion process is ongoing, evident from the more oil retention on such surfaces (Figure 2.3a). While both surfaces with 500 cSt and 1000 cSt oil possess desired wettability, drop mobility on these surfaces is found to be unfavorable (Figures 2.2d,e). Thus, dep-nc-LIS with 50 cSt oil presents a good trade-off between both features, i.e., high drop mobility (Figure 2.2c) and persistent hydrophobicity during depletion (Figure 2.3d), making it a suitable choice for evaluating its condensation heat transfer performance. In present study, based on V_s and oil depletion (inferred from oil mass change, Figure 2.3a), we found nc-LIS prepared with 50 cSt oil performed superior to nc-LIS prepared with other viscosity oils.

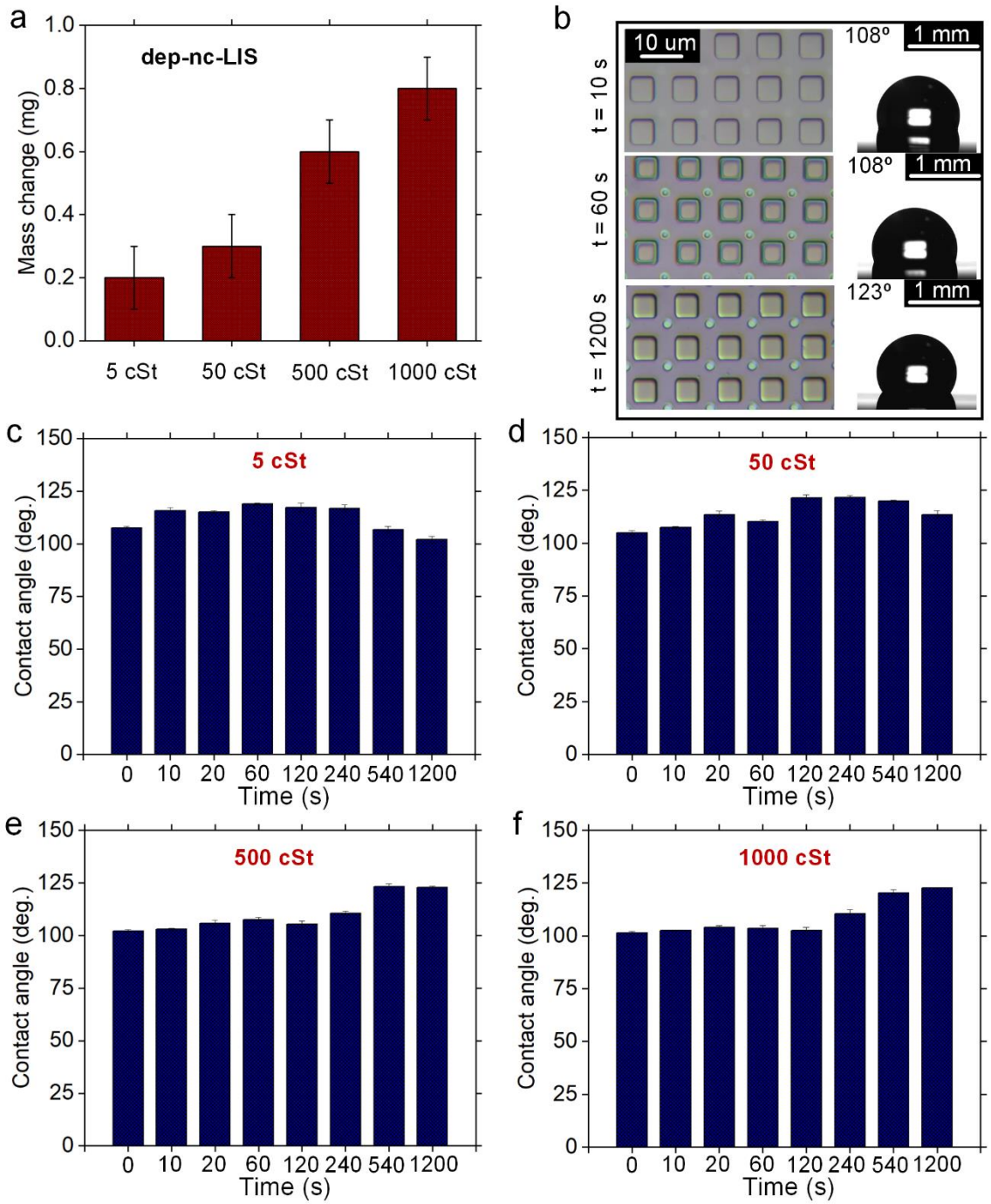

Figure 2.4. Effect of water shear depletion on the wettability of nanochannel depleted lubricant infused surface (dep-nc-LIS): (a) difference in the weight of dry sample (before oil infusion) and dep-nc-LIS surface for all four prepared nc-LIS with different silicone oil viscosity (5 cSt, 50 cSt, 500 cSt, 1000 cSt), (b) effect of tap water shear depletion as noticeable from micrograph and

water contact angle measurements at different time interval, (c-f) variation in water contact angle observed during tap water shear depletion of fresh nc-LIS for all four prepared samples having different silicone oil viscosity (5 cSt, 50 cSt, 500 cSt, 1000 cSt).

2.3.4 Condensation on Porous Nanochannel Lubricant Infused Surface

In order to test the heat transfer performance of our LIS, all condensation experiments were carried out in ambient air, i.e., in the presence of non-condensable gases (NCGs). Schematic of the experimental setup is shown in Figure 2.2. To conduct the condensation experiments, we chose a nanochannel sample with larger sample size (28.1 mm by 35.8 mm) but with same underlying geometry dimension of nanochannels and micropores. After sample preparation and oil depletion, LIS was attached to a custom-made aluminum plate through which cold thermal fluid (ethylene glycol-water) was supplied from a recirculating chiller. Constant flow rate of cold thermal fluid was maintained using a flow meter valve in custom-designed flow rate control circuit. Aluminum cold plate was sealed on all exposed areas using RTV silicon sealant except for the LIS sample. The cold plate along with the sample were subsequently positioned on one of the faces of open condensation chamber facing the high-speed camera (Figure 2.2). Four thermocouples were inserted (3 mm under the condensing LIS surface from all four sides) in the cold plate to record the surface temperature. Moreover, two thermocouples were inserted in the inlet and outlet tubes of cold plate to monitor the temperature change (ΔT_w) of water-glycol mixture during condensation that was further used in condensation heat transfer (Q_w) calculation. Humidity and temperature in the condensation chamber was maintained by a boiling-based external vapor generation system.

Heat transfer coefficient (HTC) calculation involves the following two equations:

$$Q_w = \rho_m V_m C_p (\Delta T_w)$$ Equation 2.4

$$Q_w = h_c A_s \Delta T_{sub}$$ Equation 2.5

where, Q_w is the condensation heat transfer (W) and is assumed to be same as heat taken away by cold thermal fluid, ρ_m= density of water-glycol mixture (50:50), 1085 kgm^{-3} at 10ºC, V_m is volume flow rate of water-glycol (50:50) during experiment (47.7 ccm), C_p is specific heat of water-glycol (50%), 3.44 $kJkg^{-1}K^{-1}$at 10ºC, h_c is condensation heat transfer coefficient ($Wm^{-2}K^{-1}$), A_s is LIS projected surface area, $1005.98*10^{-6}$ m^2, and ΔT_{sub} is the temperature difference between dep-nc-LIS average surface temperature and ambient condensation chamber temperature (T_{amb}). Calculations for h_c, Q_w and related error and uncertainty analysis is presented in Appendix A1. Two different sets of condensation experiments were performed. In the first set of experiments that lasted for 4 hours and 15 minutes each, flat Si-LIS and depleted nc-LIS (50 cSt, 500 cSt) samples were used. Results obtained from above experiments were evaluated against second type of experiment which involved 3 days of condensation performed over an 18-day period on fresh LIS on porous nanochannel with 50 cSt silicon oil, referred to as nc-LIS-50. Similarly, samples of dep-nc-LIS with 50 cst oil, and 500 cSt oil will be referred to dep-nc-LIS-50, and dep-nc-LIS-500, respectively in the remainder of this work.

For the first set of experiments conducted for 4 hours and 15 minutes each, variation of HTC for flat Si-LIS with 50 cSt oil, dep-nc-LIS-50, and dep-nc-LIS-500 is shown in Figure 2.5a. Variation of ambient chamber temperature (T_{amb}), average sample temperature ($T_{sample,avg}$), thermal fluid temperature at cold plate outlet ($T_{fluid,out}$) and thermal fluid temperature at cold plate inlet ($T_{fluid,in}$) during condensation is shown in Figure 2.6. Although there are localized variation in HTC throughout the experiment (due to varying degree of vapor content coming into

condensing chamber which dictates the ΔT_{sub}, overall HTC obtained for dep-nc-LIS-50 was: 2.33 ± 0.42 $Wm^{-2}K^{-1}$ which is ~162 % and ~40 % improvement over flat Si-LIS with 50 cSt oil (h_c=0.89 ± 0.16 $Wm^{-2}K^{-1}$) and dep-nc-LIS-500 (h_c=1.66 ± 0.25 $Wm^{-2}K^{-1}$), respectively.

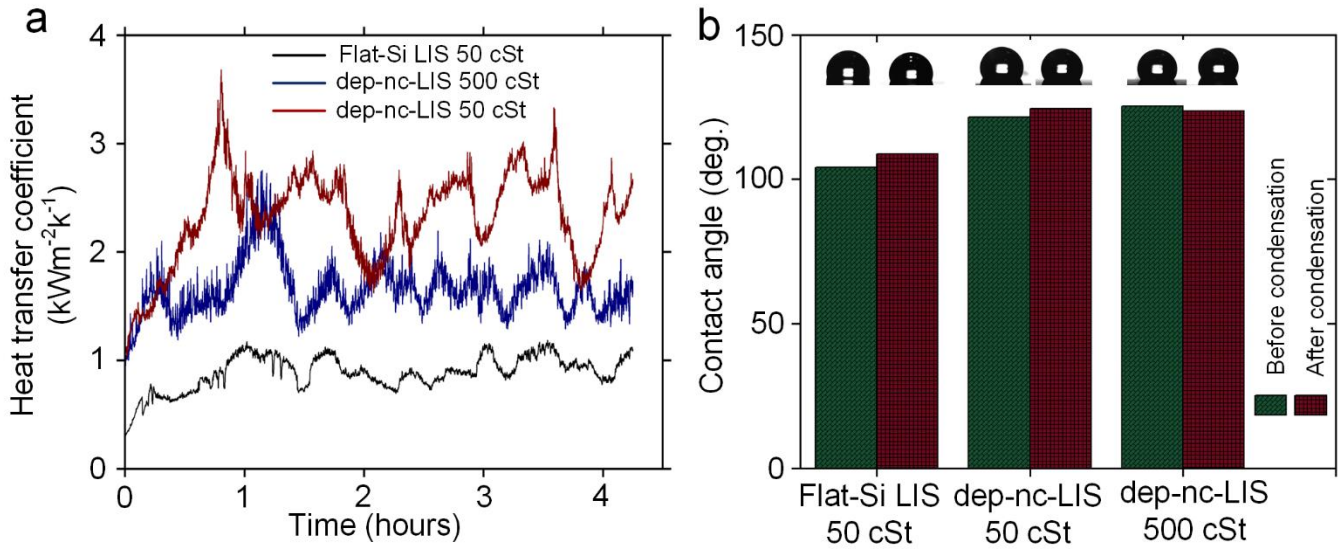

Figure 2.5. Condensation of water vapor on three different depleted liquid infused surface namely, flat Si-LIS with 50 cSt oil (LIS on flat silicon surface), and two nanochannel depleted lubricant infused surfaces (dep-nc-LIS with 500 cSt oil, and dep-nc-LIS with 50 cSt oil), showing: (a) variation of heat transfer coefficient (HTC) for depleted samples, and (b) water contact angle before condensation and after 4 hours 15 minutes of condensation on depleted sample.

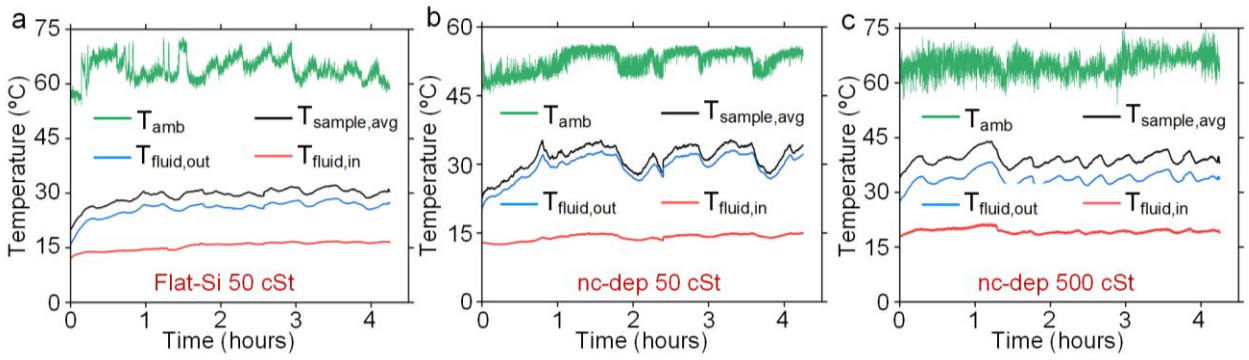

Figure 2.6. Variation of ambient chamber temperature (T_{amb}), average sample temperature ($T_{sample,avg}$), thermal fluid at temperature cold plate outlet ($T_{fluid,out}$) and thermal fluid at cold plate temperature inlet ($T_{fluid,in}$) during condensation for: (a) LIS on flat silicon surface with 50 cSt oil, (b) depleted LIS on porous nanochannel with 50 cSt oil, and (c) depleted LIS on porous nanochannel with 500 cSt oil.

In case of flat Si-LIS with 50 cSt oil, depletion process preceding condensation resulted in removal of surface oil to the fullest extent as apparent from the temporal drop size distribution during condensation (Figure 2.7); hence flat Si-LIS with 50 cSt oil exhibits lower HTC over time. Moving average of HTC for dep-nc-LIS-50 and dep-nc-LIS-500 reveals modest depreciation as evident from the small increment in condensate drop size on the surface and delayed shedding. While condensing surface being in depleted state does not hold sufficient oil to cloak droplets, there exists the possibility of oil depletion (during droplet shedding) from shear due to oil menisci formed at ridges. This shear depletion of oil is opposed by the existing capillary pressure inside the nanochannels and is inversely proportional[32] to oil viscosity, thus causing retention of oil on the sample. Variation in surface wettability because of condensation is reported in form of WCA measured before and after condensation experiments for all three cases

(Figure 2.5b). Maximum variation was found to be ~ 5º for flat Si-LIS surface and was less than ~3º for dep-nc-LIS surfaces.

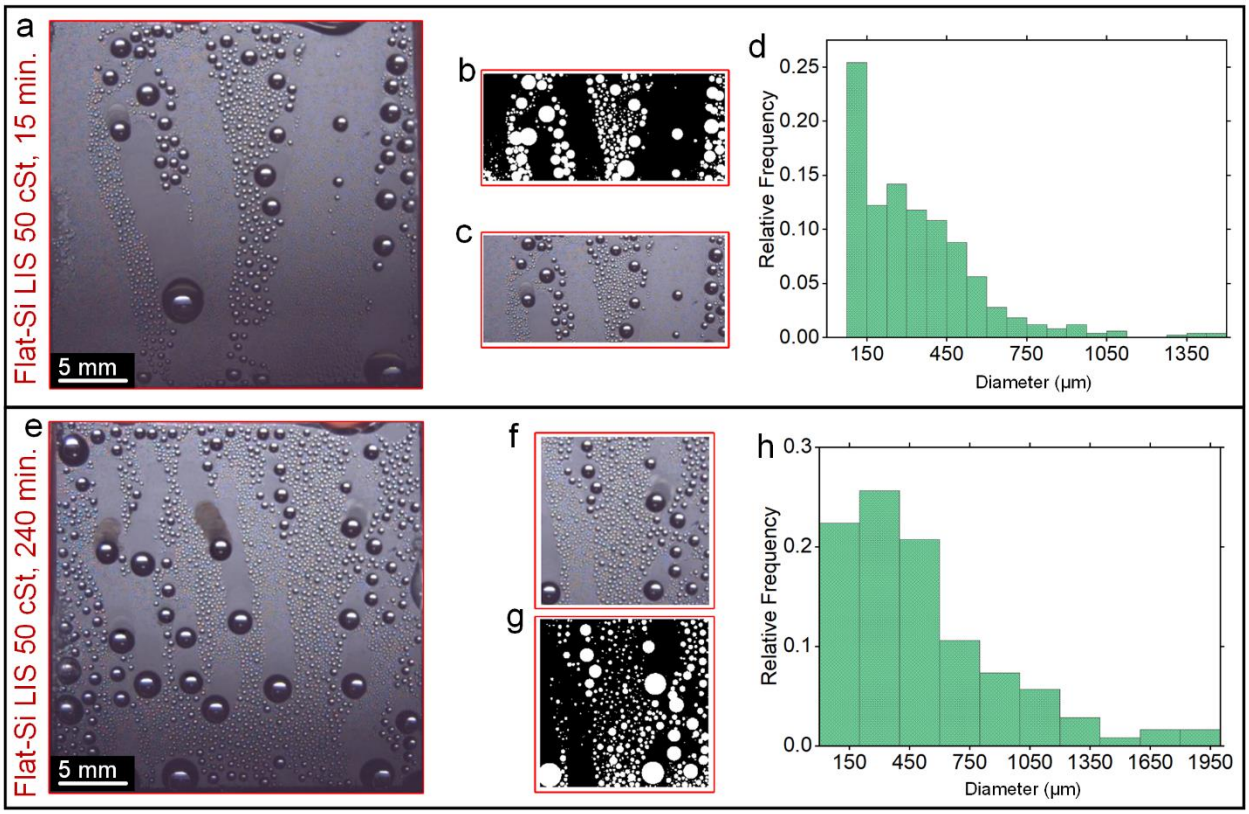

Figure 2.7. Drop size distribution for a selected region on flat silicon (flat Si) liquid infused surface (LIS) sample during experiment for (a-d) flat-Si 50 cSt after 15 minutes of condensation, (e-h) flat-Si 50 cSt after 240 minutes of condensation.

Table 2.1. Variation in contact angle hysteresis after condensation

Depleted LIS surface type	Before condensation			After condensation		
	Advancing (θ_a)	Receding (θ_r)	Hysteresis ($\theta_{h,b}$)	Advancing (θ_a)	Receding (θ_r)	Hysteresis ($\theta_{h,a}$)
Flat Si-LIS-50 cSt	Pinned	Pinned	N/A	Pinned	Pinned	N/A
dep-nc-LIS-50	117º	88º	29º	126º	72º	54º
dep-nc-LIS-500	124º	93º	31º	127º	71º	56º

A distinct change in contact angle hysteresis (CAH) of all three samples used for condensation can be seen from Table 2.1. Considering severe depletion of oil before condensation, pinned droplets on flat Si-LIS with 50 cSt oil is obvious. Even though dep-nc-LIS-50 and dep-nc-LIS-500 did not manifest droplet pinning, significant rise in CAH after condensation indicates surface degradation. The extent of surface deterioration during condensation experiment for flat Si-LIS with 50 cSt oil (Figure 2.7), dep-nc-LIS-50 (Figure 2.8(a-h)) and dep-nc-LIS-500 (Figure 2.8(i-p)) has been investigated by analyzing the condensate drop size distribution on the condensing surfaces (Figure 2.6d,h,l,p). Histograms (bin size = 75 μm) show the relative frequency of occurrence of a particular size group of droplets. Drop growth on the upper portion of the sample is faster as cold fluid from chiller enters at the top of cold plate, prompting coalescence and

earlier shedding of drops there than those at the bottom of surface. The departing drop leaves behind a regenerated area for re-nucleation of new drops. Consequently, frequent drop departure results in higher fraction of condensation surface observing nucleation and hence an improvement in HTC. It was found that percentage of drops having diameter < 250 μm at the beginning of condensation was ~ 41%, ~ 65% and ~ 84% for flat Si-LIS, dep-nc-LIS-50, and dep-nc-LIS-500, respectively, which dropped towards the end of condensation to ~ 28%, ~ 73% and ~ 52%, respectively for the same surfaces. Throughout the condensation, fractional coverage of large drops is most pronounced in flat Si-LIS surface and is undesired because water has high conduction resistance during high heat transfer between hot vapor and condensing surface. This is consistent with the obtained HTC for all three surfaces. Comparison of drop size < 500 μm elucidates the contrasting difference in heat transfer performance of dep-nc-LIS surfaces compared to flat Si-LIS surface. For dep-nc-LIS-50, percentage of drops having diameter < 500 μm decreased from ~ 98 % (at the beginning of condensation) to only ~ 93 % (towards the end of condensation), and for dep-nc-LIS-500 from ~ 91% to ~ 82%. As expected, the reduction was more prominent for flat Si-LIS (from ~ 80% to ~ 61%).

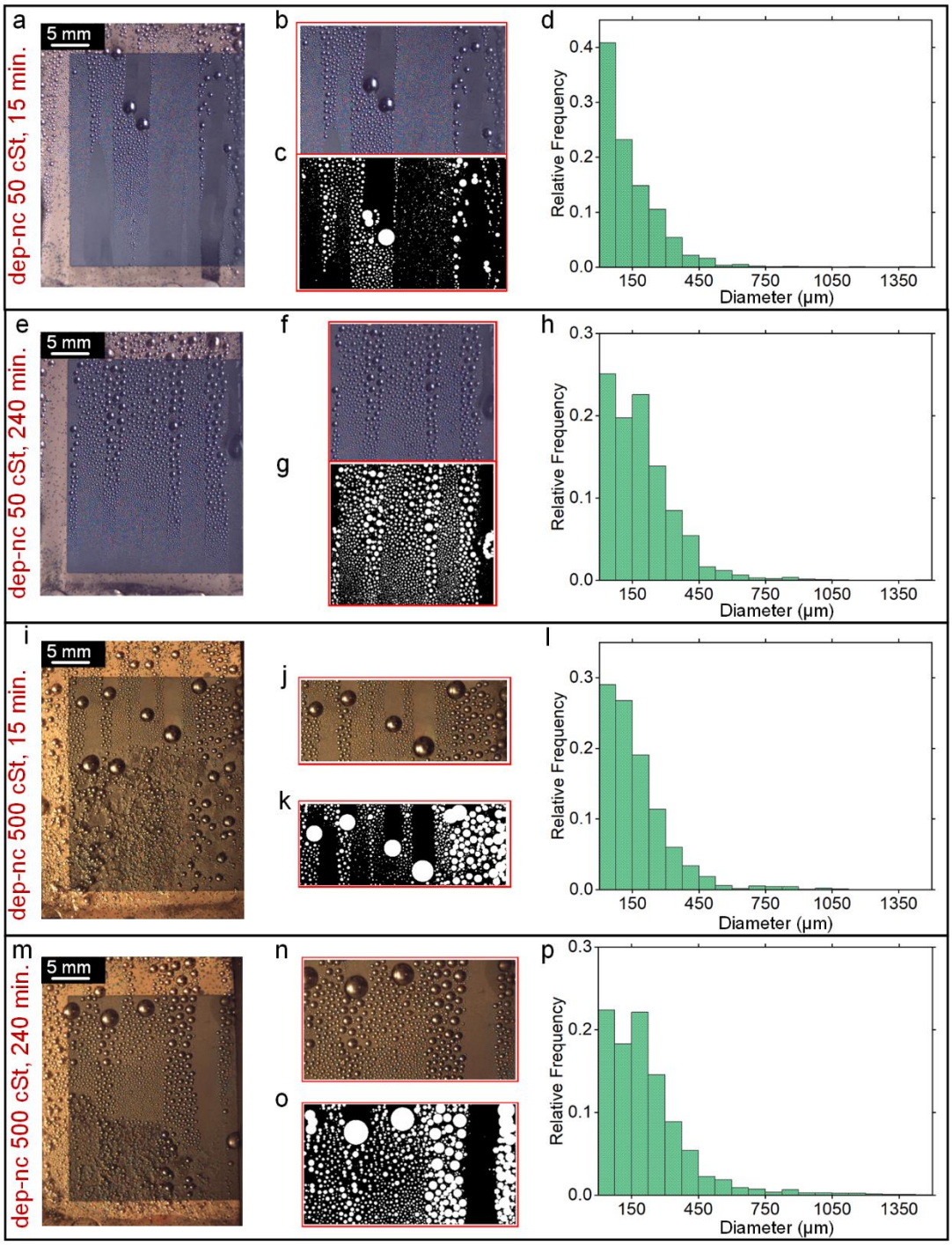

Figure 2.8. Drop size distribution for a selected region on nanochannel depleted liquid infused surface (dep-nc-LIS) samples during experiment for dep-nc-LIS with 50 cSt oil after (a-d) 15

minutes, and (e-h) 240 minutes of condensation. Similarly, drop size distribution on dep-nc-LIS with 500 cSt oil after (i-l) 15 minutes, and (m-p) 240 minutes of condensation.

For the second set of experiments, condensation on fresh LIS on porous nanochannel sample with 50 cSt silicon oil (nc-LIS-50) was conducted for total of 3 days in two phases over a period of 18-days. The first phase of the experiment included continuous condensation over the first day (24 hours), followed by 15 days of keeping the sample as-is in the experimental setup and still under ambient conditions. Second phase involved 2 days (48 hours) of continuous condensation on the same nc-LIS-50 sample. Heat transfer coefficient variation for nc-LIS-50 is shown in Figure 2.9a and respective variation of ambient chamber temperature (T_{amb}), average sample temperature ($T_{sample,avg}$), thermal fluid temperature at cold plate outlet ($T_{fluid,out}$) and thermal fluid temperature at cold plate inlet ($T_{fluid,in}$) during condensation is shown in Figure 2.10. The average heat transfer coefficient in first four hours of experiment was: 1.83 ± 0.11 $Wm^{-2}K^{-1}$, which is similar to reported values[124,151,152] for condensation in presence of NCGs. However, variation in HTC on day 1 (Figure 2.9a), where HTC appears to increase in contrast to reported studies that show a continuous drop in HTC as the condensation progresses, could be an indication to unique wettability feature of porous nanochannel LIS. Due to the low thermal conductivity (~ 0.6 $W/m^{-1}K^{-1}$) of silicon oil which acts as a thermal barrier, extra thickness of oil on the surface of freshly prepared LIS is unfavorable for heat transfer. Therefore, HTC is seen to improve because the underlying porous substrate can still retain necessary oil and maintain hydrophobic properties while extra oil on the surface depletes (Figure 2.3d), thus facilitating quicker condensate shedding from the surface. This explains why the average HTC in final 4 hours of condensation (2.12 ± 0.02 $Wm^{-2}K^{-1}$) on day 1 was around ~ 16 % higher than the initial 4 hours of HTC and nearly as high as HTC (2.33 ± 0.42 $Wm^{-2}K^{-1}$) of dep-nc-LIS-50 (Figure

2.5a). After the first day of experiment, the LIS sample was kept in an open lab environment for 15 days before condensation once again was started on day 17 and continued for 2 additional days. It is important to note that for these experiments, which span over multiple hours, water level in vapor generation system was maintained by a temperature-controlled feedback-based pump circuit unlike manual intervention in case of condensation on depleted LIS. Variation of HTC on nc-LIS-50 for the last 2 days (days 17 and 18) is shown in Figure 2.9a. Cumulative effect of oil depletion during day 1 experiment, surface contamination, and oil depletion due to gravity over 15 days can be seen in lower average HTC value of 1.46 ± 0.16 $Wm^{-2}K^{-1}$. Over the total 3 days of condensation on nc-LIS-50, the shedding condensate drop size was observed to increase (Figure 2.9b), but the nc-LIS surface maintained dropwise condensation, never transitioned to filmwise condensation, and remained hydrophobic (WCA~104^{o}) at the end of experiments, thus showing the potential applicability of our LIS samples for real-world applications.

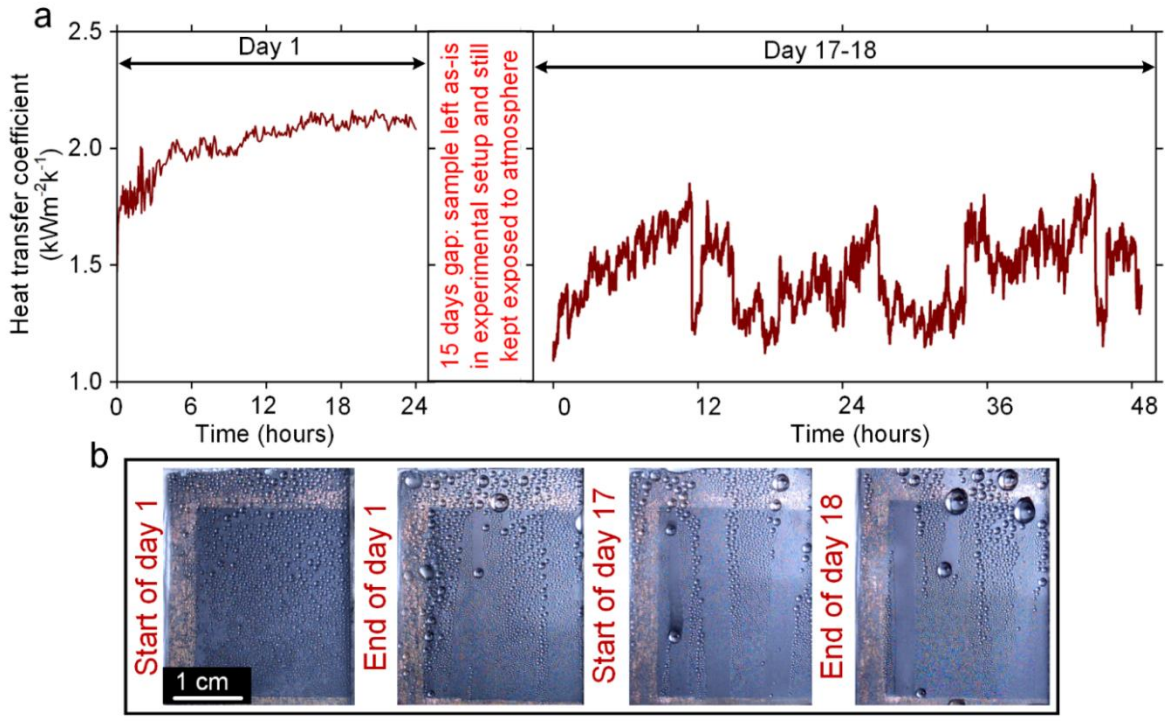

Figure 2.9. Condensation of water vapor on freshly prepared liquid infused surface on porous nanochannel with 50 cSt silicone oil: (a) variation of heat transfer coefficient (HTC) for total of 3 days of condensation over an 18-day period and, (b) drop visualization at different times during condensation experiment.

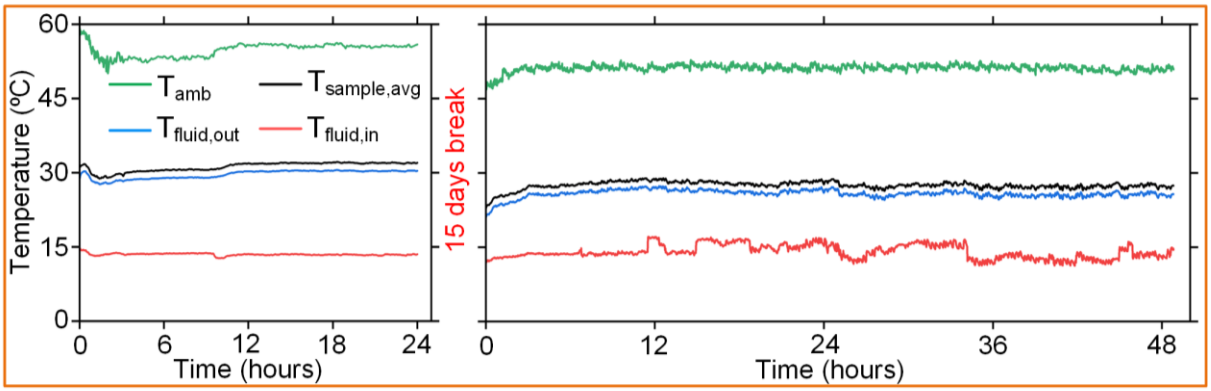

Figure 2.10. Variation of ambient chamber temperature (T_{amb}), average sample temperature ($T_{sample,avg}$), thermal fluid temperature at cold plate outlet ($T_{fluid,out}$) and thermal fluid

temperature at cold plate inlet ($T_{fluid,in}$) during condensation for freshly prepared LIS on porous nanochannel with 50 cSt oil

2.4 Summary

Condensation heat transfer on liquid infused surfaces (LIS) necessitate seemingly conflicting requirements of high sliding velocity and low lubricant depletion. Although, oil depletion can be mitigated to some extent, it has been established by reported studies to be omnipresent in lubricant infused surfaces, eventuating in gradual decline of heat transfer performance. In this chapter, porous nanochannels wick based lubricant infused surfaces (nc-LIS) show excellent drop mobility (roll-off angle ~1^o) and demonstrate improved condensation heat transfer performance in presence of non-condensable gases. Non-toxic, immiscible silicone oil of different viscosities functioned as lubricating medium in the porous substrate. Based on the comparison of four different silicone oil viscosities, it was observed that higher silicone oil viscosity nc-LIS exhibited prolonged retention on the surface, but the drop sliding velocity was significantly lower compared to nc-LIS with low viscosity silicone oil. nc-LIS using 50 cSt and 500 cSt silicone oil are shown to provide substantial improvement in condensation heat transfer coefficient (HTC ~ 2.33 $kWm^{-2}K^{-1}$ for 50 cSt and 1.66 $kWm^{-2}K^{-1}$ for 500 cSt) even in depleted conditions, and no significant change (ΔWCA~3^o) in contact angle was observed for such LIS samples. Improved performance can be attributed to oil being held inside nanochannels, and thus retained on the surface, due to capillarity and improved adhesion owing to plasma cleaning. Drop size distribution study reveals more than ~ 95 % of all drops had a diameter < 500 µm as evident from videos captured at different instances throughout the experiment. Experiment conducted on flat silicon surface with 50 cSt oil under depleted condition shows lack of adequate oil on surface as multiple coalescence of condensate occurs before drop departure which led to only 28% of

drops having diameter < 250 µm and 61% of drops with diameter < 500 µm. Condensation on fresh nc-LIS with 50 cSt silicone oil for 3 days revealed an improvement in heat transfer coefficient of 16% from the start of condensation (0-4 hours HTC: 1.88 ± 0.11 $Wm^{-2}K^{-1}$) towards the end of first 24 hours (20-24 hours HTC: 2.12 ± 0. 02 $Wm^{-2}K^{-1}$), as extra oil depletion reduced the thermal barrier for condensation heat transfer while the porous geometry retained the necessary oil to keep the surface hydrophobic. After a 15-day gap during which the sample was kept exposed to ambient conditions, steady state HTC was attained over the last 2 days of experiments with an average value: 1.46 ± 0.16 $Wm^{-2}K^{-1}$. Over the course of this long experimental duration, the sample maintained dropwise condensation, never transitioned to filmwise condensation, and remained hydrophobic with WCA ~ 104º at the end of condensation. We anticipate that the presented LIS preparation approach can be implemented on large scale porous surfaces for heat transfer-based applications with improved performance even under depleted conditions. Moreover, design of such system could be tailored to suit the needs of variety of applications such as drag reduction surfaces or in medical field to generate inert, non-toxic, and non-adhesive surfaces.

Chapter 3: Superhydrophobicity using Porous Nanochannels

3.1 Introduction

Despite substantial advancements in development of artificially engineered superhydrophobic surfaces (SHS), durability and regenerative aspect of such surfaces remain elusive. A typical fabrication process of a functional SHS requires two important steps, namely, modification of surface roughness usually achieved by methods such as sol-gel[153], etching[154,155], lithography[156], and plasma treatment[157] followed by treatment of the fabricated surface with low surface energy coatings[158]. However, harsh working condition, especially extreme exposure to water or humidity deteriorates plastron property of superhydrophobic surfaces rendering them inappropriate for prolonged under water applications. Recently, candle soot (CS)-derived carbon nanoparticles (CNPs) have been employed as an effective coating to produce SHS. CS particles are usually regular shaped and uniform, its fractal like structure traps sunlight resulting in good photothermal performance essential for iceophobic characteristics. Low cost, readily available, biocompatible[159,160] and multifunctional[161] CS has prompted several studies[162–170] utilizing CS coating for fabrication of SHS with WCA in excess of 160° and ROA as low as 2° .

Irrespective of fabrication procedure, performance testing of SHS is critical in assessing their suitability to practical applications. Usually, performance of any SHS is evaluated by performing numerous durability tests including chemical stability[48], anti-icing[54], mechanical abrasion[56], thermal stability[162], and water drops/jet impact test[168,170]. Nevertheless, other important durability parameters such as long term plastrons[171] (underwater durability), and regenerative property of such surfaces are either limited or remains unexplored[172–174]. Plastron test refers to submersion of SHS and subsequent manifestation of silver appearance due to air

trapped in textured-surface voids which resembles respiration plastrons on some aquatic insects[175]. The deterioration of silver appearance indicates surface losing its superhydrophobic characteristics. While in engineered surfaces plastrons eventually collapse, some insects have evolved with non-wettable hairs for long lasting plastrons[175]. Thus, it important to have engineered surface which can provide durable plastron property and long-term stability under various operating conditions.

This chapter reports a systematic approach for creating a durable superhydrophobic surface by first plasma-treating a fabricated porous nanochannel geometry on a silicon substrate followed by infusion-depletion of silicon oil and coating a layer of carbon derived from candle soot. The infusion and subsequent depletion of non-toxic silicon oil in a plasma treated superhydrophilic porous silicon substrate generates a hydrophobic slippery liquid-infused porous (SLIP) base. The chemical reaction of silicon oil polymer chain (polydimethylsiloxane) with inorganic silicon substrate[176] results in traces of silicon oil being retained on the surface maintaining its hydrophobic property even after severe gravity and shear depletion of oil. Further coating of this hydrophobic surface with candle soot transforms it into a superhydrophobic surface, termed as np-SHS (nano-porous superhydrophobic surface) in the remainder of text. The surface is capable of maintaining water contact angle (WCA) of nearly 160° and roll off angle (ROA) less than 5° after undergoing 20 different tests including mechanical (tap water jet up to ~ 10.3 ms^{-1}), tape peeling test up to 12 cycles), chemical (saline and solvents immersion), thermal (high temperature exposure), self-cleaning tests, organic compatibility (honey, soy sauce, chocolate syrup, all-purpose flour) and superoleophilic test, thus exhibiting potential real-world applications. The surface retains stable plastron with negligible change in WCA and ROA even after being under 10 cm of water for 30 days, similar to respiration plastrons seen on some

aquatic insects. Moreover, heat transfer characteristics such as ice delay (up to 540 sec), frost-defrost cycle (for 14.75 hours, temperature range: -25℃ to 10℃) photothermal property (solar exposure from 0.5 to 1.5 kWm^{-2}) and drop wise condensation are reported here. Besides excellent water repellency, current sample derives its regenerative property by recovering its superhydrophobicity from degraded state by cleaning, oil reinfusion-depletion followed by carbon coating.

3.2 Methodology

Porous samples (Figure 3.1a) were fabricated in a square region (14 mm) on a 500 µm thick silicon substrate by following procedure mentioned in chapter 2 (additional details in Appendix A1). Preparation (Figure1b) of np-SHS starts with standard chemical cleaning procedure of the porous nanochannel sample which is hydrophilic (WCA ~14° , Figure 3.1b) followed by 10 minutes of plasma cleaning and subsequent flooding of nanochannels with 500 cst silicon oil (polydimethylsiloxane) to form a SLIP surface. It is important to note that plasma treatment of the surface was found to improve the durability of prepared surface. Infused sample is then placed in a convective oven overnight at 150℃, following which oil depletion is carried out first by gravity and then placing the sample under running water (jet velocity ~ 4.1 ms^{-1}) for 5 mins. The sample is again kept in convection oven at 150℃ for 30 mins. Candle soot was used as a source for depositing carbon on the hydrophobic depleted SLIP surface (WCA ~122°, Figure 3.1b). The surface was held over a candle flame for approximately 60 s such that the “black smoke” (soot) from candle flame gets uniformly deposited. Excess fragile soot particles deposited on the surface are removed by placing coated sample under running tap water (~1 ms^{-1}) for 1 minute resulting in a layer of soot adhered to the SLIP surface (Figure 3.1b). Repeatability of current methodology is evident from WCA values obtained in excess of

160° and water drop roll of angle ~ 2±1° for more than 30 samples prepared. Further, it was found that np-SHS performed superior when compared to the SHS prepared on (a) porous surface without oil infusion-depletion, and (b) flat silicon wafer with oil infusion-depletion by adopting same preparation procedure.

Surface morphology obtained from atomic force microscope (AFM) for different scanning area size is shown in Figure 3.1c,d. Average roughness (R_a) for 10 µm region (Figure 3.1d) and 500 nm region (Figure 3.1d) was 431 nm and 99 nm, respectively. Root mean squared roughness (R_q) for the same regions were 586 nm and 146 nm.While the superhydrophobicity of surfaces is a consequence of air trapped in textured surface at three phase contact line resulting in reduced contact area between liquid and solid, non-uniform roughness in surface morphology can hinder the drop mobility leading to higher ROA due to pinning action[177]. The cross-sectional scanning electron micrograph (SEM) (Figure 3.1e) for np-SHS shows stable ~15 µm thick carbon coating. Observation of SEM images (Figure 3.1f,g) at different resolution reveals highly porous coating with interconnected soot particles having width around 30-60 nm. Study of elemental composition performed using X-ray spectroscopy (EDS) at three different locations on the surface (Figure 3.1h) substantiate uniform presence of elements of carbon (~ 55 %), oxygen (~ 19 %), and silicon (~ 24 %). Carbon and oxygen constitute candle combustion product while presence of silicon can be attributed to the diffusion of silicon oil from underneath the soot layer. Moreover, investigation of the regenerative property of sample i.e., ability to restore superhydrophobicity from a degraded np-SHS state by methodical cleaning, oil infusion-depletion and carbon coating, resulted in recovering consistent WCA (~ 161°) and roll-off angle (~ 3±1°) tested for six cycles (Figure 3.1i). The regenerative capability of a sample is defined as ability to restore its superhydrophobic characteristics from a degraded state for multiple cycles.

In present study, regenerative ability is demonstrated by: (a) forced degradation of coating after a durability test on the np-SHS, (b) chemical cleaning of degraded np-SHS followed by plasma cleaning, (c) observation under microscope to check cleaning effectiveness, and (d) wettability test of cleaned porous sample followed by drying of sample in convection oven which results in attaining the original state of superhydrophilicity. The superhydrophobic surface can be regenerated by again following the procedure, mentioned above in this section, of oil infusion, depletion, candle soot coating followed by washing the sample under tap water.

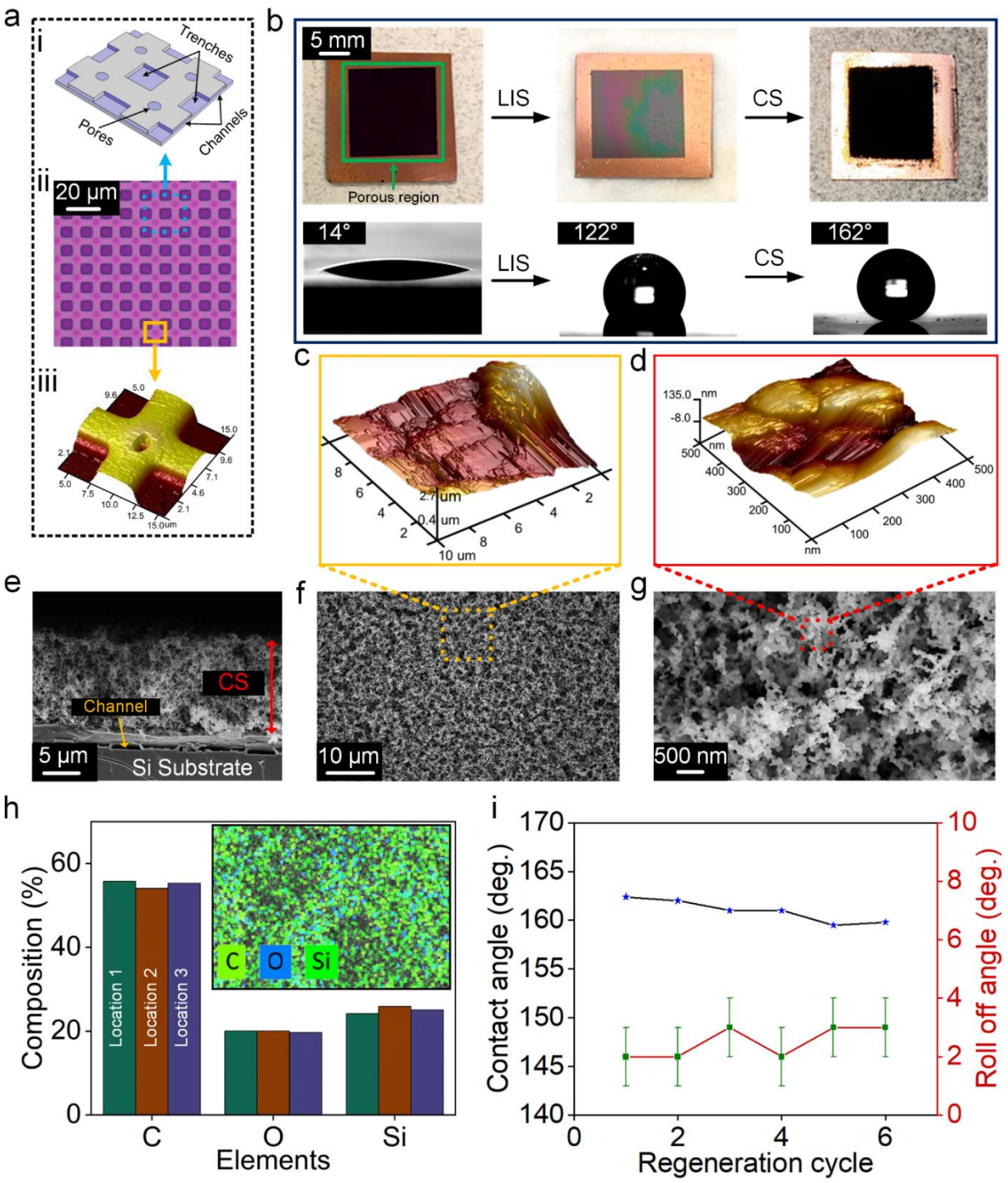

Figure 3.1. Sample preparation, morphology characterization and regenerative property: (a) (i) Three-dimensional schematic of a porous sample unit cell comprising of four pores (diameter: 2 μm), intersecting channels (height: ~ 728 nm, width: 5 μm) and trenches, (ii) Micrograph of

porous sample, (iii) Atomic force microscope (AFM) image at channel intersection depicting pore (b) Sample preparation process from clean and porous sample to depleted SLIP surface to carbon-soot coated superhydrophobic surface, termed np-SHS. Water contact angle variation during the process is also shown. AFM image of typical (c) 10 μm region and (d) 500 nm region of np-SHS (e) Cross-sectional scanning electron microscopy (SEM) image showing carbon soot anchored to the porous base. Typical SEM image at (f) lower magnification and (g) higher magnification of the surface (h) Energy dispersive X-ray spectroscopy (EDS) for analyzing elemental composition at three different locations on the surface with inset image showing color coded distribution of carbon, oxygen, and silicon (i) Regenerative superhydrophobicity of np-SHS conducted over six cycles showing minimal variations in water contact angle and roll of angle[178].

3.3 Results

Examination of water drop adhesion on the surface by pushing it against the np-SHS is shown in Figure 3.2a which further confirms its superhydrophobic behavior. Although previous studies[50,173] on general SHS have performed plastron test by submerging such surfaces underwater, it is limited by both in time (typically < 10 days) and depth of immersion (typically < 5 cm); both parameters have considerable effect on the robustness of any SHS. Hence, plastron test was performed by keeping np-SHS under 10 cm of tap water for 30 consecutive days. The silver appearance, resulting from tapped air on the surface, remains noticeable even after 30 days (Figure 3.2b). WCA (159°) and ROA ($3\pm1°$) measurement after 30 days (Figure 3.2c) confirms the robustness of np-SHS under such extreme exposure to water. Immediately after the plastron test, the same sample was kept in air (inside laboratory) for an additional 150 days. Variation in WCA and ROA for the total 180 days is shown in Figure 3.2c. While WCA

was mostly intact at 154°, ROA (11±1°) deteriorated due to contact line pinning towards the end of 180 days. Surface durability test was performed by observing coating stability under shear imparted by running tap water jet from a nozzle of diameter 4.6 mm. WCA and ROA variation during 600 sec of water flow (velocity ~ 1 ms^{-1}) is shown in Figure 3.2d. Continuous higher flow rate tests (up to velocity ~ 10.3 ms^{-1}) were also conducted. These tests incur no noticeable change in WCA (159°) and ROA (3±1°). Standard pancake bouncing[179] on np-SHS was confirmed by observing a water drop of volume ~ 10 ±2 µl falling from a height of 4 cm. Bouncing of drop exhibited typical behavior[180] on np-SHS such as Worthington jet and secondary droplets upon rebound with total contact time of the drop with surface being 12.8 ± 0.6 ms.

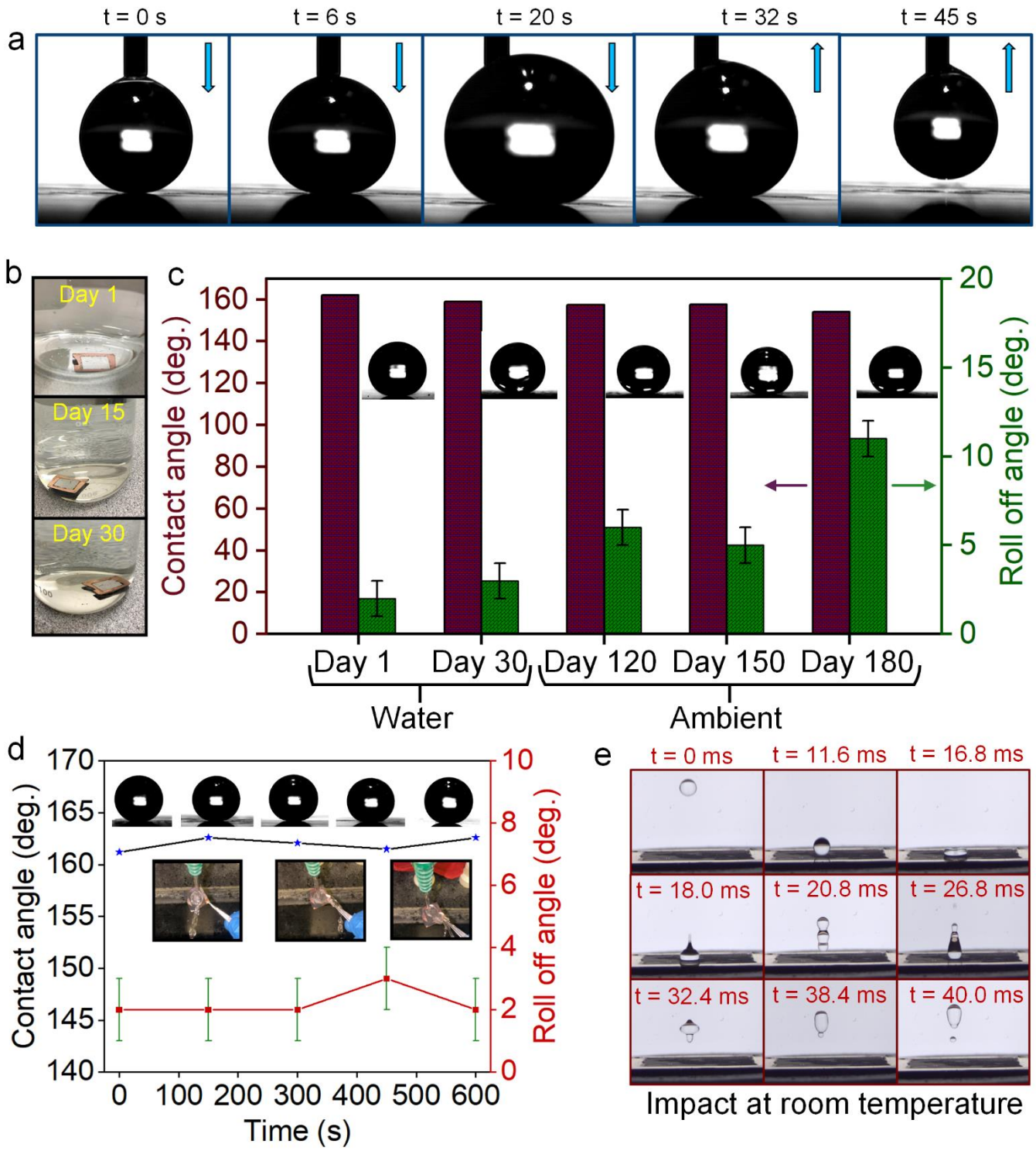

Figure 3.2. Superhydrophobicity and robustness of nano-porous superhydrophobic surface (np-SHS) (a) Water drop being pushed against the np-SHS surface (b) Plastron layer on surface

under 10 cm of water for day 1, day 15 and day 30, respectively (c) Water contact angle (left Y-axis) and roll of angle (right Y-axis) variation for total of 180 days (30 days under water followed by 150 days in ambient air) (d) Variation of water contact angle and roll of angle during tap water jet shear test for 600 sec under flow rate of ~ 1 ms^{-1}(e) Impingement of water drop (volume ~10 ±2 µl) on np-SHS at room temperature[178].

Thermal stability test was performed by heating np-SHS to temperatures up to 300℃, at 50℃ intervals, and keeping it at those temperatures for a period of 600 sec. The sample was cooled back to room temperature after each interval and measurement of WCA and ROA was carried out as shown in Figure 3.3a. Results indicates stable superhydrophobic properties making current sample suitable for high temperature applications. Adhesive strength of CS coating with silicon base was analyzed by using a tape peel test. A total weight of 207 gm was used on the tape applied on np-SHS as an external force (Inset, Figure 3.3b). Peeling off the tap after a waiting period of 120 s constituted one cycle. Variation in WCA and ROA after 20 such cycles is shown in Figure 3.3b. The coating residue on tape and sample condition after peeling cycles are reported in Appendix A2. Amount of soot particles coming off in successive tape peeling diminishes and sample attains WCA of 156° with ROA of 8±1° at the end of 20th cycle. UV light is known to alter surface wettability; thus, to assess the same, np-SHS was exposed to 5 W UV light source, Appendix A2) for a duration of 24 hours without observing any wettability deterioration (Figure 3.3c). WCA and ROA variation for sample submerged under 10 cm of artificial saline solution (35 gm NaCl in 1 liter of tap water) as well as under 5 cm of different solvents (acetone, ethanol) for 15 days (Appendix A2) for all cases is shown in Figure 3.3c. While low surface tension solvents wick into the np-SHS when submerged with no sign of plastron, wettability recovery is observed after sample is isolated and left overnight to allow

complete evaporation of solvent. Acidic (PH 1, 0.1 M HCl) and basic (PH 13,1M NaOH) tests show that while basic solution maintained contact angle (CA) of 154°, HCl drop although exhibiting CA of 141° at the beginning of contact angle measurement, later (~ 100 seconds) reacted with carbon underneath and wicked into porous soot. Further plastron test of acid tested sample reveals surface degradation due to highly corrosive HCl drop. To force deterioration of a sample high power ultrasonication was performed at 40 kHz; interestingly, the surface remained intact till 7.5 minutes as observed by WCA and ROA measurements, but beyond which a gradual increase in WCA is observed, reaching 154° after 15 minutes and the water drop getting pinned after 12.5 minutes indicating surface deterioration.

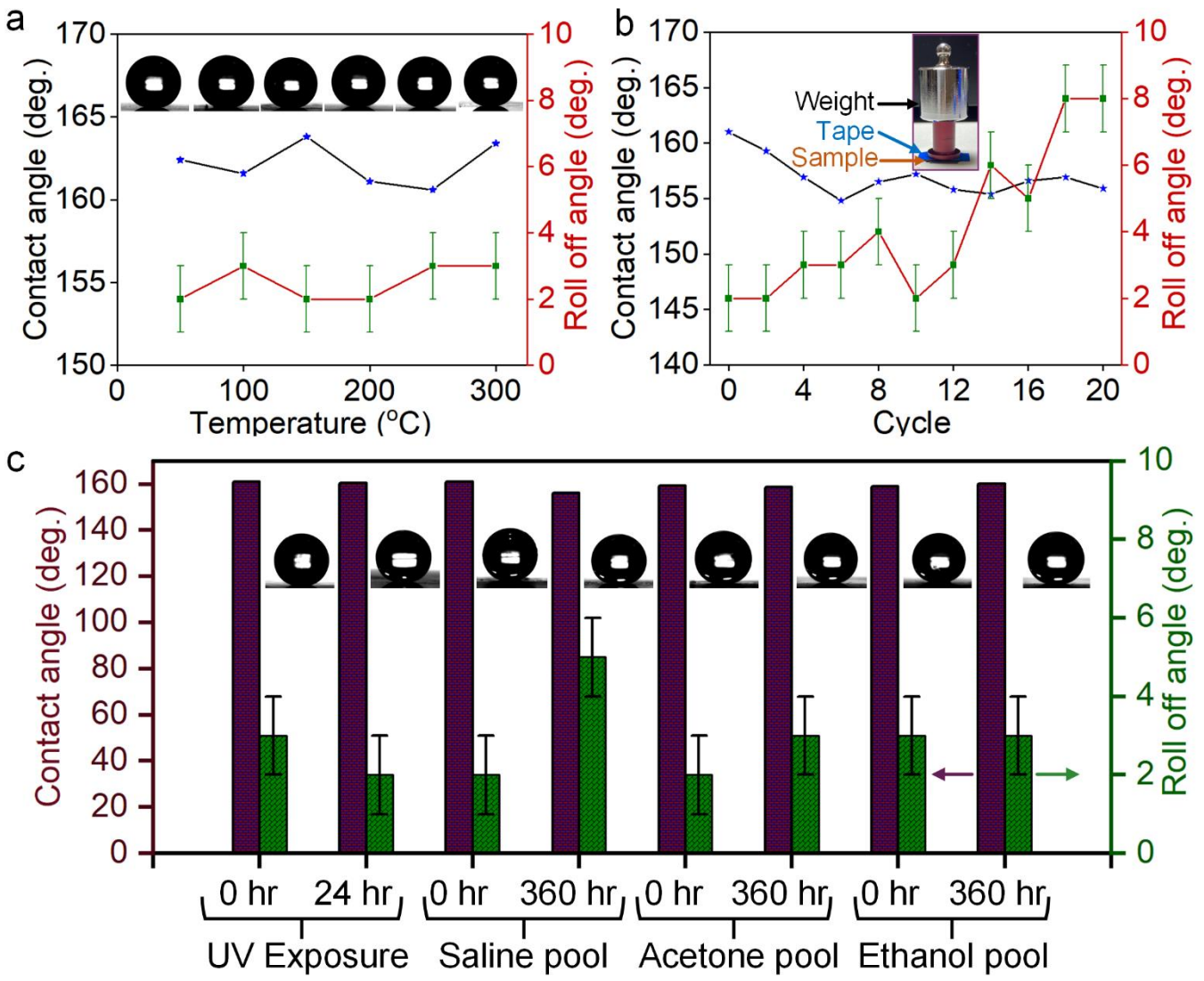

Figure 3.3. Thermal, mechanical and chemical stability of nano-porous superhydrophobic surface (np-SHS) (a) Water contact angle (left Y-axis) and roll of angle (right Y-axis) variation post-heating of np-SHS up to temperatures of 300℃ (b) Tape peeling test with general purpose vinyl adhesive tape. Changes in water contact angle and roll of angle indicate robustness of sample for 20 cycles of tape application (c) Water contact angle and roll of angle variation after 24 hours of 5 W UV exposure, 360 hours of sample being submerged under 10 cm of artificial saline solution, 5 cm of acetone pool and 5 cm of ethanol pool[178].

Another interesting feature of SHS surfaces is delayed ice formation. This test was carried out on np-SHS by placing a 15 µl water drop on a sample maintained at -10°C. As shown in Figure 3.4a, np-SHS shows icing delay of ~ 540 s under ambient condition of 42% relative humidity and 23°C room temperature. Frosting on any surface including SHS is inevitable at low temperature, it can only be delayed making such surfaces suitable for aviation and heat transfer applications. In such scenario integrity and stability of coating structure become crucial. To test the same, 125 frosting-defrosting cycle (Figure 3.4b(i),(ii)) were performed over a period of 14.75 hours. Each cycle duration was ~ 425 s, consisting of ~ 200 s of sample maintained at ~25°C to observe frost growth and subsequent defrosting (Figure 3.4b(ii)). Few of the 125 cycles of sample temperature variation during experiment are shown in Figure 3.4b(i). WCA and ROA measurement shown in Figure 3.4b(iii) indicate unaltered wettability and stability of surface coating following hours of frost growth and defrost. The experimental setup for frost-defrost test is shown in Appendix A2. The photothermal response of np-SHS was captured by exposing surface to artificial sunlight at various heat flux (0.5 kWm^{-2}, 1 kWm^{-2} and 1.5 kWm^{-2}) from a solar simulator (Appendix A2). 1 sun (1 kWm^{-2}) illumination resulted in surface temperature reaching ~ 65°C with calibrated emissivity of 0.94 as shown in Figure 3.4c. High emissivity of such surfaces would trigger melting near surface-ice interface, thus facilitating easy removal of ice nuggets at the early ice incipience phase. These features of np-SHS could be beneficial for designing anti-icing surface coatings. Moreover, np-SHS promotes drop wise condensation (inset, Figure 3.4d) resulting in average heat transfer coefficient (HTC) of 2.7 $kWm^{-2}K^{-1}$ in presence of non-condensable gases. Variation of HTC and surface supercool (difference between ambient and surface temperature) during experiment is shown in Figure 3.4d. The average relative humidity and ambient

temperature of the condensation chamber was 59.8 % and 42.4℃ during 90 minutes of the experiment.

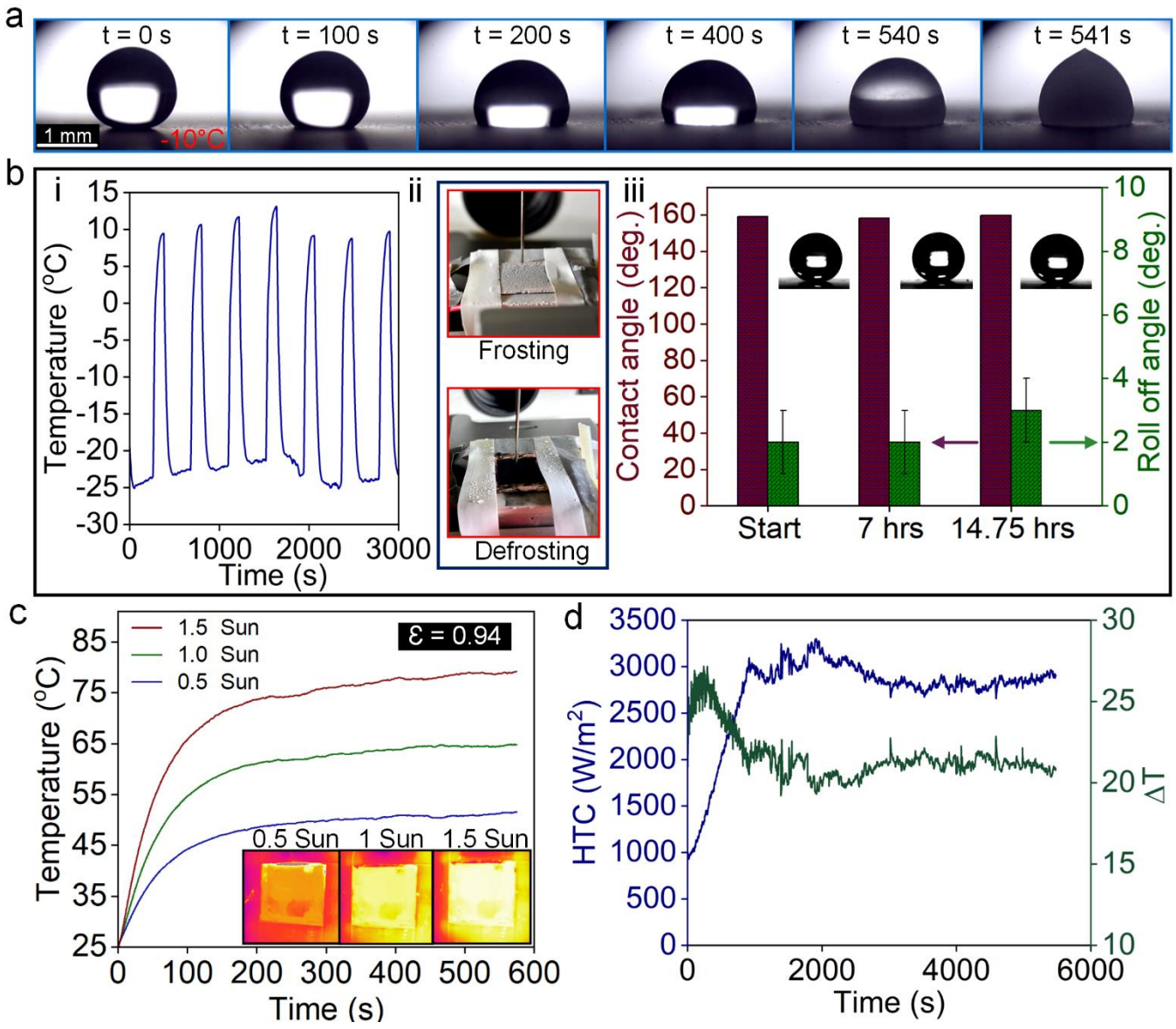

Figure 3.4. Heat transfer characteristics of nano-porous superhydrophobic surface (np-SHS) (a) Delayed freezing (~ 540 s) of a 15 µl water drop on sample maintained at -10℃ (b) (i) Cyclic variation of sample surface temperature during continuous frosting-defrosting test in environment with room temperature 23℃ and 42 % relative humidity, (ii) Sample condition

during frost and defrost state, (iii) Variation in water contact angle (left Y-axis) and roll of angle (right Y-axis) during 14.75 hours of frosting-defrosting test (c) Photothermal response for various heat flux reveals high emissivity of 0.94 and surface temperature reaching ~ 65℃ under 1 sun (1 kWm^{-2}) illumination (d) Variation in condensation heat transfer coefficient (HTC) (left Y-axis) and temperature difference between SHS surface and the chamber (ΔT) (right Y-axis). Average condensation HTC of 2.7 kWm^{-2}K^{-1} was obtained in presence of non-condensable gases. Inset shows condensate at different time intervals[178].

Further, compatibility of np-SHS with organic materials such as honey (Figure 3.5a), soy sauce (Figure 3.5b), chocolate syrup (Figure 3.5c), fine grain all-purpose flour (Figure 3.5d), milk (Figure 3.5e), canola oil (Figure 3.5f) and oil-water emulsion (Figure 3.5g,h) was also examined. Interestingly, plastron can be seen even in sample submerged in honey as shown in Figure 3.5a. Withdrawal of sample from honey results in a layer of viscous honey to form a temporary film enveloping np-SHS due to adhesion of honey on copper strip around the edge of superhydrophobic region. Film thickness gradually diminishes due to gravity induced depletion followed by sudden rupture revealing unaffected surface as confirmed by WCA (160°) and ROA (2±1°). Soy sauce and chocolate syrup drops behave similar to water drops, not adhering to the surface. Moreover, to test self-cleaning property of np-SHS, the surface was covered with commercially available fine grain all-purpose flour (Figure 3.5d) and subsequently cleaned using tap water. Complete removal of flour was observed with WCA (161°) and ROA (2±1°) remaining unchanged. Figure 3.5e shows a 20 µl milk drop on sample indicating milk-repellency feature of np-SHS. Surfaces used in oil-water separation system[38] usually possess simultaneous superhydrophobic and superoleophilic wetting property. Robust superhydrophobicity of np-SHS and strong affinity for oil as shown in Figure 3.5f,h could be

beneficial for development of a functional oil-water separation system. To test this hypothesis, a ~ 4 µl drop of canola-oil emulsion (20 % v/v) (Figure 3.5g) was placed on np-SHS. Oil appears spreads out (Figure 3.5h) due to oleophilic nature of surface while simultaneously enveloping and forming a visible oil ridge around accumulated water drop at the center (~ 50 seconds), similar to findings reported in literature for typical SHS[181]. To visualize the oil ridges, a water drop was placed on freshly prepared oil infused surface as shown in Figure 3.5i. Distinction between water drop and oil ridges can be observed because of dissolved biocompatible tracer (fluorescein sodium salt) in the water. Due to superhydrophobic and superoleophilic characteristic of the np-SHS, the oil-water emulsion behaves similar to a water drop on oil infused surface. Further investigation and design consideration such as net-like porous structure are required to realize the potential of such surfaces for oil-water separation.

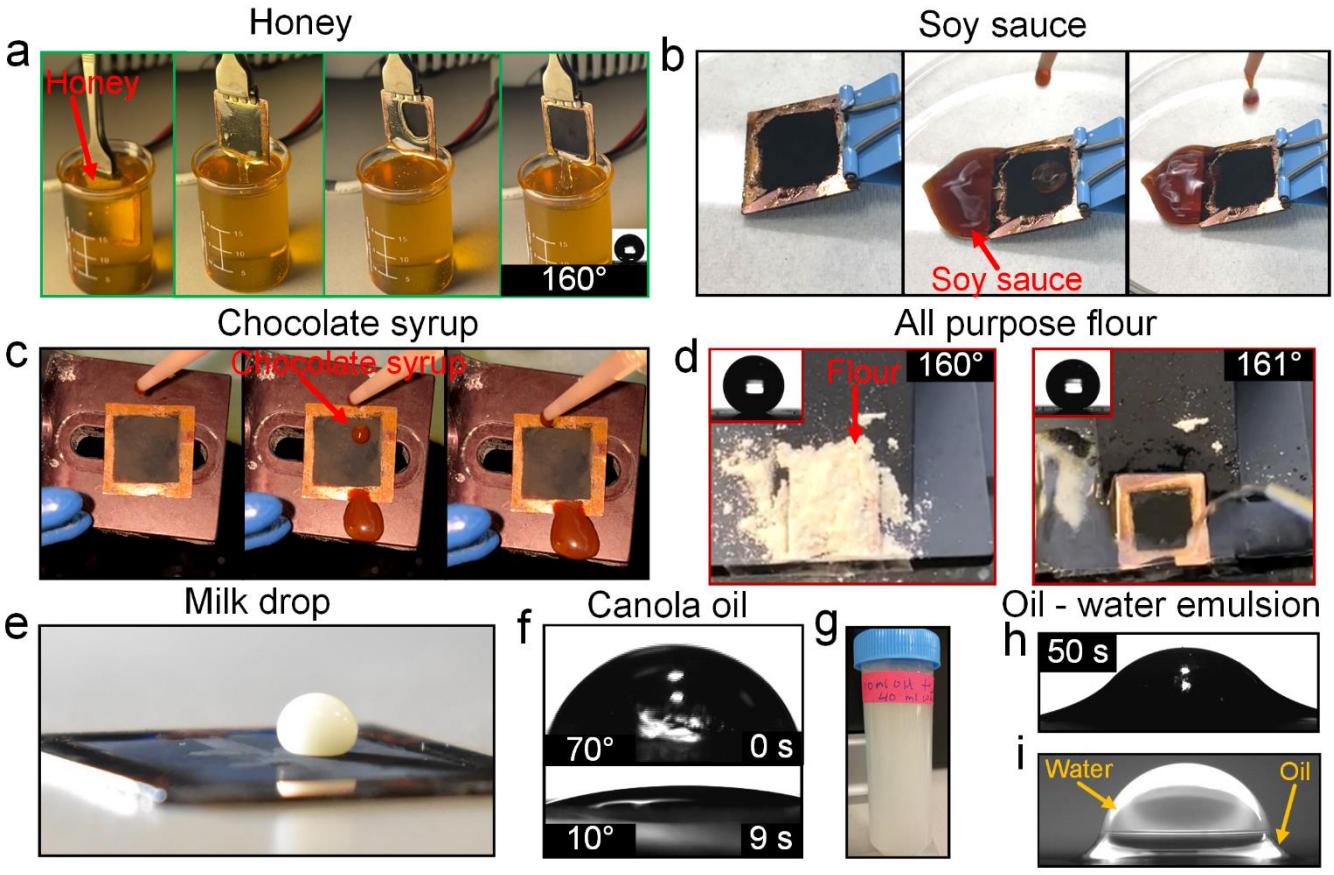

Figure 3.5. Organic materials compatibility and self-cleaning property of nano-porous superhydrophobic surface (np-SHS) (a) Visible plastron layer over sample when dipped in honey. Highly viscous honey stuck along the copper edge of sample enveloping the SHS following a sudden rupture of honey film revealing np-SHS surface (b) Soy sauce drop sliding off the sample with no sign of adhesion (c) Chocolate syrup drop rolling off the sample without any adhesion (d) Sample covered with fine grain all-purpose flour showing self-cleaning feature when washed with tap water without leaving any residue (e) A 20 µl milk drop resting on np-SHS (f) Superoleophilicity behavior over 9 s resting time of canola vegetable oil drop (g) Prepared emulsion of canola oil- water (20 % v/v) (h) Canola oil-water emulsion drop on np-SHS surface showing oil ridges around accumulated water drop (i) water drop on oil-infused surface[178].

3.4 Summary

A systematic approach for creating a durable nano-porous superhydrophobic surface (np-SHS) is presented where cross-connected buried nanochannels, with micropores present at intersections, is used to attain a depleted oil-infused surface, followed by coating it with candle soot. Surface roughness of np-SHS helps in maintaining stable Cassie-Baxter state during multiple durability/performance tests. Numerous successful tests such as prolonged plastron test, tap water jet impact test, adhesive tape peeling test, chemical stability test (immersion in artificial saline water and solvents), exposure to UV radiation and, icing delay, and frost-defrost test were carried out for np-SHS stability analysis. Further, np-SHS demonstrates exceptional durability in harsh conditions, particularly under water, retaining water contact angle (WCA) of 159° and roll of angle (ROA) of $3\pm1°$ after 30 days of continuous submersion under 10 cm of water, and WCA of 154° after subsequent 150 days in ambient air. Impact of tap water jet having velocity of 1 ms^{-1} to 10 ms^{-1} on np-SHS had insignificant effect on WCA and ROA demonstrating excellent mechanical stability of coating. While frost growth usually damages the structural integrity of a typical SHS, WCA (159°) and ROA ($3\pm1°$) measured after 14.75 hours of continuous frosting-defrosting cycles suggest no effect on np-SHS wettability. Dropwise condensation on the surface was also observed with average heat transfer coefficient of 2.7 $kWm^{-2}\ K^{-1}$. Compatibility of np-SHS with organic materials was examined with milk, honey, soy sauce and chocolate syrup while self-cleaning property was evident from complete removal of fine grain all-purpose flour from sample. Another feature of the surface is superoleophilicity which renders np-SHS potentially suitable for oil-water separation systems as implied by preliminary testing with canola oil-water emulsion. Moreover, it was shown that the underlying porous nanochannel geometry allows us to regenerate np-SHS from deteriorated state.

Chapter 4: Porous Nanochannels for Vapor Generation

4.1 Introduction

The consumption of steam has been at the core of technological innovation in the form of steam engine at the beginning of industrial revolution to modern era steam turbine for power generation[182,183]. Energy demand for vapor generation in applications such as desalination of seawater[61,62], low grade waste heat recovery[63,64], humidification[65] and steam sterilization[66] could be met with proper harvesting of renewable energy sources like solar heat flux in an interfacial vapor generation (IVG) device. In such devices vapor generation rate is governed by two primary factors (a) the ease of water transport from bulk to the surface under capillarity and (b) subsequent evaporation at liquid-air interface.

A typical solar based IVG requires three major components: (1) Solar absorber with high absorbance capabilities, also known as photothermal materials (2) Porous material (substrate) designed for continuous water transport from bulk to surface (3) A suitable insulator at the bottom of substrate to minimize heat loss to bulk water without having adverse effect on water transport. Considering poor solar radiation absorbance[184]of water, special design considerations are required to maximize the sunlight absorbance. It has been demonstrated that with a suitable choice of material and fabrication technique even a single material can serve as both an absorber and a substrate.

Photothermal materials follow various solar energy conversion mechanism namely thermally induced lattice vibration, electron generation-recombination and resonance based plasmonic localized heating. A typical lattice vibration mechanism based double layer carbon based absorber[72,76] in which top hydrophilic layer acting as an efficient absorber positioned above an insulating layer have been widely tested. The photothermal materials in electron-hole

generation-recombination based devices are usually metal oxides/complexes[92,93] such titanium oxides, iron oxides, whereas plasmonic heating based vapor generators commonly use nanoparticles[68], carbonaceous materials[90] and semiconductors[91]. They have been found to achieve solar conversion efficiency up to 97 % with vapor generation rate of 2.08 $kgm^{-2}h^{-1}$. Carbon-based substrates enhance water absorption and high porosity favors desirable properties like water transportation, low density, and low thermal conductivity. Considering the abundance, stability and negligible impact on environment, carbonaceous materials[89,185] derived from biomass have been set forth as a suitable choice for vapor generation. It can be inferred that solar vapor generation device design is heavily dictated by two criteria (a) capillary pressure driven wicking of water through the porous substrate from bulk to active evaporation site and (b) simultaneous evaporation rate from liquid-air interface. The later criteria can be fulfilled by utilizing thin-film evaporation which offers significantly higher evaporation rate[97] as compared to free surface evaporation. For the former criteria, a substrate must be designed to offer consistent and reliable wicking. Recently, a study[140] of wicking and evaporation dynamic[186] for a water droplet on cross-connected buried nanochannels has shown a promising result for superior wicking on a hydrophilic surfaces which can be a suitable candidate for IVG device.

This chapter deals with experimental investigation of porous nanochannel wicks for vapor generation. Porous nanochannel wicks facilitates passive water flow from bulk reservoir at the bottom to the pores fabricated along the nanochannel wick through capillary flow. Compared to above mentioned materials and techniques, the current design provides additional liquid-vapor interface along the water flow path. Thus, high vapor generation rate 1.18 $kgm^{-2}h^{-1}$ has been achieved, even in dark condition (without heat input), primarily due to wicking through

channels[140] and nanoscale thin film evaporation in the nanochannels and pores[97,186]. Unlike vapor generating devices mentioned in discussion above, the surfaces of heat input and evaporation surface are separate corresponding to two sides of thin silicon (500 ± 25 μm) sample. Separation of these surfaces offers flexibility in choices of energy input namely solar energy, low grade heat energy like exhaust gases to name a few that can be used with this sample. Moreover, the performance of device was also evaluated using solar simulator mimicking the solar heat flux. It is also shown that the proper selection of coating on heat input side would enhance solar absorption for such system.

4.2 Methodology

Porous nanochannel is fabricated in a 28 mm square region on a 500 μm silicon wafer. The detailed fabrication process of the samples is shown in Appendix A1. After fabricating porous structure on the one side, other side was coated with 90 nm thick indium tin oxide (ITO) film through which a direct current is passed to serve as joule heating layer. A 500 nm thick Cu layer was deposited as electrodes. In a typical sample (porosity = 0.75) with porous nanochannel wicks, there are two sets of parallel 1-D nanochannels (width: 5.75 μm, height: 728 nm) cross-connected to each other, with a micropore (diameter: 2.4 μm) at each intersect. The micrograph, atomic force microscopy (AFM) for single unit cell, and three-dimensional representation of substrate is shown in Figure 4.1a, 4.1b and 4.1c respectively. Cross sectional schematic of sample dipped vertically in the deionized (DI) water reservoir represented in Figure 4.1d (not to scale) depicts the heater position and simultaneous wicking in the channels and evaporation from pores.

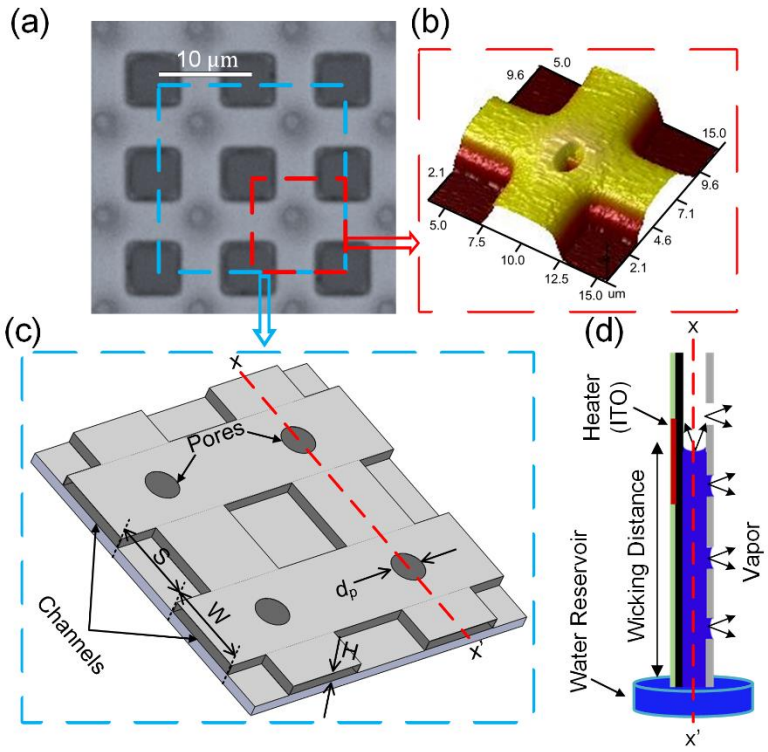

Figure 4.1. Characteristics of nanochannel wicks (a) Micrograph obtained by optical microscope. (a) AFM image of single unit cell. (c) 3D schematic of four-unit cells of cross connected nanochannel wicks. (d) Schematic showing wicking along cross section x-x' in vertically oriented sample dipped in DI water reservoir[187].

The experimental setup shown in Figure 4.2a depicts various apparatus used in experiments. The sample positioning stand is used to hold and position the sample. A cylindrical water reservoir of diameter 90 mm and height 22.8 mm was placed on weighing scale interfaced with a computer to record data at a frequency of 1 Hz. Only openings on reservoir surface were a rectangular (51 mm by 7 mm) slit and four thermocouple openings of diameter 6.2 mm at the top which contributed to free surface evaporation from water. During experiment with solar simulator, the only opening area was 23 mm by 7 mm, since the sample used here was less wide. An infrared thermal (IR) camera for capturing thermal profile and a high-speed camera for visual analysis

were employed on the opposite sides of sample. A programmable DC power supply was used to provide necessary joule heating through ITO and corresponding transient current and voltage were recorded. It was observed that SiO_2 emissivity (ϵ) was extremely temperature dependent which would interfere with the accuracy of the IR camera. Conversely, we used a white vinyl tape (thickness = 0.18 mm) having calibrated constant emissivity of 0.7 over the heating side of sample and on teflon as shown in Figure 4.2b. The front side on sample in Figure 4.2c shows thermocouples dipped inside the bulk water. A data acquisition system in addition to LabVIEW software were used to record temperatures at a frequency of 1 Hz. The solar simulator arc lamp power supply and arc lamp housing was used to simulate the solar heat flux of 1.25 kWm^{-2}.

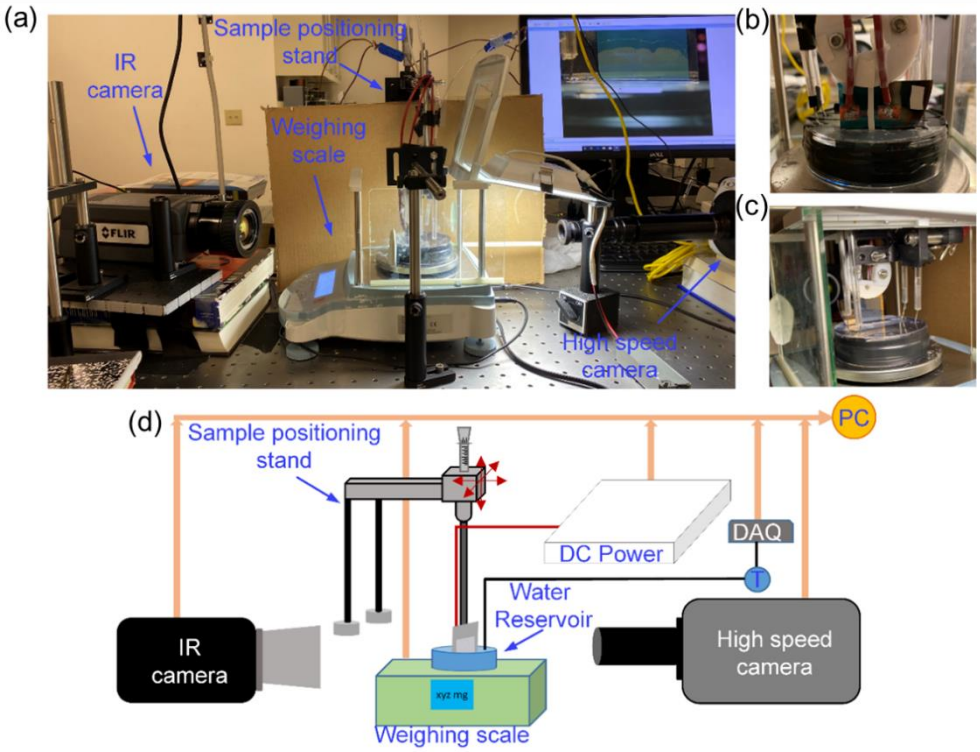

Figure 4.2. (a) Actual experimental setup indicating different components. (b) Heating side as visible from infrared camera. bb) Evaporation side having nanochannel wicks and pores observable from high-speed camera. (d) Schematic of the experimental setup[187].

The schematic diagram of experimental setup with all the components labelled is shown in Figure 4.2d. For experiment with solar simulator, I have used a black enamel paint instead of vinyl tape which had a calibrated emissivity of 0.96 facilitating in enhanced solar absorption. The experiments were performed in controlled environment at 23 ± 0.15 °C and 41 ± 0.25% RH. The top part of sample is first sandwiched between two circular teflon discs which are anchored to sample positioning stand (SPS). SPS provides five (three translational and two rotational) degrees of freedom for proper alignment of sample while dipping into the DI water reservoir placed on digital weighing scale (Figure 4.2a) having computer interface. The resulting loss in weight of water reservoir due to evaporation is recorded by a dedicated software (SPDC) at a frequency of 1 Hz. A high-speed camera positioned in front of evaporation side (Figure 4.2a) records the video of wicking which further undergoes image processing to obtain wicking distance. We used images at a rate of four frames per second for complete 1620 seconds of each experiment. Figure 4.3a shows a sample image during experiment as captured by high-speed camera. The top interface of water wicked into nanochannels is shown as wick front whereas, the free surface of water as water front. Wicking distance is the difference between position of wick front and water front which essentially indicates the extent of water transportation through nanochannels under capillarity. To avoid any error resulting from faulty pixels in images, we choose regions of interest as three boxes shown in Figure 4.3a which covers around 90 % of sample width. Seperating each images into three parts was followed by extracting water front (Figure 4.3b) and wick front (Figure 4.3c,d,e). The average wicking distance of three regions was considered as wicking distance for a particular image.

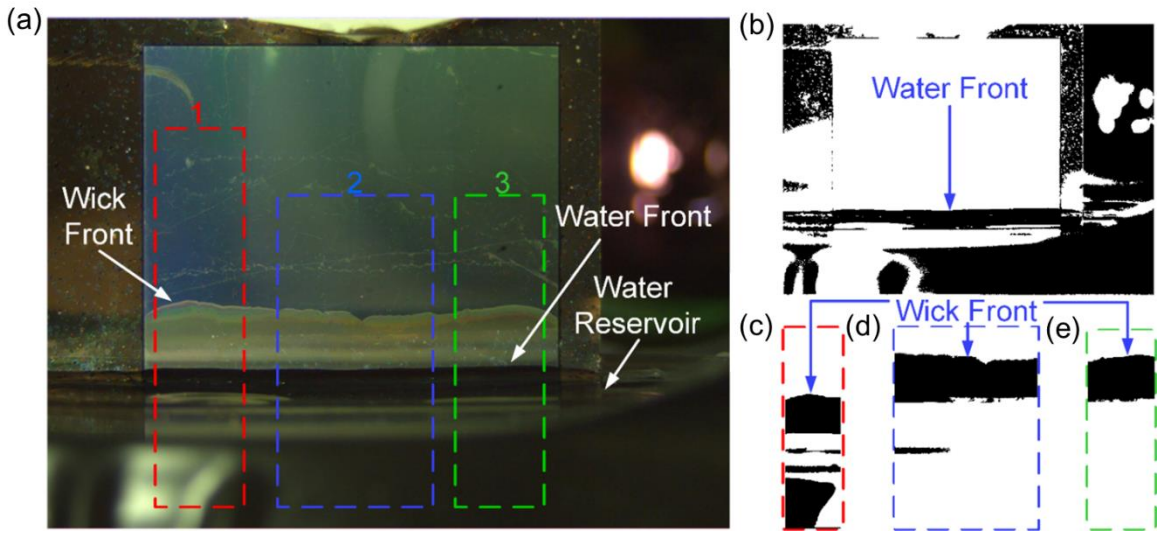

Figure 4.3. Wicking distance calculation (a) Sample of a single frame recorded in high-speed camera showing three boxes (red, blue and green) as region of interest. (b) Processed image showing water front. (c) Wick front for region enclosed in box 1. (d) Wick front for region enclosed in box 2. (e) Wick front for region enclosed in box 3[187].

4.3 Results

4.3.1 Performance of nanochannel wicks in dark environment

To assess the performance of nanochannel wicks exclusively, we first quantified the loss of mass from the water reservoir in petri dish due to free surface evaporation. The petri dish was closed with a cover having well-defined openings to allow insertion of the sample and thermocouples into the reservoir. The mass of evaporated water from the reservoir through the openings, due to free surface evaporation (m_{fs}) was first obtained (without sample dipped in) and was subtracted from the 0 W case (sample dipped in the water reservoir without power input). The enhanced vapor generation was first demonstrated by comparing free surface vapor generation rate from the bulk water in petri dish to that from a sample dipped in water at room temperature (without any heating). The vapor generation rate was obtained using following equation:

$$\dot{m} = \frac{M_{ev,cumulative}}{A \cdot t_{exp}}$$ Equation 4.1

where $\dot{m}$ is vapor generation rate, $M_{ev,cumulative}$ is total mass of vapor generated and t_{exp} is experiment duration (1620 sec for all experiments). In case of evaporation from surface of bulk water, A was fixed as 470 mm^2, while for evaporation from the sample, A was calculated by A= wd_{avg}*w, where wd_{avg} is the average wicking distance calculated over the course of duration and w is the width of the nanochannel wicks region (28 mm). Figure 4.4 shows the temporal plot of the variation of wicking distance and cumulative vapor generation. The vapor generation rate from surface of the bulk water was 0.26 $kgm^{-2}h^{-1}$, which is close to empirical prediction (0.22 $kgm^{-2}h^{-1}$) by Hahne and Kubler[188]. With the presence of the nanochannel wicks, the vapor generation rate was enhanced by ~350% (1.18 $kgm^{-2}h^{-1}$), which can be primarily attributed to the thin film evaporation occurred inside the nanochannels and pores. This vapor generation rate (without any heat input) is comparable to that using CNT's, plasmonic wood, carbon foam and exfoliated graphite in ISVG systems under 1 sun radiation (1 kWm^{-2}) reported in literature (0.9-1.2 $kgm^{-2}h^{-1}$)[76,189–192].

The wicking distance in nanochannel wicks fluctuated constantly, even after reaching quasi-steady state. The fluctuation was primarily due to the competition between continuous evaporation and wicking in nanochannels. Evaporation from the pores causes waterfront to recede, leading to decrease in wicking distance until capillary pressure re-compensates again, leading to the increase in wicking distance as depicted by fluctuation of wicking distance in Figure 4.4.

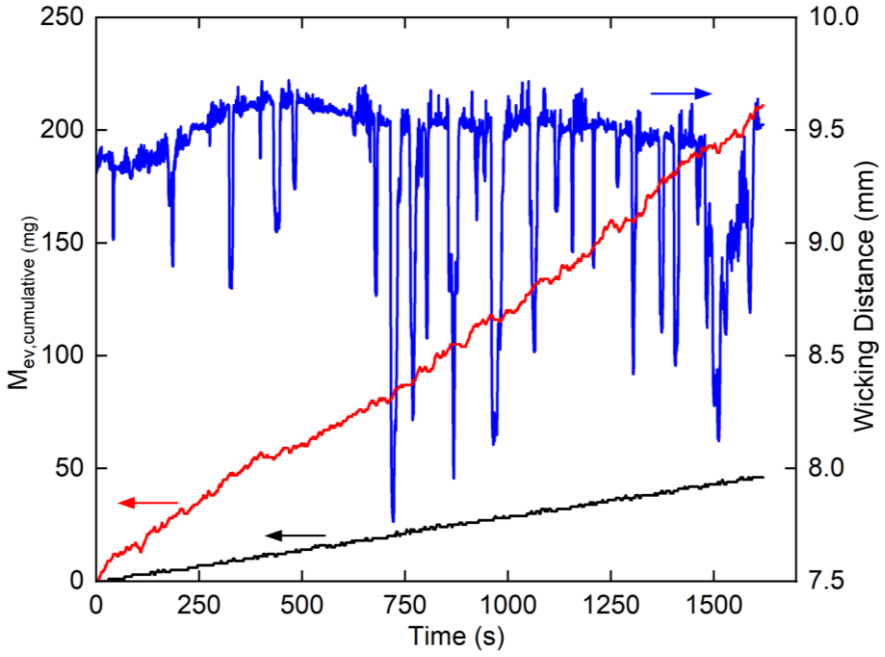

Figure 4.4. Variation of cumulative mass of generated vapor (left y-axis) and wicking distance (right y-axis) with time for vapor generation experiments from free surface of bulk water in petri dish and that from porous nanochannel wick sample dipped in water without any heat supply (0 W)[187].

4.3.2 Performance of nanochannel wicks under resistive/joule heating

We then investigated vapor generation under various heat input. We tested four power levels: 2.01 W, 2.89 W, 3.89 W, and 5.08 W, with corresponding heating flux of 1.5 kWm^{-2}, 2.16 kWm^{-2}, 2.9 kWm^{-2} , 3.80 kWm^{-2}, respectively using following equation.

$$Q''_{in} = \frac{P}{A_{ex}} \qquad \text{Equation 4.2}$$

Where, P (=V*I) is supplied power and A_{ex} (=1137.4 mm^2) is the area of heating side exposed to the ambient. The vapor generation rate increased (4.28 $kgm^{-2}h^{-1}$, 9.68 $kgm^{-2}h^{-1}$, 13.49 $kgm^{-2}h^{-1}$,17.12 $kgm^{-2}h^{-1}$) with increasing heat input. Free surface evaporation (m_{fs}) losses were estimated for each case and subtracted accordingly. However, there existed a critical heat input, above

which enhancement in cumulative mass of vapor generation appears to be insignificant (Figure 4.5a). Similar to the operational limit in thermal management devices related to liquid-to-vapor phase change[193], mass transport is the bottle neck of the device performance. Here, in terms of vapor generation, when the water supply was not sufficient to compensate for enhanced evaporation, wicking distance decreased (Figure 4.5b), leading to a reduction of the number of active pores for evaporation. Figure 4.5c shows the maximum sample temperature throughout the experiment is in the range of 23ºC to 62ºC depending on heat input level. Considering the vapor generation (1-10 kgm^{-2}) at 40-100°C when using various materials based ISVG systems reported in literature[73–76,85–88,91,194], high vapor generation rate was achieved at low temperature with our wicks, thus implying the potential of integrating our current design with heat recovery from low grade energy sources like exhaust gases.

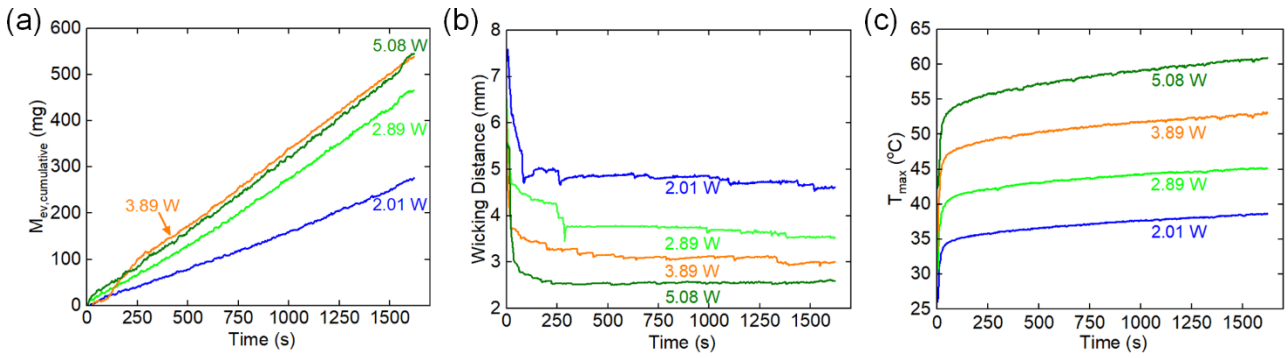

Figure 4.5. Variations of (a) cumulative vapor generation, (b) wicking distance, and (c) maximum temperature observed on the sample with time for heat inputs of 2.01 W, 2.89 W, 3.89 W, and 5.08 W respectively[187].

One important aspect to evaluate vapor generation is its efficiency (η), which is defined as the ratio of evaporation energy to the total input power (Equation 4.3) and the specific vapor generation (m_{sp}), which is defined as the amount of generated vapor per unit heat input (Equation 4.4).

$$\eta = \frac{Q_{ev}}{Q_{total,in}} \quad \text{Equation 4.3}$$

$$m_{sp} = \frac{m_{ev,cumulative}}{Q_{total,in}} \quad \text{Equation 4.4}$$

where $Q_{ev}=m_{ev,cumulative}*h_{fg}$, is evaporation energy and h_{fg} is the latent heat of vaporization of water, $Q_{total,in}$ is the total heat input throughout an experiment.

There are several sources of heat loss such as energy loss to bulk water (Q_{wa}), energy loss to teflon (Q_{tf}), natural loss from sample (Q_{sn}), energy loss due to free surface evaporation (Q_{fs}) and unaccounted losses (Q_{un}). To calculate heat loss to teflon, we performed parametric COMSOL simulation for natural heat transfer coefficient (h), keeping constant ambient temperature as 23°C. The experiments were performed by sandwiching the sample at the bottom of two teflon block such that the bottom edge of sample could be perceived as a chord of length 13 mm on circular face of teflon. The area enclosed between chord and the minor arc i.e., area of teflon covered by sample serves as the input boundary in COMSOL simulations. The 3D teflon geometry is shown in Figure 4.6a. Further, temperature acquired by IR camera at the top edge of box 1 (Figure 4.6c) was used as boundary condition during simulation. The minimization of mean sum of square error between experimental and simulation temperature of a point (P1) on teflon (Figure 4.6c) for all four-power input resulted in h = 1.75 $Wm^{-2}K^{-1}$ (Figure 4.6b). Then, the heat transfer to teflon was evaluated as the sum of heat loss to surrounding via natural convection during experiment ($0 - 1620$ s) and heat stored in teflon at the end of experiment as given by the following equation:

$$Q_{tf} = hA_{tf}(T_{st} - 23) + mc_p(T_v - 23) \quad \text{Equation 4.5}$$

where A_{tf} is total surface area of teflon blocks exposed to ambient, T_{st} and T_v (both obtained from simulation) are the transient average surface temperature and volumetric average temperature (at

the end of experiment) of teflon blocks respectively, m is mass of teflon blocks and c_p is heat capacity of teflon.

The convection heat transfer coefficient for sample was assumed to be same as that of teflon obtained using simulation. Thus, heat loss from sample surfaces on account of natural heat convection was estimated as

$$Q_{sn} = hA_{sn}\left(T_{s,avg} - 23\right) \quad \text{Equation 4.6}$$

where h = 1.75 $Wm^{-2}K^{-1}$(obtained from teflon simulation), A_{sn} is the exposed sample area to ambient, $T_{s,avg}$ is the transient average surface temperature of sample obtained from IR imaging.

In order to calculate the heat loss to water reservoir (Q_{wa}), we implemented a numerical technique by treating it as a inverse heat conduction problem (IHCP) and used space marching algorithm[195] for obtaining heat flux from the sample to the bulk water at the bottom of box 1 (Figure 4.6c). The temperature required for solving IHCP was obtained from two arbitrary points near the bottom of box 2. It was assumed that cross section of sample near the bottom has uniform temperature at any instant during experiment. Energy loss due to free surface evaporation during experiment was obtained by:

$$Q_{fs} = m_{fs}\left(h_{fg}\right) \quad \text{Equation 4.7}$$

Where, m_{fs} is the mass of free surface vapor generated and h_{fg} is latent heat of vaporization of water. Free surface vapor generation was obtained by using relation by Hahne and Kubler[188] using water vapor pressure at average bulk water temperature for each experiment and variation of h_{fg} with temperature was also taken into account. The total free surface vapor generation during the entire period of each experiment was 49 mg, 65 mg, 82 mg, 99 mg and 17 mg for 2.01 W, 2.89 W, 3.89 W, 5.08 W, 1.25 sun, respectively. Performing energy balance on each case resulted in unaccounted losses.

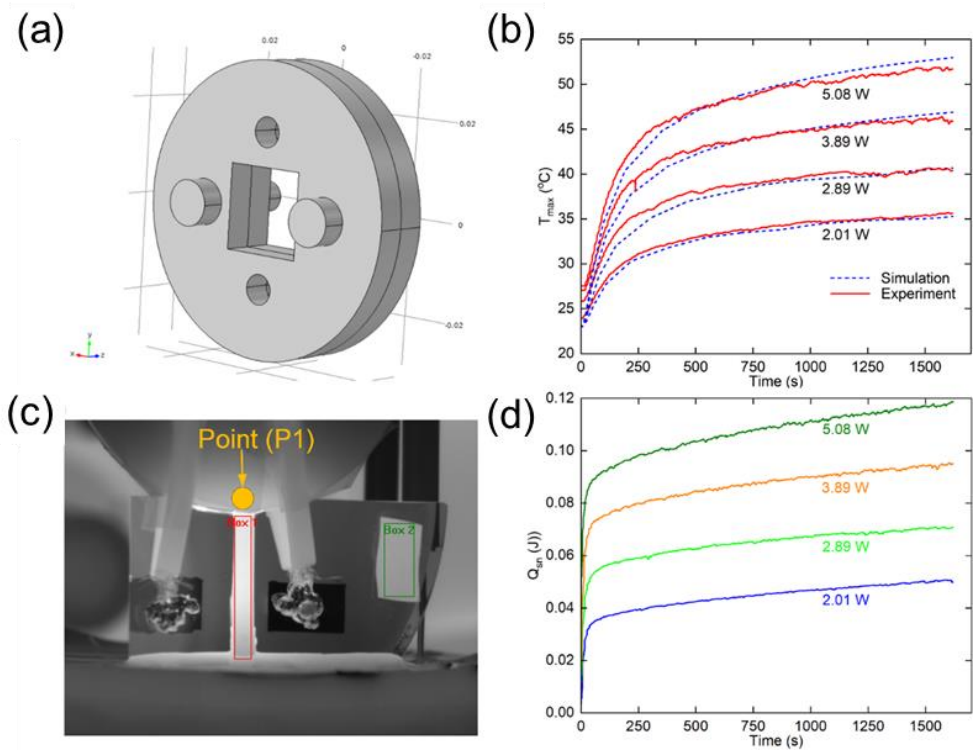

Figure 4.6. Heat loss estimation. (a) Three dimensional teflon block geometry used in simulation. (b) Comparison of experimental and simulation temperature of a point (P1) on teflon. (c) Infrared image at a random instant depicting point P1, box 1 and box 2 on vinyl tape. (d) Energy loss due to natural convection from sample[187]

Since latent heat of vaporization of water is temperature dependent[196] , we have used different values of h_{fg} corresponding to average temperature of sample during each experiment. As shown in Figure 4.7a, despite increase in vapor generation rate with increasing power input, the simultaneous decline in available pores for evaporation resulted in lower specific vapor generation and hence moderate vapor generation efficiency. The maximum specific vapor generation rate peaking at heat input of 2.89 W suggests that such system would have an optimum heat input where the vapor generation rate is balanced by water supply rate.

Nevertheless, low vapor generation efficiency (~20%) implies unignorable heat loss in current experimental design. Hence, we performed a quantitative analysis of heat losses in the system. Figure 4.7b shows the energy distribution for all four cases. The energy loss to bulk water was the major heat loss, primarily due to the lack of thermal insulation between the sample and bulk water, as well as relatively high thermal conductivity of silicon substrate. The energy assessment of all four cases can be found in Table 4.1.

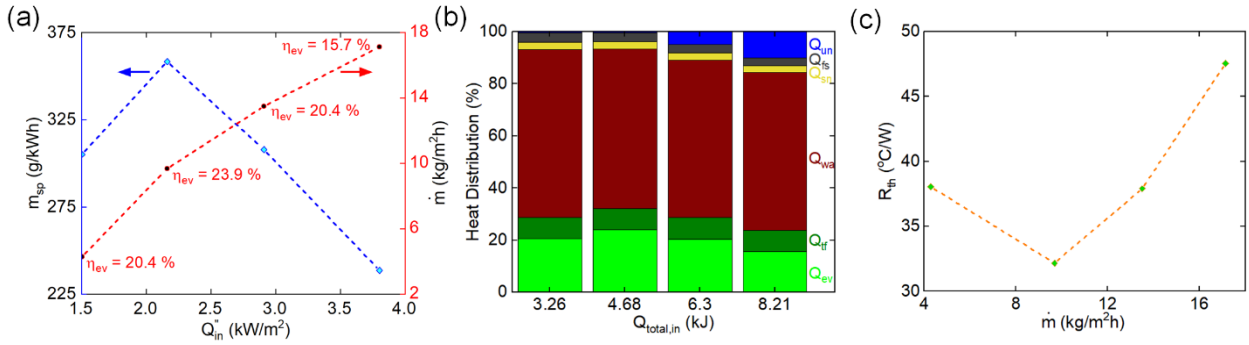

Figure 4.7. Performance of porous nanochannel wicks (a) Variation of specific vapor generation (on left y-axis) and vapor generation rate (on right y-axis) with supplied heat flux. (b) Distribution of total supplied energy among different factors such as evaporative energy (Q_{ev}), energy loss to bulk water (Q_{wa}), energy loss to teflon (Q_{tf}), natural loss from sample (Q_{sn}), energy loss due to free surface evaporation (Q_{fs}) and unaccounted losses (Q_{un}). (c) Thermal resistance behavior with vapor generation rate[187].

At last, we evaluated our design by calculating R_{th}

$$R_{th} = \frac{T_{max} - T_{amb}}{Q_{ev}} \qquad \text{Equation 4.8}$$

where T_{max} is the maximum temperature on sample, T_{amb} is ambient temperature assumed to be constant (23°C). As shown in Figure 4.7c, the minimum thermal resistance in current design was obtained in the case of heat input of 2.89 was 32.17 °CW^{-1}, which is similar to the reported

values in literature[75,191]. This implies that mitigation of losses, especially energy loss to bulk water would significantly lower the heat input while maintaining high evaporation rate for nanochannel wicks-based vapor generation systems. Heat loss to bulk water can be significantly reduced by incorporating suitable porous insulators such as recyclable foams[197] (porosity ≈ 90 % and thermal conductivity ~ 0.13 $W°C^{-1}m^{-1}$), porous ceramic[198] (porosity ~ 60 % and thermal conductivity 0.165 $W°C^{-1}m^{-1}$) and readily available highly porous polyurethane foams[199] (thermal conductivity 0.022 $W°C^{-1}m^{-1}$) underneath the current device in horizontal position.

Table 4.1. Energy assesement for 2.01 W, 2.89W, 3.89 W, 5.08 W and 1.25 Sun.

Quantity	**2.01 W**	**2.89 W**	**3.89 W**	**5.08 W**	**1.25 Sun**
Heat supplied (J)	3256	4682	6302	8230	1088
Heat lost in evaporation	666	1120	1283	1292	384
Heat loss to teflon blocks (Q_{tf})	267	385	524	657	92
Heat lost due to bulk water (Q_{wa})	2101	2868	3806	4997	548
Heat lost to surrounding from sample surfaces (Q_{sn})	93	132	176	211	11
Heat lost to surrounding due to free surface evaporation (Q_{fs})	119	158	199	240	42
Unaccounted heat loss (Q_{un})	10	19	314	833	11
Efficiency	20.4 %	25.3%	22.2 %	17.7 %	35.3
Unaccounted loss	0.3 %	0.4 %	6.27 %	10.1 %	1 %

4.3.3 Performance of nanochannel wicks under solar simulator

To assess the performance under solar heat flux, we have used solar simulator (1250 Wm^{-2}) with black enamel paint instead of vinyl tape having calibrated emissivity of 0.96 (Figure 4.8, inset). For this experiment, a smaller sample size of 14 mm by 14 mm (instead of 28 mm by 28 mm as in previous cases) was used keeping the nanochannel dimensions same. This allowed us to operate solar lamp, which has low output beam diameter (~33 mm), at the desired heat flux.

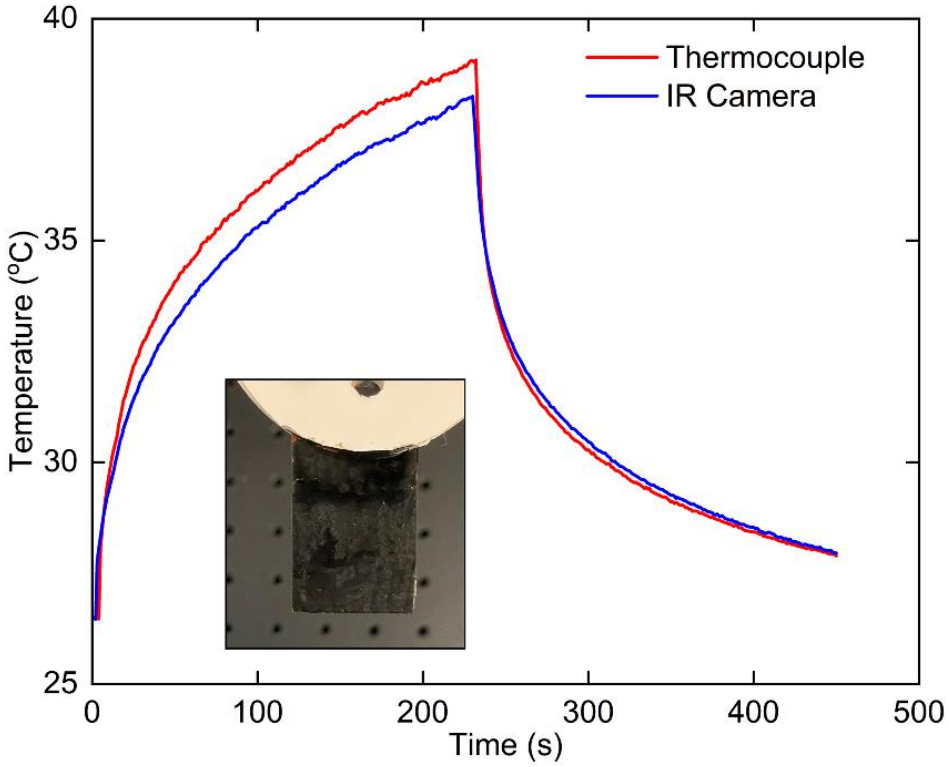

Figure 4.8. Comparison of temperature recorded by IR Camera (at a location on black paint coating) and thermocouple at constant emissivity (ϵ =0.96) of paint. Inset shows the coating of heater side of sample with black enamel paint[187].

Cumulative vapor generated mass and variation in wicking distance is shown in Figure 4.9. The average wicking distance and vapor generation rate was 5.12 mm and 4.87 $kgm^{-2}h^{-1}$, respectively.

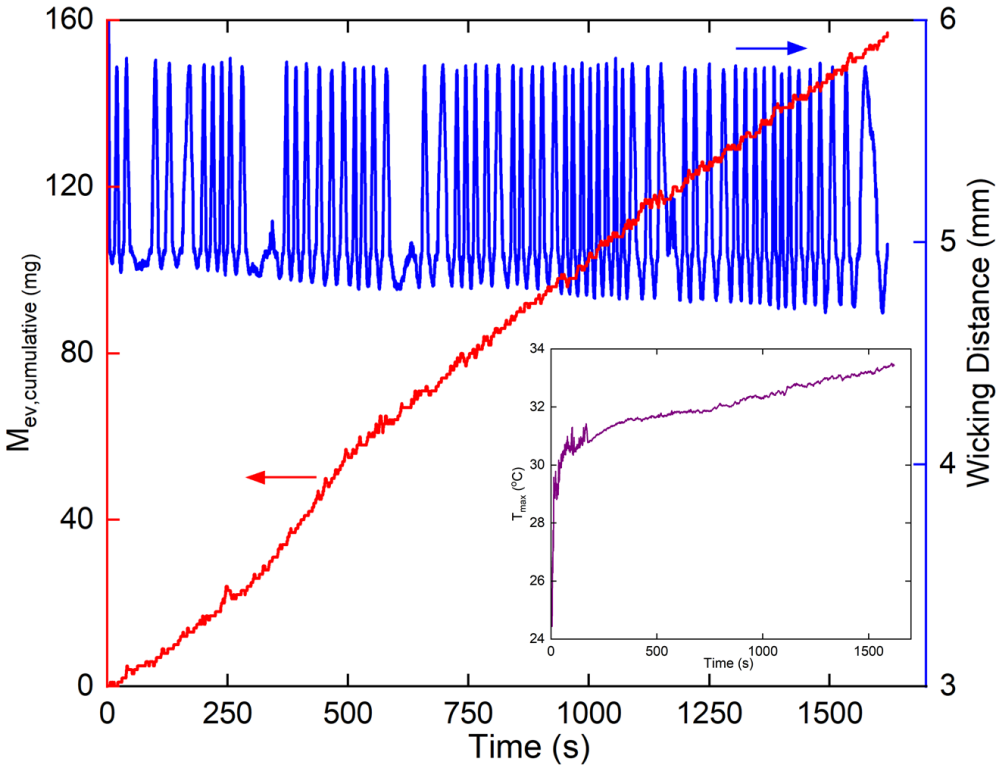

Figure 4.9. Variation of cumulative mass of generated vapor (left y-axis) and wicking distance (right y-axis) with time for 1.25 sun (1250 Wm^{-2}). Inset is a temporal plot of maximum sample temperature[187].

Vapor generation efficiency was 35.3%, which is significantly higher than the previous cases with joule heating. This could be attributed to the combined effect of factors like uniform distribution of heat by solar arc lamp on sample and low area of contact between sample and water (due to smaller sample size) causing less heat loss to bulk water. The maximum surface temperature was 33.5°C (shown in inset, Figure 4.9) with thermal resistance of vapor generation system as 44.3 $°CW^{-1}$.

4.4 Summary

In conclusion, a novel approach of vapor generation using micropore-nanochannels wick combination on a silicon substrate was presented. Enhanced evaporation observed in present

system is combination of the interfacial evaporation at pores and along the path of water travel. Apart from joule heating, we have shown that for such devices solar radiation absorption would depend on the emissivity of heating surface and hence it eliminates the need of additional absorber component. Unlike most carbon-based substrate, the design of current sample is well structured facilitating easy optimization of channel and pore dimension. We believe that present strategy to separate heating surface and vapor generating surface along with low operating temperature (even <50°C). could be beneficial in heat recovery from low grade energy sources besides solar radiation. We were able to obtain vapor generation rate of 1.18 $kgm^{-2}h^{-1}$ in dark condition (no heat input) up to 17.12 $kgm^{-2}h^{-1}$ at 5.08 W. Testing the current system using solar simulator under heat flux of 1.25 sun (1250 Wm^{-2}) resulted in vapor generation rate of 4.87 $kgm^{-2}h^{-1}$ which is significantly higher than reported values in literature at same heat flux. Moreover, the increasing power input diminished the wicking distance from 9.39 mm in dark condition to 2.61 mm at 5.08 W effecting the interfacial area available at pores for evaporation. Further, maximum vapor generation efficiency in such devices is governed by two crucial factors namely power supply and wicking distance. Although, they are interdependent factors, there exist an optimum value of heat input for which wicking distance is sufficient to prevent dry out and maintain continuous evaporation at pores.

Chapter 5: Nanochannel based Evaporator for Thermal Management

5.1 Introduction

Thin film evaporation has been shown to achieve tremendous heat flux dissipation for variety of fluids on micro-nano structured surfaces. Thermal management solutions of integrated circuits (ICs) used in electronic devices frequently use thin film evaporation[7,121,200], to maintain the temperature of such devices in the operational range. However, high heat flux values have typically been attained based on the distance between meniscus and the liquid reservoir ranging from tens to hundreds of micrometers. Such a short wicking distance can be vulnerable to quick drying out while also limiting the real-world applicability of such devices. Furthermore, , accuracy of heat flux[201,202] calculation with any fluid-wick structure combination directly depends on the reliability of contact angle (CA) measurement at the meniscus because it governs the pressure gradient required for capillary flow. The CA acquired from the meniscus image[109] or Young-Laplace equation[110] in the confined space may not be accurate because it is susceptible to errors in the detection of the three-phase contact line and the limitations associated with the camera/microscope field of view. Other studies have used augmented Young-Laplace model[201], interferometry[202] and, different contact angles for top and side walls of high-aspect-ratio wicks[203] to capture accurate apparent contact angle of fluid. To overcome this issue, we performed direct measurement of mass of evaporated FC72 to estimate the interfacial evaporative heat flux. Such a technique mitigated the need for contact angle measurement in micro/nano confined space. The device used in this study was a nanochannel (122 nm depth and 10 μm width) based evaporator with FC72 as working fluid. The evaporative performance relies heavily on maintaining the thin liquid film at the interface governed by capillary pressure and viscous pressure drop in wick/porous structure. Although a decrease in the

geometrical parameters of the wick design enhances capillarity, increased viscous resistance restricts fluid flow[10]. For a characteristic length of 'L' of a typical wick structure with wick distance 'D' between liquid source and evaporation zone, capillarity scales as L^{-1}, in contrast, hydrodynamic resistance scales as DL^{-2}. Therefore, momentum transport poses a significant challenge in evaporator design of a heat pipe. FC72 was chosen to be working fluid as it is non-polar and dielectric with a low boiling point suitable for electronics cooling. The 1 mm thick evaporator consists of more than 1000 nanochannels connecting two micro-reservoirs 4.8 cm apart. Thin film evaporation experiments were conducted for four different power inputs, and the steady-state wicking distance varied from 21 mm to 8 mm depending on the evaporator's working temperature. The maximum evaporative heat flux was 0.93 $kWcm^{-2}$ at ~ 65 ºC hot spot temperature. Interestingly, the product of wicking distance and evaporative heat flux remained constant for all power inputs. Numerical simulations were performed to quantify the heat losses from different components of the evaporator arrangement and to determine the effectiveness of the system. This study provides a systematic approach to design thin film evaporators while delineating important parameters to help develop effective thermal management strategies for high-performance electronics.

5.2 Methodology

Figure 5.1a shows the three-dimensional model of the nanochannel evaporator (nc-EVAP). FC72 enters the device through openings fabricated in glass right over the micro-reservoirs. Details for nc-EVAP fabrication methodology is discussed in Appendix A3. Depending on the experimental requirement, either single or both openings can be used to supply FC72. Heater is attached in the center and bottom of nc-EVAP along with a thermocouple (Appendix A3). Atomic force microscopy (during fabrication) on a channel cross section, and depth variation are shown in

Figure 5.1b, c, respectively. The average depth of a nanochannel is ~122 nm with width ~ 10 µm. Micro-reservoirs are of dimension 22 mm by 6 mm and length of nanochannels connecting them is ~ 48 mm. The top view of nc-EVAP used in experiments is shown in Figure 5.1d. Yellow tape pieces covering the openings keep the micro reservoirs clean until the tube reservoirs are attached (Appendix A3) before the experiments. Micrograph of a portion of nc-EVAP (Figure 5.1e) shows the alternating nanochannels (light shade) and silicon ridges (dark shade), each of width ~10 µm.

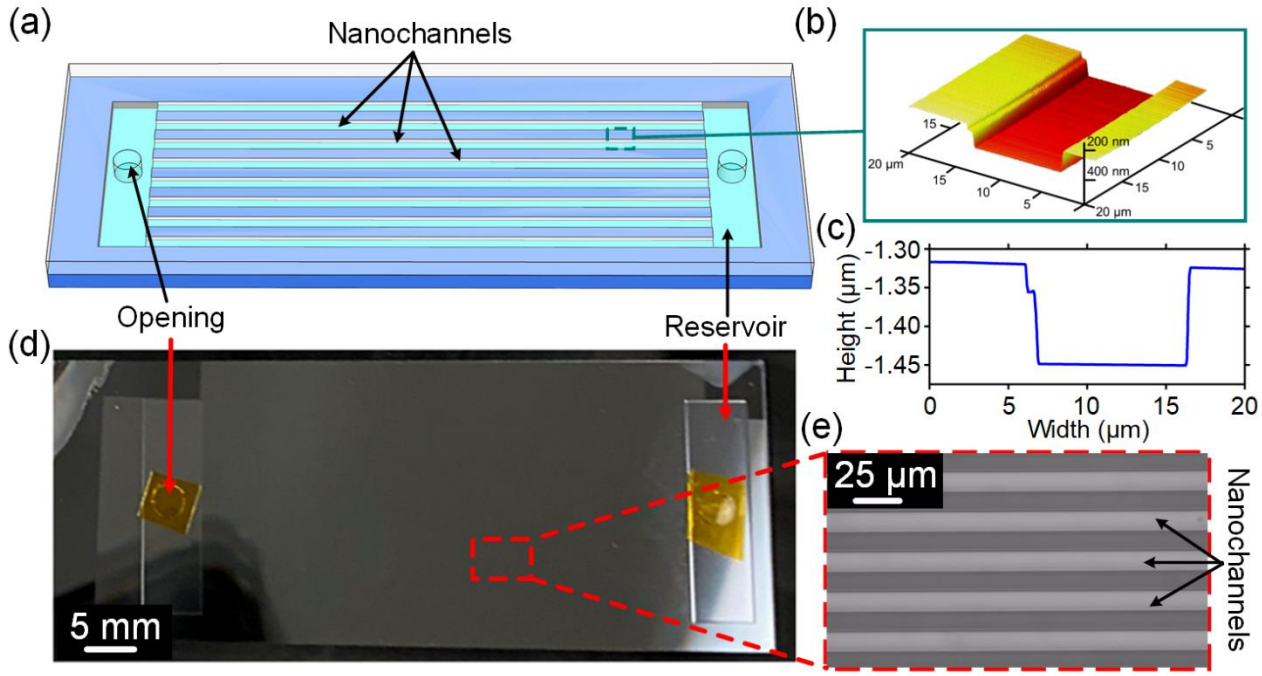

Figure 5.1. Evaporator details and nanochannel characterization. (a) 48 mm long nanochannels (122 nm by 10 µm) between two micro-reservoirs having openings over them are shown in a three-dimensional illustration of a nanochannel evaporator (nc-EVAP). (b) Atomic force microscope (AFM) image of a nanochannel. (c) Variation of the depth of the nanochannel across its width. d) Actual nc-EVAP used in experiments with its features. (e) Micrograph of nc-EVAP showing alternate nanochannels with silicon in between them.

Figure 5.2a shows the schematic of the experimental setup that has tube reservoirs with sealing plugs, heater, plastic support, and aluminum base plate attached to the nc-EVAP. The meniscus movement is tracked and visualized under the microscope (Figure 5.2b), and the location of the meniscus from the micro-reservoir (i.e., wicking distance) was determined using a reference scale placed beside the nc-EVAP. The left tube reservoir in Figure 5.2b is longer than the right one because it is primarily used to hold the FC-72 during nc-EVAP experiments, and the scale markings (least count: 0.01 ml) on its curved surface estimate the amount of FC72 evaporated during the experiments. At each input heat flux, nc-EVAP was first observed under a microscope, then temperature was monitored using an infrared (IR) camera (Figure 5.2c). Temperature distribution on the nc-EVAP was recorded for 120 seconds after achieving steady state (~ 20 minutes after heat flux supply). Figure 5.2d depicts successive images of FC72 wicking in the nanochannels, as shown by the shift in color and contrast during the process. FC72 gradually floods the nanochannels all the way to the other micro-reservoir. Details of the nc-EVAP fabrication procedure, materials used, characterization, and other procedural details are presented in Materials and Characterization section.

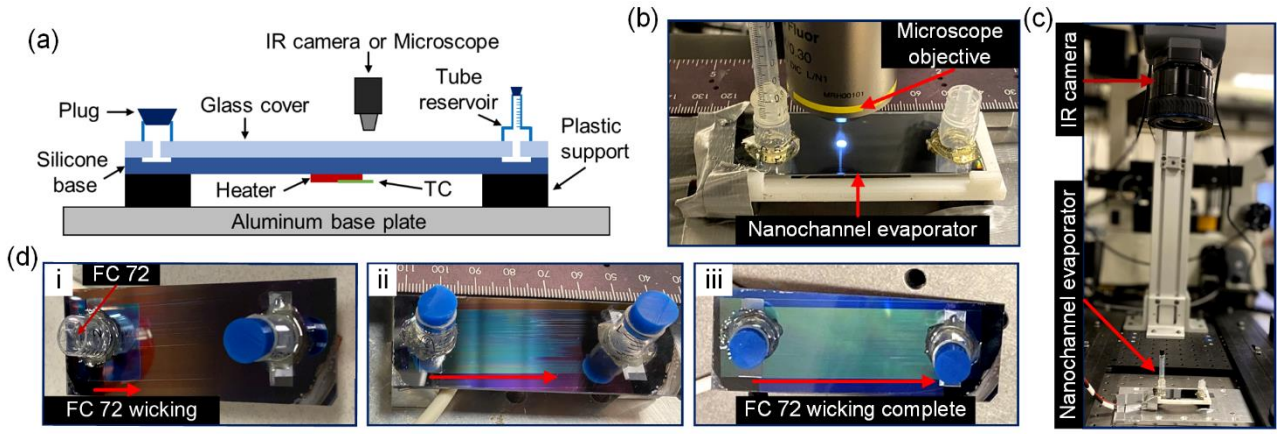

Figure 5.2. Experimental setup. (a) Schematic of evaporator arrangements including resistive heater at the bottom, over-the-top reservoirs, and plastic support between evaporator and base plate. (b) Observation of meniscus in nanochannels under the microscope. (c) Capturing temperature distribution across evaporator using infrared camera. d) Wicking of FC72 in nanochannels (i-iii) when one end of reservoir is filled while keeping another reservoir empty.

5.3 Results

5.3.1 Wicking Under no Supplied Power

The wicking of liquids in nanochannels is attributed to capillary pressure[204,205], and the motion of liquid inside is given by the Lucas–Washburn[206]

$$L_{wd} = K\, t^{0.5} \qquad \text{Equation 5.1}$$

where, L_{wd} is wicking distance, t is the elapsed time and K is a constant depending on the geometrical properties of the capillary tube and physical properties of the liquid. Linear variation of wicking distance with $t^{0.5}$ given in Equation 5.1 has been verified to hold valid for meniscus wicking inside nanochannels[203,207]. In present study FC72 is filled in from only one of the reservoirs of nc-EVAP keeping the other empty. A high-speed camera captures wicking video, which is later processed using MATLAB script to obtain continuous wicking distance (Figure

5.3a) confirming the linear relation between the wicking distance and $t^{0.5}$ proposed by Equation 5.1. Furthermore, liquid front velocity (V_{wf}) during the wicking process is shown in Figure 5.3b and is also obtained by image processing as discussed in the next section. The flow of liquid through nanochannels leads to occurrence of disjoining pressure[203] and development of ultra-thin stagnant layers on the solid surface[205]. V_{wf} drastically diminishes within ~ 250 sec of wicking (L_{wd}~ 19 mm) due to viscous resistance, and approaches ~15 μms^{-1} towards the end.

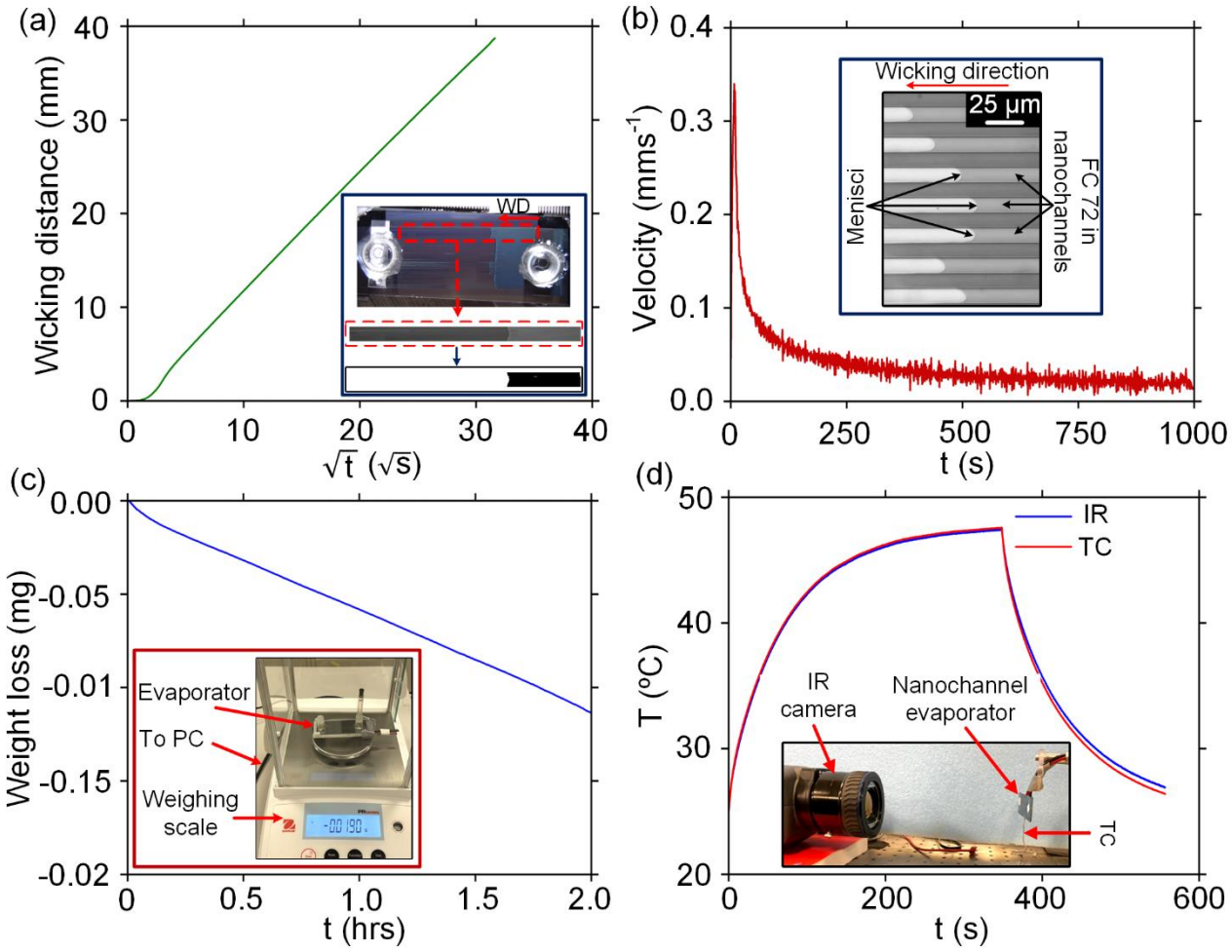

Figure 5.3. Wicking in of nc-EVAP. (a) Wicking distance of FC72 in nanochannels as a function of square root of time. The inset shows the actual liquid front and the corresponding procedure to obtain the wick length (b) Variation in the velocity of the liquid front with time. The inset

shows the menisci in nanochannels. (c) Calibration of weight loss obtained from decrease in FC72 level on the reservoir scale with weight loss recorded by the weighing scale. d) Emissivity calibration of the evaporator for emissivity = 0.92.

After complete wicking, the nc-EVAP was kept on a computer-connected weighing scale to record the weight loss due to evaporation of FC72 as shown in Figure 5.3c. The tube reservoirs are arranged so that the long tube (inset, Figure 5.3c) with scale marking containing FC72 is kept plugged (i.e., closed) to prevent evaporation, while the other tube reservoir is left open to the atmosphere. The recorded weight loss over a period of two hours was then calibrated against the drop in level of FC72 in the right reservoir (inset, Figure 5.3c). This weight change-based approach of finding evaporative mass flux and subsequent evaporative heat flux (for localized heating, next section) is rather unconventional and independent of contact angle-based methodology extensively used in literature. Deviating from macroscale to nanoscale, meniscus shape, and hence contact angle accuracy, depends on numerous factors such as resolution of image, refractive index of glass, molecular interaction between fluid-solid surface, and contaminations in confined spaces, and certainly edge detection of the microscopic image of liquid-vapor interface may not be an accurate technique of finding contact angle. Studies[201,208] show that there exist inherent issues in confinement, such as significant variation between the actual and apparent contact angle and potential deformation of microstructure at the three phase contact line under negative pressure. Although the current weight loss approach does not capture details of the interfacial phenomena, it does account for the macroscopic performance of nanochannels. Evaporative mass flux ($\ddot{m}_{ev}$) in absence of active heat flux was ~12.8 $kgm^{-2}s^{-1}$ obtained from following equation:

$$\ddot{m}_{ev} = \frac{\Delta m}{t_{ev} * A_{nc}}$$ Equation 5.2

where, Δm is mass change of FC72 in the tube reservoir (kg), t_{ev} is the total evaporation time (s) and A_{nc} is the total cross-sectional area of nanochannels (m^2). Please note that A_{nc} does not include nonfunctional/blocked nanochannels which were found to be 84 (out of total of 1100). Prior to evaluating the performance of nc-EVAP, emissivity (ε) calibration of evaporator top surface was performed as shown in Figure 5.3d. The temperature recorded by the IR camera and thermocouple matches well at $\varepsilon = 0.92$, and this value of ε has been used in this work.

5.3.2 Liquid Front Velocity

The liquid front velocity (V_{wf}) was measured by analyzing frames of the sliding drop; the frames were recorded using the high-speed camera. A custom written MATLAB algorithm was used to detect the wick front. After cropping out the desired area in the image, it is converted into binary i.e., black & white image (inset, Figure 5.3a). This enabled easy tracking of the wick front as the black pixel on the wick front would always have value "0" and vacant nanochannel ahead appearing as white pixel would have value "1".

Elapsed time elapsed (t) between frames was obtained from number of frames (nf) and captured frame rate (fps) of video. Velocity was obtained as,

$$\text{Velocity} = \frac{\Delta L * fps}{p * nf}$$ Equation 5.3

where, ΔL is difference in pixel distance of wick front from the microreservoir in subsequent frames, p is calibrated pixel length (i.e., how many pixels would be in 1 mm).

5.3.3 Heating and Meniscus Stability

Initially, both reservoirs were filled with FC72 and allowed sufficient time to completely wick into the nanochannels (like Figure 5.2d) with sufficient additional FC72 present in both

reservoirs. Subsequently, sample was heated beyond its normal boiling point (~ 56ºC) by supplying 5.53 W (11.8 Wcm^{-2}) while continuous monitoring the nanochannels under microscope. Interestingly, despite the surface of nc-EVAP at ~88 ºC (Figure 5.4a), no sign of nucleation was observed. On the contrary, vigorous boiling was seen at the opening of the micro-reservoirs. Nucleation does not occur in the nanochannel primarily due to combination of disjoining pressure and associated increase in energy required to increase pressure and displace liquid[203,209]. Instead, heat from the heater is conducted laterally along the silicon wafer causing the surface temperature at micro-reservoirs to rise above boiling point. Following the dry out at the reservoirs, the menisci receded rapidly (Figure 5.4a) from one of the reservoirs to the other.

To obtain stable menisci under heated conditions, FC72 was filled in only one of the reservoirs. Depending upon the supplied power, stable menisci were achieved (Figure 5.4b) regulated by FC72 evaporation rate and subsequent momentum transport governing the FC72 flow to liquid-vapor interface. Four levels of power input at heater: 0.64 W, 0.92 W, 1.63 W and 2.20 W (corresponding heat flux: 1.36 Wcm^{-2}, 1.96 Wcm^{-2}, 3.48 Wcm^{-2}, 4.69 Wcm^{-2}) were utilized in nc-EVAP performance analysis. The distance at which the menisci attain steady state is called wicking distance (L_{wd}) which is measured after confirming the meniscus stability under the microscope. Temperature recorded by IR camera for Q = 2.2 W near left reservoir (L), right reservoir (R), and above heater (C) is shown in Figure 5.4c. Temperature near right reservoir is lower than the left counterpart due to presence of FC72 in the right one.

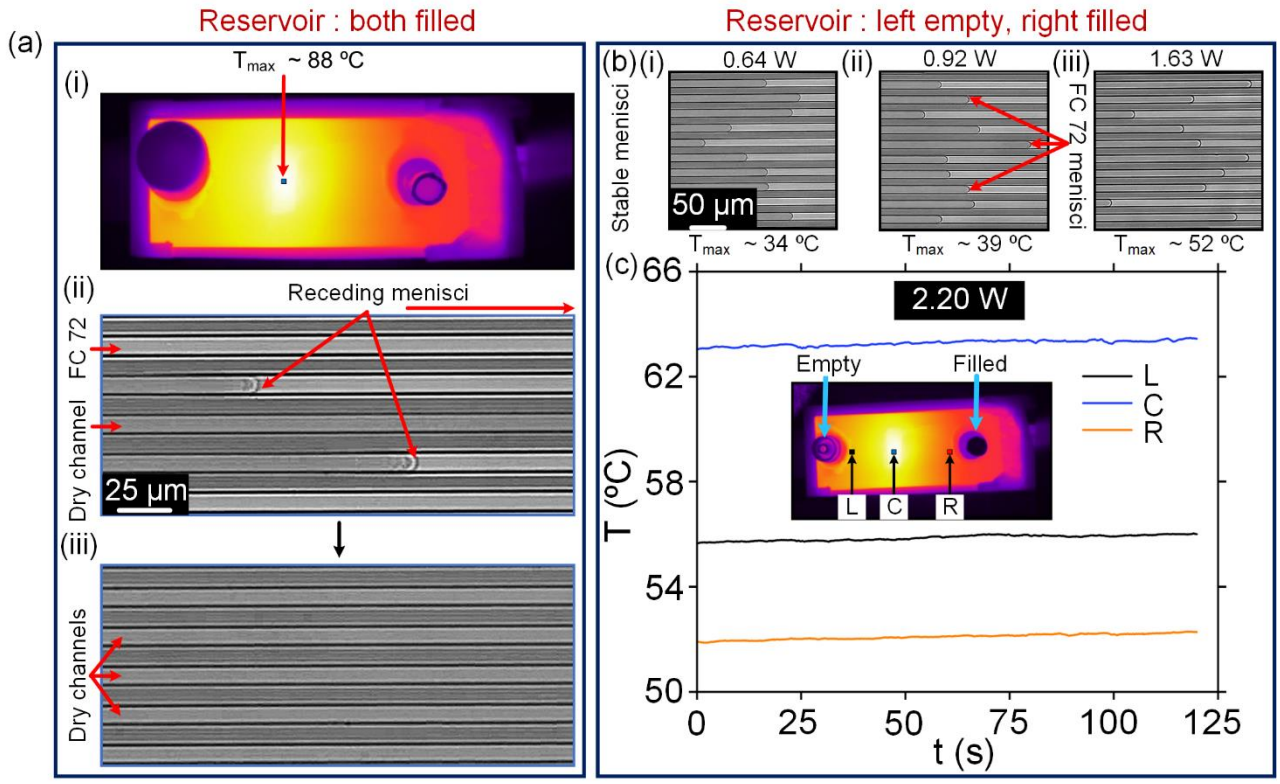

Figure 5.4. Observations in heated conditions. (a) Nanochannels dry out without nucleation, at temperature (~ 88 ºC) much higher than boiling point (~ 56 ºC) of FC72. (b) Stable menisci at different locations from reservoirs depending on the heat flux input. (c) Variation of temperature near left reservoir (L), right reservoir (R), and above heater (C) after achieving stable menisci.

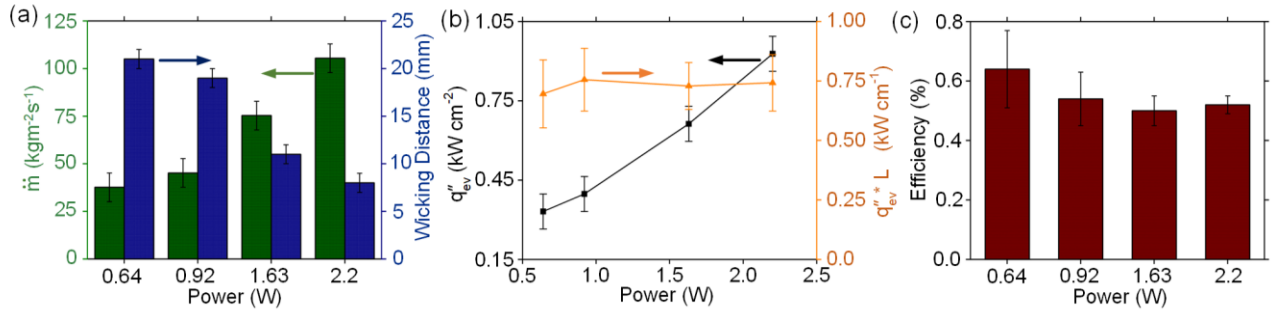

Figure 5.5. Nanochannel evaporator performance at different heat flux input a) Variation of evaporative mass flux (ṁ, left y-axis) and stable wicking distance measured from reservoir (right y-axis). b) Evaporative cooling efficiency. c) Variation of the interfacial evaporative heat flux

(left y-axis), and product of stable wicking distance with the interfacial evaporative heat flux (right y-axis)

$\ddot{m}_{ev}$ and L_{wd} for all four supplied power level are shown in Figure 5.5a. At 2.20 W, extremely high $\ddot{m}_{ev}$ ~105.4 $kgm^{-2}s^{-1}$ was recorded. Increased power supply caused reduction in L_{wd} from 21 mm (at 0.64 W), however nc-EVAP maintained L_{wd} = 8 mm (at 2.20 W) at temperature ~ 52 ºC (measured near meniscus) and close to the boiling point of FC72. At steady state, the contribution of interfacial evaporation in cooling (Q_{ev}) is given by:

$$Q_{ev} = \frac{\rho_l \Delta V h_{fg}}{t_{ss}} \quad \text{Equation 5.4}$$

where, ρ is the density of FC72 (1.68 gcm^{-3}), ΔV is the change in FC72 volume in the tube reservoir (ml), h_{fg} is the latent heat of vaporization of FC72 (88 Jg^{-1}), and t_{ss} is the experiment duration after achieving steady state. ΔV is acquired over t_{ss} = 30 minutes.

Steady state interfacial evaporative heat flux (q''_{ev}) for each supplied heat power is written as:

$$q''_{ev} = \frac{Q_{ev}}{A_{nc}} \quad \text{Equation 5.5}$$

Details on uncertainty analysis and numerical values are presented in Appendix A3, Table 5.1, respectively. For a moving meniscus, q''_{ev} is also given by:

$$q''_{ev} = \rho_l h_{fg} v_f \quad \text{Equation 5.6}$$

where, v_f is the liquid front velocity and for a flow thorough rectangular channel, it can be approximated as[109]

$$v_f \propto \frac{h^2 \Delta P}{\mu L_{wd}} \quad \text{Equation 5.7}$$

where, h is the height of the nanochannel, ΔP is the capillary driving pressure over L_{wd} and μ is dynamic viscosity of the liquid. The inverse relationship between v_f and L_{wd} can be observed from Figure 5.3a, b. From Equations 5.6 and 5.7 following observations can be made:

$$q''_{ev} L_{wd} \propto \frac{\rho_l h_{fg} h^2 \Delta P}{\mu}$$ Equation 5.8

Equation 5.8 implies that even though q''_{ev} increases with supplied heat input (Figure 5.5b), the product of interfacial evaporative heat flux and wicking distance remains uniform as verified with experimental results shown in Figure 5.5b. In current study, maximum q''_{ev} obtained was 0.93 kWcm^{-2} and average $q''_{ev} L_{wd}$ was ~ 0.73 ±0.02 kWcm^{-1}. So, a similar nc-EVAP designed to maintain shorter wicking distance L_{wd} ~ 100 μm can theoretically achieve q''_{ev} ~ 73 kWcm^{-2}, which is within the kinetic theory predictions[10] of maximum q''_{ev} ~ 110 kWcm^{-2}**.** The efficiency of nc-EVAP (Figure 5.5c) is written as:

$$\eta_{ev} = \frac{Q_{ev}}{Q}$$ Equation 5.9

where Q is supplied power to nc-EVAP. While local interfacial evaporative heat flux (q''_{ev}) can attain ~1 kWcm^{-2} or higher as in reported studies, its efficiency in actual device cooling is typically restricted or not reported. In current study, η_{ev} for all four level of supplied power was < 1 % due to the high q''_{ev} restricted only to minuscule interfacial area inside nanochannels. This aspect of nanostructured-based evaporator should also be investigated to enhance η_{ev} apart from primary focus on achieving higher q''_{ev}.

Table 5.1. Errors and uncertainties related to various parameters.

Parameter (unit)	**Mean Value**	**Standard Deviation/ Uncertainty**
0.64 W		
$\ddot{m}_{ev}$ (kgm^{-2}s^{-1})	37.6	7.5
Q_{ev} (mW)	4.11	0.82
q''_{ev} (kWcm^{-2})	0.33	0.06
$q''_{ev} L_{wd}$ (kWcm^{-1})	0.70	0.14

η_{ev} (%)	0.64	0.13
0.64 W		
$\ddot{m}_{ev}$ ($kgm^{-2}s^{-1}$)	45.2	7.5
Q_{ev} (mW)	4.93	0.82
q''_{ev} ($kWcm^{-2}$)	0.39	0.06
$q''_{ev}L_{wd}$ ($kWcm^{-1}$)	0.76	0.13
η_{ev} (%)	0.54	0.09
	1.63 W	
$\ddot{m}_{ev}$ ($kgm^{-2}s^{-1}$)	75.3	7.5
Q_{ev} (mW)	8.21	0.82
q''_{ev} ($kWcm^{-2}$)	0.66	0.06
$q''_{ev}L_{wd}$ ($kWcm^{-1}$)	0.73	0.09
η_{ev} (%)	0.50	0.05
	2.20 W	
$\ddot{m}_{ev}$ ($kgm^{-2}s^{-1}$)	105.4	7.5
Q_{ev} (mW)	1.15	0.82
q''_{ev} ($kWcm^{-2}$)	0.93	0.06
$q''_{ev}L_{wd}$ ($kWcm^{-1}$)	0.74	0.12
η_{ev} (%)	0.52	0.04

5.3.4 Heat Loss Estimation

While evaporative heat flux contributed < 1% to the thermal management, other factors such as conduction through silicon and subsequent heat loss via natural convection significantly reduced hotspot temperature. We performed COMSOL simulation to examine the hot spot temperature and associated convection heat losses in presence of nc-EVAP by comparing experimental and simulation temperature values.

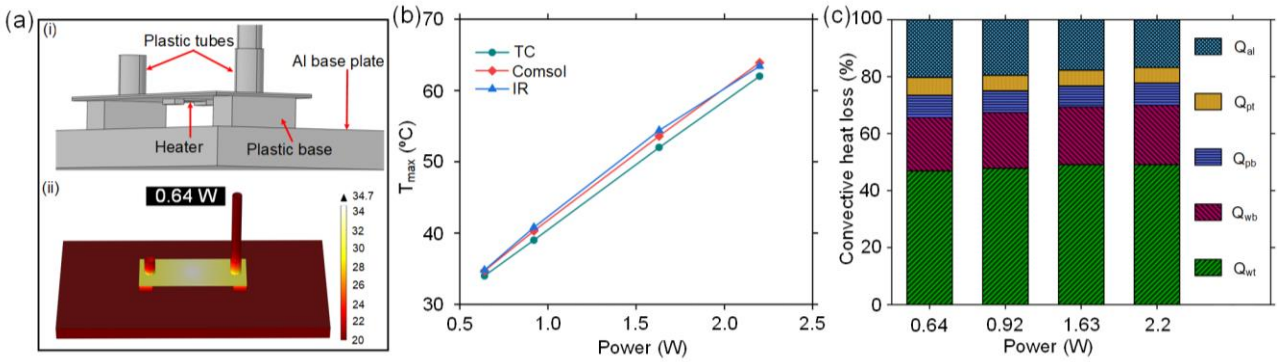

Figure 5.6. Heat loss estimation from COMSOL. (a) Three-dimensional model of evaporator arrangements and temperature variation across multiple sources of heat loss for 0.64 W. (b) Comparison of maximum temperature recorded by infrared camera (IR) and thermocouple (TC) over heater with temperature obtained from COMSOL simulation. (c) Distribution of natural convection heat loss from aluminum base plate (Q_{al}), reservoir tubes (Q_{pt}), plastic base under evaporator (Q_{pb}), evaporator bottom (Q_{wb}), and evaporator top (Q_{wt}).

Three-dimensional model and temperature distribution (for Q_{in} = 0.64 W) on the experimental setup obtained using COMSOL simulation is shown in Figure 5.6a.

All COMSOL simulations were steady state study. Boundary conditions in simulations were: ambient temperature = 20ºC, ambient pressure = 1 atm. To determine natural convection heat loss from different surfaces, inbuilt surface intergal function for heat flux was used. This method allowed us to obtain individual heat loss from different components of the experimental setup.

Dimesions of the components are as following:

Silicon and glass wafer: 80 mm by 30 mm by 500 µm

Heater: 7.1 mm by 6.6 mm by 500 µm

Electrodes: 6.6 mm by 3 mm by 1.5 mm

Plastic support base at both end of the evaporator: 20 mm by 10 mm by 10 mm

Aluminum base plate: 200 mm by 100 mm by 100 mm

Small hollow tube reservoir : outer radius 4 mm, 1 mm thick and 12 mm high cylinder over microreservoir

Long hollow tube reservoir : outer radius 3.5 mm 0.5 mm thick and 60 mm high cylinder over microreservoir

Comparison of maximum surface temperature obtained from simulation results and experiments (both by IR and thermocouple) for each of the supplied power is shown in Figure 5.6b. There is an excellent agreement between IR measurements and the COMSOL results, and corresponding percentage of the natural convection heat loss from various sources is shown in Figure 5.6c. The convection losses were from aluminum base plate (Q_{al}), reservoir tubes (Q_{pt}), plastic base under evaporator (Q_{pb}), bottom silicon surface of the evaporator (Q_{wb}), and top glass surface of the evaporator (Q_{wt}) which were estimated by performing COMSOL simulations. As expected, heat loss from the top surface of nc-EVAP (Q_{wt}) contributes the most in each case. Even though the maximum q_{ev} was ~ 0.93 $kWcm^{-2}$ for Q_{in} = 2.2 W, net cooling provided only by evaporation was ~ 11.5 mW and cooling was predominantly accomplished by heat losses via natural convection on the experimental setup. Similarly, previous studies[109,110,115,200] that demonstrate very high q_{ev} utilizing various types of porous structures, nano porous membranes, porous wicks among others, to enhance evaporative heat flux require a new perspective to assess the net effect of such q_{ev} improvements on device cooling and associated heat losses through other components.

5.4 Summary

A systematic approach of fabricating a practical nanochannel-based evaporator (nc-EVAP) was presented and its performance was evaluated with dielectric FC72 as working fluid. The nc-

EVAP device included 1100 nanochannels of cross-sectional area 122 nm × 10 μm running across a length of ~48 mm between two micro-reservoirs. nc-EVAP was designed to facilitate the direct measurement of the change in mass during evaporation of FC72, and thus the interfacial evaporative heat flux (q''_{ev}) was estimated without contact angle measurement of meniscus in nanochannels and the associated uncertainties that accompany such an approach. When the channels and both reservoirs were filled with FC72, nucleation was not observed even at temperature of ~88 ºC, well beyond the boiling point of FC72. When the channels were filled with FC72 using only one reservoir while the other reservoir was open to atmosphere, stable evaporating menisci were obtained for different power inputs. At lower input heat flux, maximum steady state q''_{ev} ~ 0.93 kWcm^{-2} was achieved at maximum surface temperature of ~ 63 ºC. The maximum variation of temperature in the nc-EVAP was ~ 11ºC from central hot spot to the micro-reservoir at 2.20 W. Depending on the given heat flux, the wicking distance ranged from 21 mm to 8 mm. The product of the steady q''_{ev} and the wicking distance was found to be nearly constant for all power inputs. This suggests the possibility of achieving high q''_{ev} by tailoring wicking distance even under steady state as compared to superior heat transfer performance during transient meniscus variation as reported in the literature. Another aspect of such evaporator is the evaporative efficiency, i.e., the absolute contribution of thermal management solution to the cooling of hot spot, which is found to be restricted to < 1% due to limited meniscus area in nanochannels. Numerical simulations were performed to calculate the contribution of different components of heat losses in the nc-EVAP system.

Chapter 6: Conclusion and Future Work

6.1 Conclusion

Nanochannel wicks for efficient heat transfer *via* tailoring surface wettability, and for thermal management of hot spot cooling was studied. Two different types of nanochannel wicks were fabricated; in first type the sample had cross connected nanochannels (height ~ 728 nm) with micro pores (diameter ~ 2 μm) at the junction while the second type was designed to have covered nanochannels (height ~ 122 nm) opening to two microreservoirs at each end 48 mm apart. While the applications and nature of the studies carried out on these sample differ, the underlying mechanism of capillarity governing the functionality of the samples remains common.

It was found that the inherent hydrophilic nature of the nanochannels with micro pores can be tailored into hydrophobic through a dedicated procedure involving plasma cleaning and silicon oil infusion-depletion. The Surface obtained is called nanochannel liquid infused surface (nc-LIS) which was shown to demonstrate remarkable durability in its hydrophobic characteristics resulting in improved condensation heat transfer performance in presence of non-condensable gases. It was discovered that while the higher silicone oil viscosity nc-LIS exhibited longer surface retention, the drop sliding velocity was significantly lower on freshly prepared LIS. Moreover, the condensation on nc-LIS using 50 cSt silicon oil provides substantial improvement in condensation heat transfer coefficient (HTC ~ 2.33 $kWm^{-2}K^{-1}$) by 162% over flat silicon LIS even in oil depleted state. Improved performance can be attributed to oil being held inside nanochannels, and thus retained on the surface, due to capillarity and improved adhesion owing to plasma cleaning. Drop size distribution study reveals more than ~ 95 % of all drops had a diameter < 500 μm suggesting fast shedding of the condensates. To confirm the durability of the

nc-LIS, condensation was carried out for 3 days. Steady-state HTC was achieved with an average value: $1.46 \pm 0.16\ Wm^{-2}K^{-1}$. The sample maintained dropwise condensation throughout the experiment and never transitioned to filmwise condensation with WCA ~ 104º at the end of condensation.

Although the usage of the LIS surface mentioned above was more suitable for dropwise condensation, the nanochannel can also be transformed into a superhydrophobic surface (SHS) by a process involving plasma cleaning, silicon oil infusion, baking, oil depletion, and candle soot coating. Surface roughness because of soot coating helps to maintain stable Cassie-Baxter state with water contact angle (WCA) of nearly 160° and roll off angle (ROA) ~ 1°. The surface exhibited exceptional durability by retaining WCA of 154° even after 30 days of continuous submersion under 10 cm of water followed by 150 days in ambient air. Coating stability was successfully tested under impact of tap water jet having velocity of 1 ms^{-1} to 10 ms^{-1}, and 14.75 hours of continuous frosting-defrosting cycles with no effect on its wettability. Dropwise condensation on the surface was also observed to enhance with HTC of 2.7 $kWm^{-2}K^{-1}$. The SHS was found to be compatible with multiple organic materials milk, honey, soy sauce and chocolate syrup while its self-cleaning property was evident from complete removal of fine grain all-purpose flour from sample surface. Another feature of the prepared surface is superoleophilicity, potentially suitable for oil-water separation systems. Moreover, it was shown that the underlying porous nanochannel geometry allowed us to regenerate superhydrophobicity from a deteriorated state multiple time.

The inherent hydrophilicity of the first type of nanochannel sample was found to be suitable for vapor generation *via* thin-film evaporation at the pores. Enhanced evaporation is observed in the system due to the presence of multiple pores along the path of water travel. Testing the current

system using a solar simulator under heat flux of 1.25 sun resulted in vapor generation rate of 4.87 kg $m^{-2}h^{-1}$ which is significantly higher than reported values. As the surface temperature was < 35ºC, even low-grade heat sources can be used to obtain significant vapor generation rate. Moreover, vapor generation rate of 1.18 kg $m^{-2}h^{-1}$ was reported in dark condition (no heat input), and up to 17.12 kg $m^{-2}h^{-1}$ at 5.08 W of resistive heating. Heat losses associated with the system was quantified by performing COMSOL simulations. Maximum vapor generation efficiency in such devices is governed by two factors namely power supply and wicking distance. Although, they are interdependent factors, there exist an optimum value of heat input for which wicking distance is sufficient to prevent dry out and maintain continuous evaporation at pores.

Second type of the nanochannels wicks with microreservoirs combination was used as device level evaporator for hot spot cooling. Dielectric FC72 was chosen as the working fluid, and a novel approach to analyze performance was developed. This approach involved collecting continuous mass loss due to evaporation in nanochannel to obtain the mass flux rate and interfacial evaporation heat flux. It eliminated the need for the time-consuming and error-prone procedure of measuring contact angles in nanochannels. Even at 88ºC, well above FC72's boiling point, nucleation was not observed when the channels were completely filled with FC72. Partial filled channels, on the other hand, resulted in a steady state wicking distance ranging from 21 mm to 8 mm depending on the heat flux. At lower input heat flux, maximum steady state heat flux ~ 0.93 $kWcm^{-2}$ was achieved at surface temperature of ~ 63 ºC. The product of the steady evaporative heat flux and the wicking distance was found to be nearly constant for all power inputs suggesting possibility of achieving high heat flux by tailoring wicking distance even under steady state. Numerical simulations were performed to calculate the heat losses through different components. While such evaporators have traditionally been focused on achieving high heat flux,

the efficiency of such a system remains poor due to the low ratio of the interfacial area to the total hotspot area.

6.2 Future Work

Micro/nano porous surfaces have immense potential in thermal management and energy efficiency. Such surfaces can offer multifunctionality depending on the design and fabrication procedure as demonstrated in previous chapters. However, existing systems can be improved to address shortcomings based on the desired application.

For example, LIS on nanochannels wicks provides high heat transfer coefficient for 3 days of condensation but the size of sample in current study was relatively small (28.1 mm by 35.8 mm). The sample maintained dropwise condensation, never transitioned to filmwise condensation, and remained hydrophobic with WCA ~ 104º at the end of condensation. In future, current LIS preparation approach can be implemented on large scale porous surfaces which are easier to fabricate such as inverse opal, and chemically etched surfaces.

The superhydrophobicity obtained with candle coating shows potential for oil-water separation as implied by preliminary testing with canola oil-water emulsion. This concept behind soot coated porous structures can be replicated on large scale porous surfaces such as porous metallic mesh structures. Silicon oils are inert and nontoxic combined with readily available candle soot coating, which can be instrumental in fabrication of multifunctional, robust, scalable, and reproducible superhydrophobic surfaces. Other coatings such as fume silica, which resemble soot in wettability characteristics can be tested with adhesive-treated rough surfaces to evaluate the binding strength and the durability.

In vapor generation system with porous nanochannels, the high heat load performance was found to be dictated by the number of active pores for evaporation. In future studies, the fabrication of microchannels underneath the sample at the nanochannel-water interface could increase the feed of water into the nanochannels and thus achieve larger wicking distance and hence higher active pores for evaporation. Further, a suitable insulator, such as carbon foam, sponges, is needed at the bottom of the sample to minimize the heat loss to bulk water, which would enhance the vapor generation efficiency.

In Chapter 5, a discussion on nanochannel-based evaporator as chip cooling solution was reported. The evaporative efficiency of such an evaporator was one of the important aspects that came to light. It refers to the absolute contribution of thermal management solution to the cooling of hot spot, which is found to be restricted to < 1% due to limited meniscus area in nanochannels. As a result, in future, appropriate modifications in nanochannel design, including a three-dimensional approach in device fabrication, are required to improve the interfacial area, which could have significant impact on thermal management in electronic systems. Fundamental approach would be to increase the interfacial area as much as possible along with enhancing the transport of working fluid to the active evaporation site.

Thus, we see that although the underlying micro/nano structure can often be similar, with a little alteration and the proper methodology, they can be used in a range of applications. The design of the current systems can be improved in the future with regard to specific applications.

Appendix A1

A1-1 Fabrication of Porous Nanochannel Wicks

Fabrication schematic is shown in Figure A1. Fabrication of porous nanochannel (nc) wicks starts with a 500 μm silicon wafer. Firstly, mark fabrication on the wafer is carried out by photoresist coating, exposing in GCA stepper with suitable reticle followed by baking, developing, and etching. After removing photoresist, a mark on wafer leaves behind which is helpful in alignment during exposure in later stages. Then, Photoresist (thickness ~ 9 μm) was spin coated on the wafer and then exposed using GCA stepper followed by an ammonia diffusion bake for the image reversal. After photoresist development, 15 nm thick chromium (Cr) film obtained deposited by e-beam evaporator (deposition rate 1.1 - 1.3 A/s) was used as adhesion layer on top of which 713 nm thick copper (Cu) film (deposition rate 3.0 - 3.5 A/s) was further deposited (using e-beam evaporator). Then, the photoresist was removed, leaving behind Cr and Cu on silicon wafer then immersed in acetone for 6 hours. This lift-off process created orthogonally connected ridges of sacrificial Cr & Cu. Then, 300 nm thick SiO_2 film was deposited over patterned Cr & Cu layer by plasma enhanced chemical vapor deposition (PECVD). After depositing 300 nm thick SiO_2, SPR 220-3 photo resist was used to obtain a ~ 3 μm coating on the wafer. After baking, GCA stepper was used to expose the sample using custom made reticle (~ 2 μm diameter holes at 10 μm pitch, exposure time 0.5 s) and executing required job file. It is important to note that alignment of reticle is very important while executing exposure such holes are exposed at the intersection of the ridges. After hard bake and development wafer with exposed SiO_2 (at ~ 2 μm diameter holes) undergoes dry etching followed by photoresist removal in hot bath and plasma strip resist. The wafer was immersed in Cr & Cu etchant to remove sacrificial Cr & Cu to form the nanochannels which are

interconnected orthogonally and open to environment via pores (~ 2 µm holes). Wafer is cut in to required dimension of sample using dicing saw.

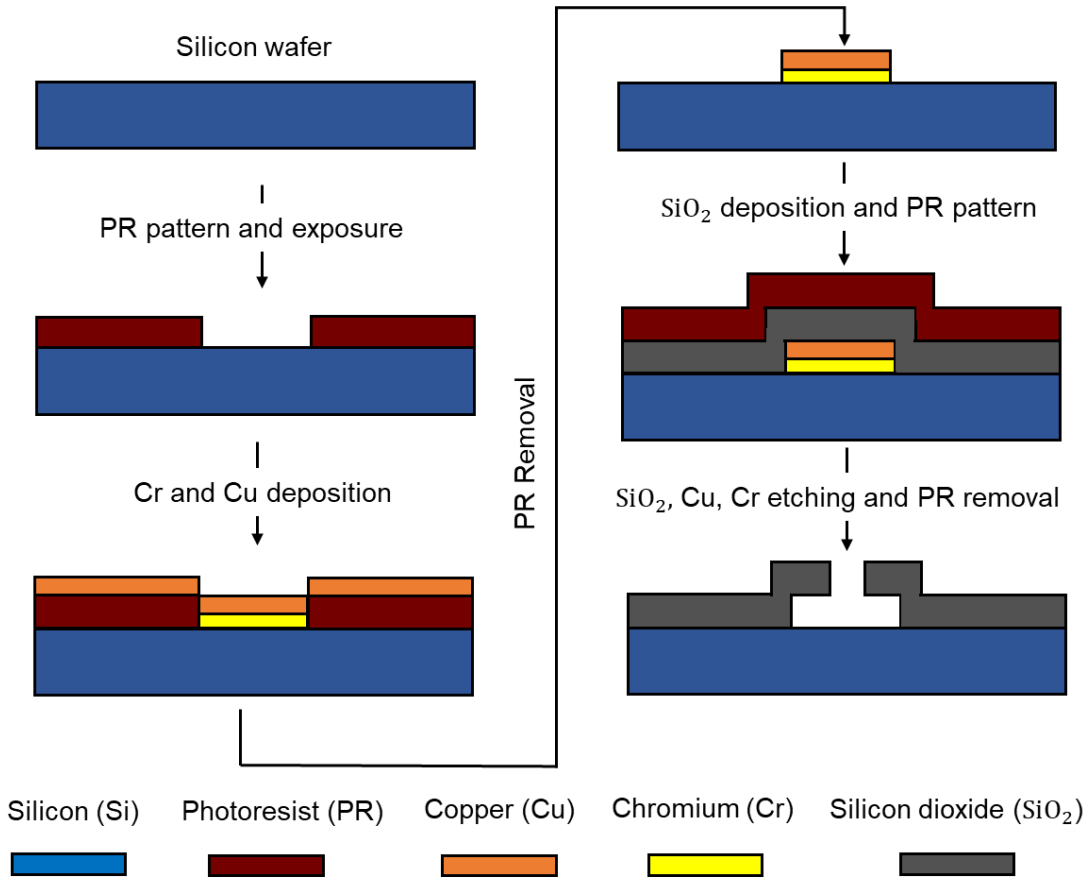

Figure A1. Porous nanochannel wick fabrication procedure.

A1-2 FT-IR Spectrum of Depleted Nanochannel LIS Sample

In the FT-IR spectrum of nc-dep LIS (Figure A2), the absorption peaks located at 2962 cm^{-1} and 2904 cm^{-1} are due to the asymmetric and symmetric stretching vibration of C-H in methyl and methylene groups present in silicone oil, respectively [210] and the peaks appeared at 1413 cm^{-1} and 666 cm^{-1} can be attributed to the bending vibration of C-H bonds [211] due to the remaining non-reacted precursors or the presence of adsorbed fats or contaminants on the surface of the material. The peaks centered at 1259 cm^{-1}, 1085 cm^{-1}, and 1016 cm^{-1} can be related to the

stretching vibration of Si-OH [212] and asymmetric and symmetric stretching vibration of Si-O-Si, respectively [213,214]. The absorption peak centered at 794 cm^{-1} is due to the bending vibration of the Si-O-Si bonds [215].

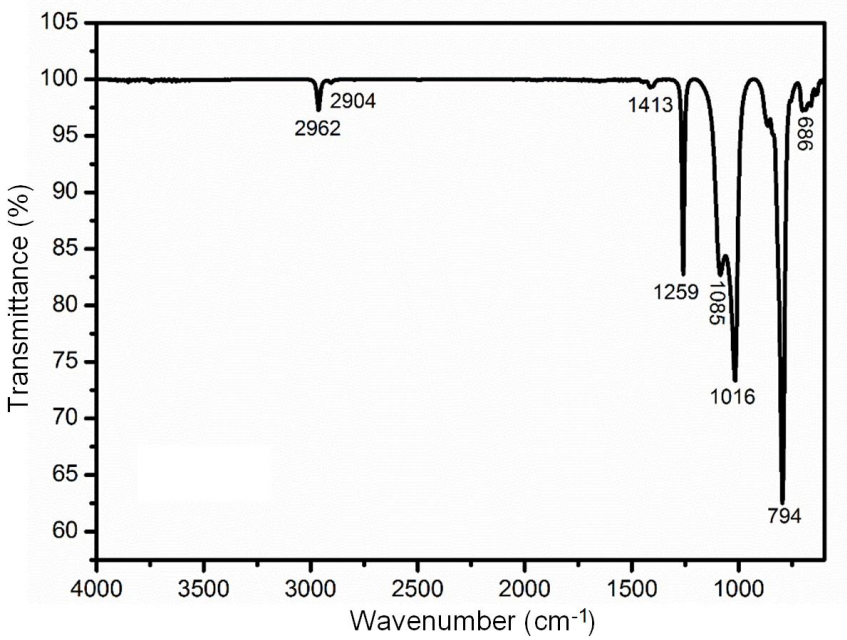

Figure A2. Fourie- transform infrared spectroscopy (FTIR) of water jet shear induced depleted nc-LIS.

A1-3 Actual Experimental Setup for Condensation

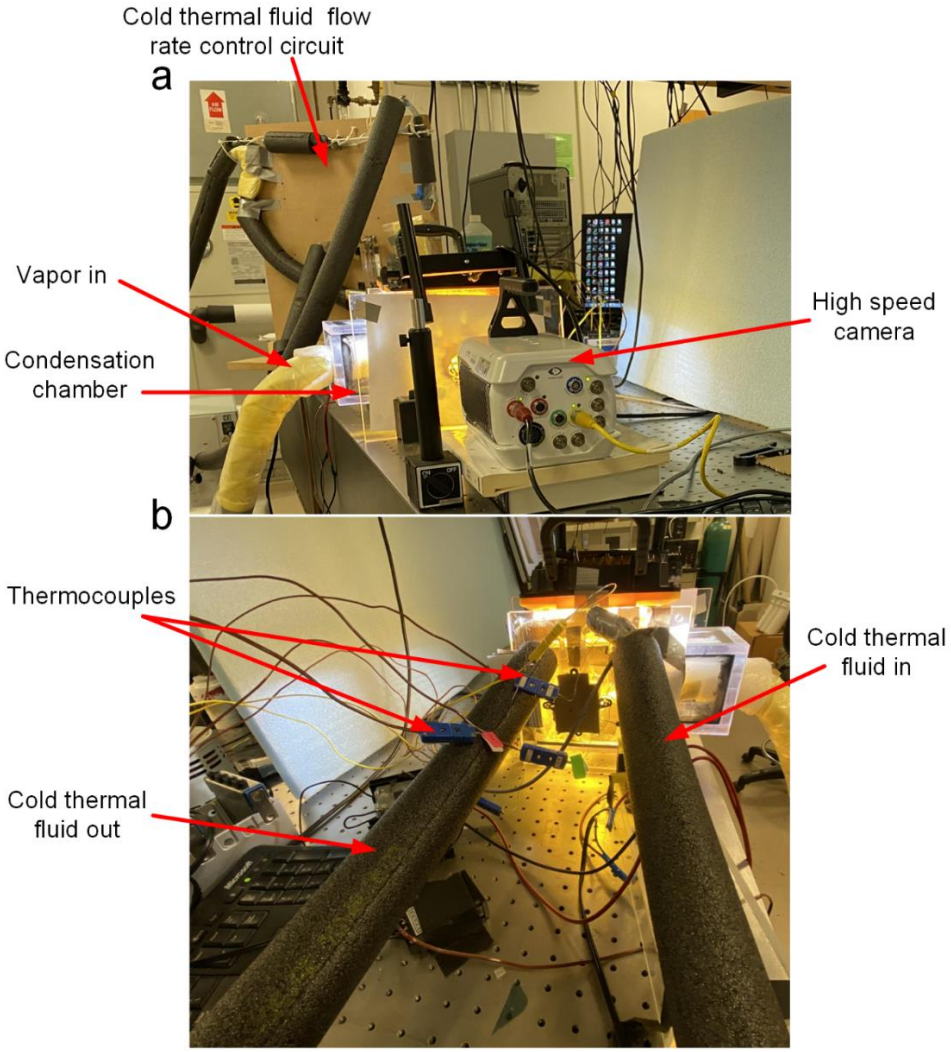

Figure A3. Condensation experimental setup. (a) components of the setup, with cold thermal fluid circuit board having height of 2 ft, and (b) view from the fluid flow rate control circuit board towards condensation chamber.

A1-4 Drop Sliding Velocity Analysis

The velocity measurement was performed by analyzing the drop sliding frames recorded by the high-speed camera. To visualize the drop, a solution of sodium fluorescein was prepared (0.1 gm

in 1 liter of deionized water)[216] and a custom written MATLAB algorithm was used to track the motion of water drop as shown in Figure A4. The images obtained from the high-speed camera were counter rotated by same angle as that of inclination of sample to make the drop motion appear horizontal during image processing. Then, after cropping out the required area in the image, it is converted into binary i.e., black & white image. This enabled easy tracking of the contour front of the drop as the white pixels on the drop would always have value 1. In Figure A4, P1 (point on drop front at the beginning of drop sliding) and P2 (point on drop front after time "t" of drop sliding) shows the location of front being tracked. The difference between pixel location along with calibrated pixel length (i.e., number of pixels in 1 mm denoted as "p") would give the distance travelled by the drop. Elapsed time (t) between frames was obtained from number of frames (nf) and captured frame rate (fps) of video. Velocity was obtained as,

$$\text{Velocity} = \frac{(P_1 - P_2) * \text{fps}}{p * nf} \qquad \text{Equation 6.11}$$

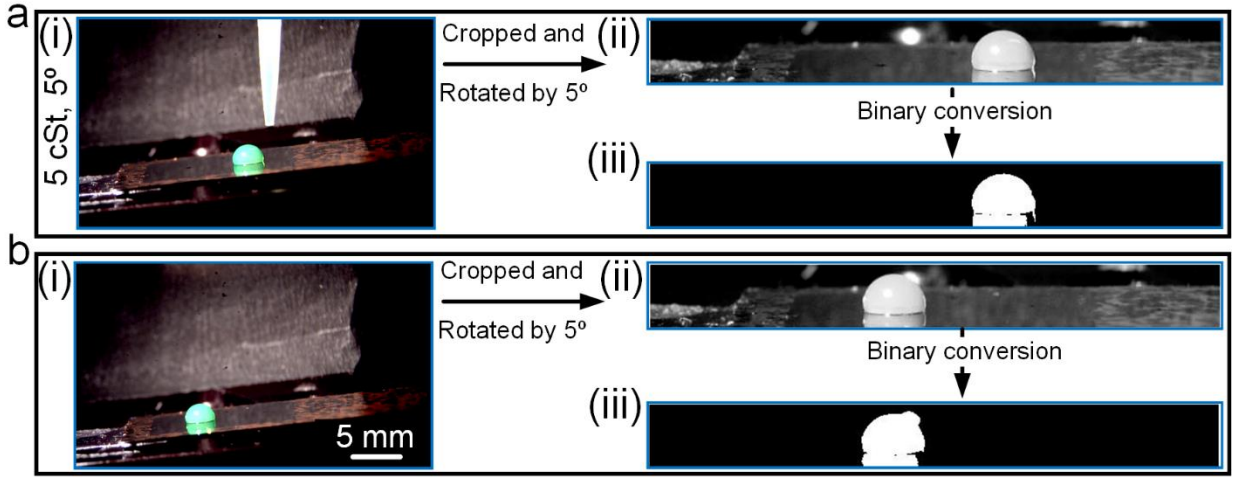

Figure A4. Drop sliding velocity measurement procedure. (a) (i)Initial drop position at the start of sliding, (ii) rotation of image by an angle same as that of sample inclination angle followed by cropping and grey scale conversion, (iii) binary (black and white) conversion (b) (i) final drop

position after sliding for some time "t" (ii) rotation of image by an angle same as that of sample inclination angle followed by cropping and grey scale conversion, (iii) binary (black and white) conversion

A1-5 Errors and Uncertainties Calculation

Uncertainty related with temperature and humidity was taken as the standard deviation in data recorded during the condensation experiment. Condensation heat transfer coefficient (HTC) was calculated at each data point in temporal domain and related standard deviation in HTC is due to fluctuations in temperatures during experiments. The uncertainty calculation for condensation heat flux ($q_c^{"}$) is obtained using following equations:

$$q_c^{"} = h_c \, \Delta T_{sub} \qquad \text{Equation A2}$$

$$\Delta q_c^{"} = h_{c,avg} \, (\Delta T_{sub,avg}) \sqrt{\left(\frac{\Delta h_c}{h_{c,avg}}\right)^2 + \left(\frac{\Delta(\Delta T_{sub})}{\Delta T_{sub,avg}}\right)^2} \qquad \text{Equation A3}$$

Where, $q_c^{"}$ is condensation heat flux (Wm^{-2}), h_c is condensation heat transfer coefficient ($Wm^{-2}K^{-1}$), ΔT_{sub} is the subcooling (temperature difference between nc-dep surface temperature and condensation chamber temperature, ^oC), $\Delta q_c^{"}$ is uncertainty associated with condensation heat flux (Wm^{-2}), Δh_c is uncertainty associated with condensation heat transfer coefficient ($Wm^{-2}K^{-1}$), $\Delta(\Delta T_{sub})$ is uncertainty associated with subcooling, ^oC).

Temperature collection rate during condensation on fresh porous nanochannel sample is given below:

Day 1-2: (a) First 2 hours: 30 data per hour, remaining 22 hours: 10 data per hour, (b) day 17-18: 30 data per hour for 48 hours.

The acquisition rate captures the fluctuations in the temperature and hence the deviation of heat transfer coefficient (HTC) from mean value; the higher the rate of acquisition, higher the sudden fluctuation in HTC and vice-versa. However, trend of mean HTC would not be affected as it is governed by surface wettability characteristics rather than sudden fluctuations in ambient and cold thermal fluid temperature. Moreover, automatic control of water level in vapor generation system will result in less variation in ambient temperature as in case of condensation on fresh LIS on porous nanochannel sample than a manually maintained water level as in case of condensation on depleted sample.

Appendix A2

A2.1 Tape Peeling Test

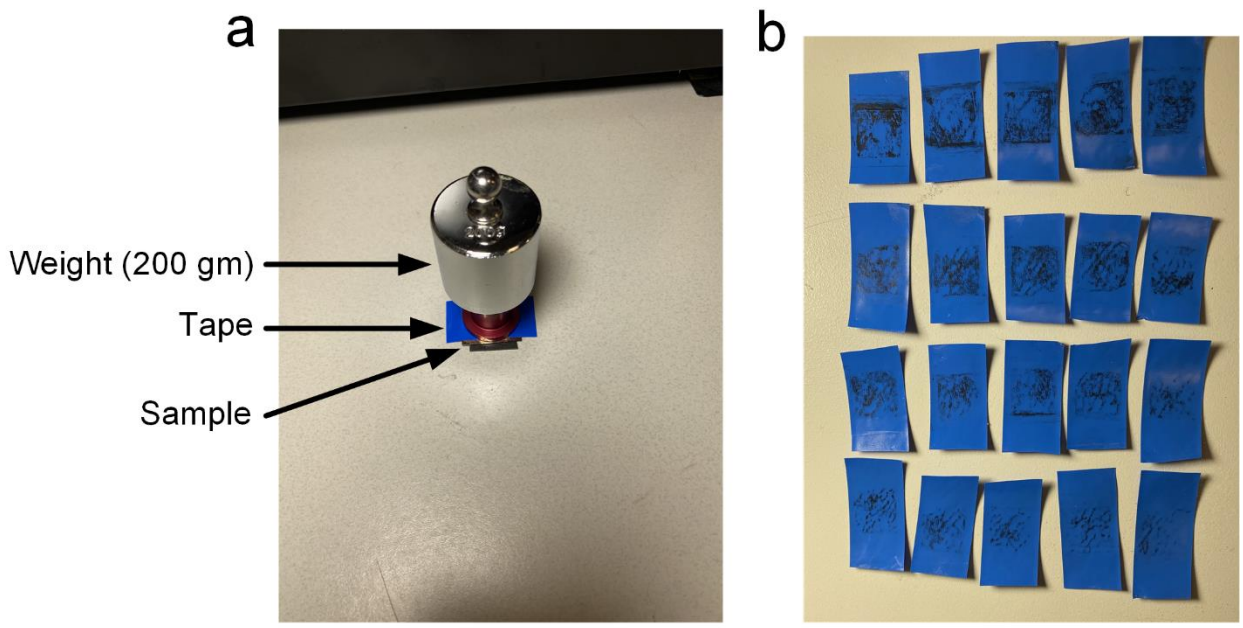

Figure A5. Tape peeling test. a) 207 gm weight kept on tape covering the coated surface for allowing sufficient adhesion of candle soot to tape. b) Coating removed by each cycle of tape peeling test. Decrease in removal rate of soot can be seen.

A2.2 UV Exposer and Solvent Submersion Test

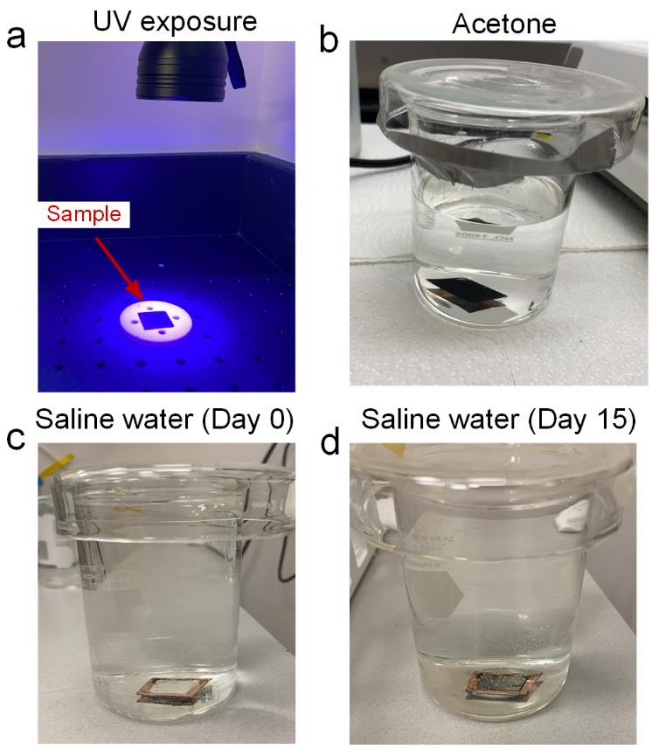

Figure A6. UV Exposer and Solvent Submersion Test. a) Experimental setup for ultraviolet light exposure. b) Nano-porous superhydrophobic surface (np-SHS) submerged under 5 *cm acetone. c) Visible plastron layer on np-SHS under* 10 *cm of saline solution*

A2.3 Frost-defrost Experimental Setup

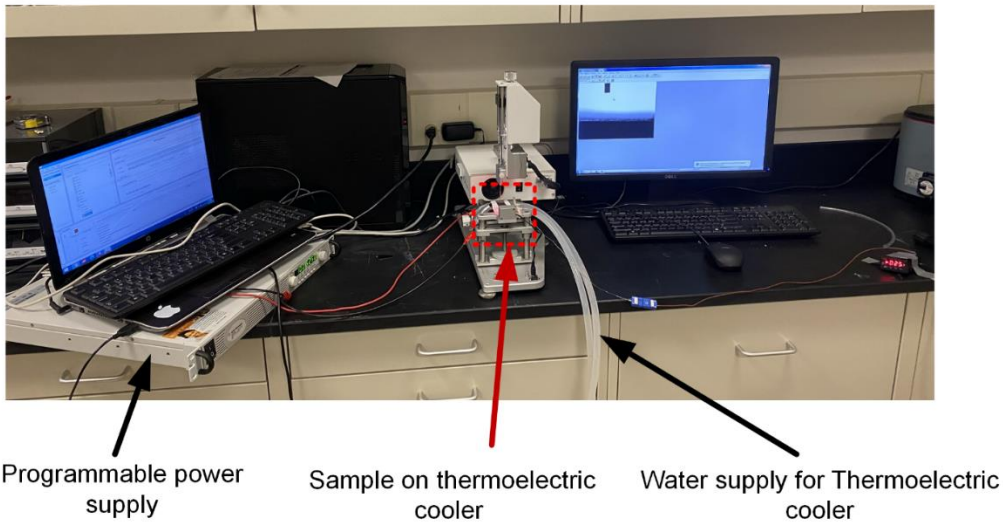

Figure A7. Experimental setup for frosting-defrosting test on nano-porous superhydrophobic surface (np-SHS). Programmable DC power supply controls the supply and maintains the power supply to thermoelectric cooler for a particular time before cutting off leading to defrosting. A total of 125 cycles were carried for 14.75 hours of experiment.

A2.3 Photothermal Response Experimental Setup

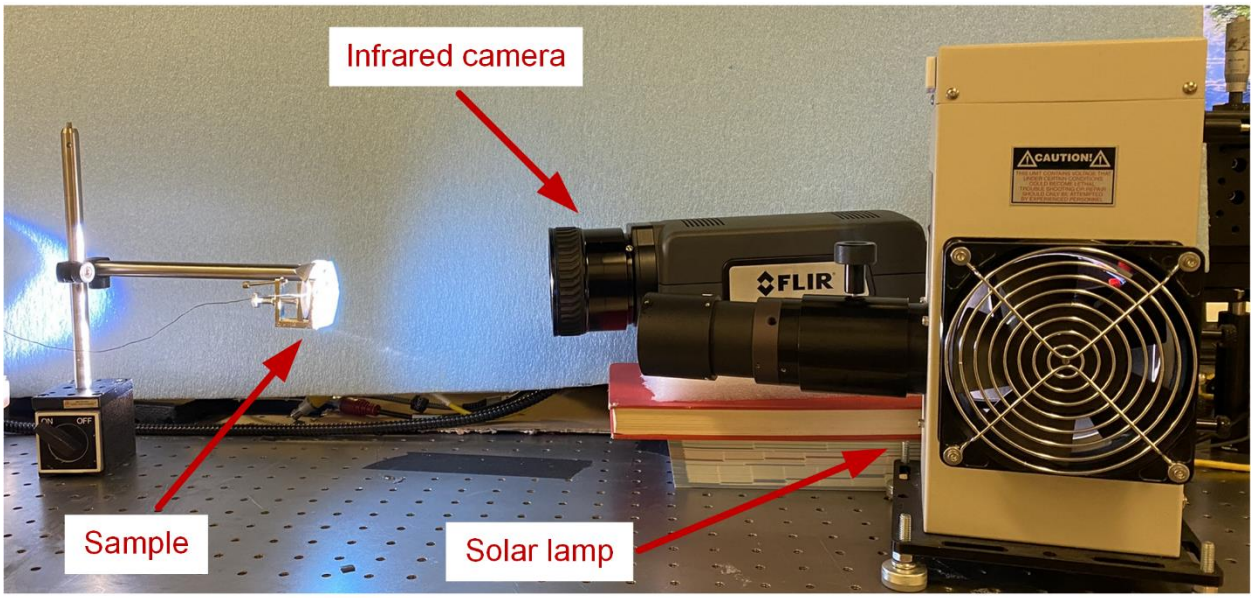

Figure A8. Experimental setup for photothermal response and emissivity calibration for nano-porous superhydrophobic surface (np-SHS).

Appendix A3

A3.1 Nanochannel Evaporator Fabrication Procedure

The nanochannel evaporator (nc-EVAP) consists of nanochannels fabricated in a four-inch silicon wafer anodic bonded with four-inch glass wafer shown in Figure A9. Fabrication of nanochannels and microreservoirs starts with a 500 μm silicon wafer. First stage of fabrication starts with wafer cleaning followed by 60 nm DUV 42P ARC layer and 600 nm UV210 photoresist coating using Gamma Automatic coat-develop tool. After exposure, wafer is hard baked and developed. Nanochannel etching is performed, followed by atomic force microscopy to acquire the nanochannel dimensions. In second stage, microreservoirs are fabricated 48 mm apart such that nanochannels function as bridges connecting microreservoirs. The nanochannel

etched wafer is plasma cleaned and coated with SPR 220-3 photoresist to obtain a ~ 3 μm coating on the wafer. Contact aligner is used to expose the PR at microreservoir locations. Please note that each wafer yields two nanochannel evaporator so, two micro-reservoirs are exposed on either side of nanochannels. After wafer development, 20 μm deep reservoirs are etched using Plasma-Therm deep silicon etcher. Wafer is then kept overnight in hot bath to remove PR. Third stage is bonding the silicon wafer with glass wafer. Glass wafer is cleaned, and 3 mm openings are laser cut such that they coincide with the center of microreservoirs. Anodic bonding is then performed, and nc-EVAP is cut in required size from bonded wafer using dicing saw.

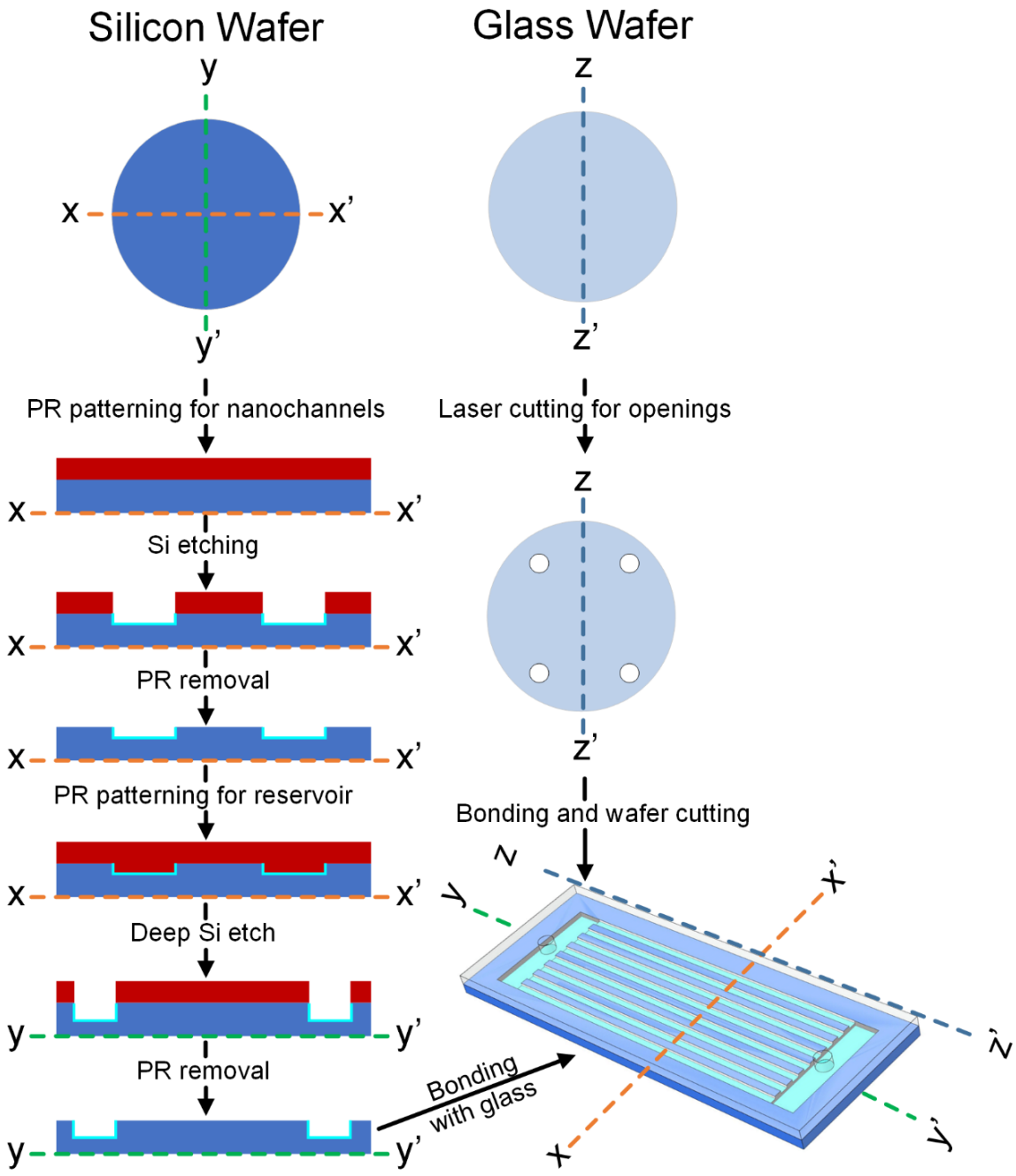

Figure A9. Nanochannel evaporator fabrication procedure.

A3.2 Heater Arrangements

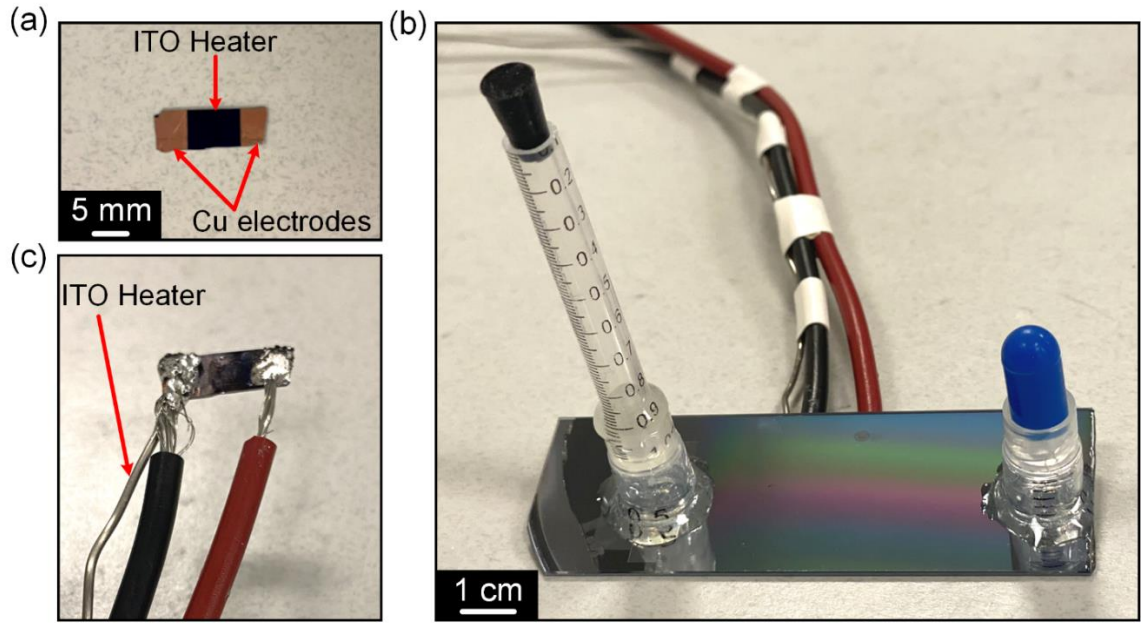

Figure A10. Heater Arrangements. (a) Resistive heater used in nanochannel evaporator (nc-EVAP). (b) Assembly of heater and nc-EVAP. (c) Wires soldered on the copper (Cu) electrodes and thermocouple attached to the heater.

A3.3 Uncertainties in Calculation

Uncertainities associated with weighing scale is 0.1 mg. For tube reservoir, the least count in scale marking is 0.01 ml. Based on these parameters, uncertainity in mass flux ($\Delta\ddot{m}_{ev}$) is given as:

$$\Delta\ddot{m}_{ev} = \ddot{m}_{ev}\sqrt{\left(\frac{\Delta(\Delta m)}{\Delta m}\right)^2 + \left(\frac{\Delta t_{ev}}{t_{ev}}\right)^2 + \left(\frac{\Delta A_{nc}}{A_{nc}}\right)} \qquad \text{Equation A4}$$

where, Δm is mass change of FC72 in the tube reservoir during evaporation (kg), t_{ev} is the total evaporation time (s), A_{nc} is the total cross-sectional area of nanochannels (m^2) excluding blocked channels.

Uncertainities in interfacial evaporation in cooling (Q_{ev}, W) is written as:

$$\Delta Q_{ev} = Q_{ev}\sqrt{\left(\frac{\Delta(\Delta V)}{\Delta V}\right)^2 + \left(\frac{\Delta t_{ss}}{t_{ss}}\right)^2} \quad \text{Equation A5}$$

where, Δt_{ss} is 1 s, $\Delta(\Delta V)$ = 0.01 ml.

Uncertainities in steady state interfacial evaporative heat flux ($\Delta q''_{ev}$) is given as:

$$\Delta q''_{ev} = q''_{ev}\sqrt{\left(\frac{\Delta(\Delta V)}{\Delta V}\right)^2 + \left(\frac{\Delta t_{ev}}{t_{ev}}\right)^2 + \left(\frac{\Delta A_{nc}}{A_{nc}}\right)} \quad \text{Equation A6}$$

Uncertainities in product of steady state interfacial evaporative heat flux and wicking distance is given as:

$$\Delta(q''_{ev}L_{wd}) = (q''_{ev}L_{wd})\sqrt{\left(\frac{\Delta q''_{ev}}{q''_{ev}}\right)^2 + \left(\frac{\Delta L_{wd}}{L_{wd}}\right)^2} \quad \text{Equation A7}$$

where, ΔL_{wd} is the uncertainty in wicking distance measurement (1 mm), and q''_{ev} is steady state interfacial evaporative heat flux.

Uncertainities in nc- HP efficiency calculation is given as:

$$\Delta\eta_{ev} = \eta_{ev}\sqrt{\left(\frac{\Delta Q_{ev}}{Q_{ev}}\right)^2 + \left(\frac{\Delta Q}{Q}\right)^2} \quad \text{Equation A8}$$

Since, error in supplied power to nc-EVAP (ΔQ) is negligible as compared to error asociated with Q_{ev}, second term in Equation A8 can be omitted.

References

1. And, J.H.L.I., and V, J.H.L. (2019) *A Heat transfer textbook*, Phlogiston Press, Cambridge Massachusetts.

2. Mudawar, I. (2001) Assessment of High-Heat-Flux Thermal. **24** (2), 122–141.

3. Semenic, T., and Catton, I. (2009) Experimental study of biporous wicks for high heat flux applications. *Int. J. Heat Mass Transf.*, **52** (21–22), 5113–5121.

4. McCarthy, M., Gerasopoulos, K., Maroo, S.C., and Hart, A.J. (2014) Materials, fabrication, and manufacturing of Micro/Nanostructured surfaces for phase-change heat transfer enhancement. *Nanoscale Microscale Thermophys. Eng.*, **18** (3), 288–310.

5. El Fil, B., Kini, G., and Garimella, S. (2020) A review of dropwise condensation: Theory, modeling, experiments, and applications. *Int. J. Heat Mass Transf.*, **160**.

6. Wang, C., He, B., Sun, S., Wu, Y., Yan, N., Yan, L., and Pei, X. (2012) Application of a low pressure economizer for waste heat recovery from the exhaust flue gas in a 600 MW power plant. *Energy*, **48** (1), 196–202.

7. Amon, C.H., Yao, S.C., Wu, C.F., and Hsieh, C.C. (2005) Microelectromechanical system-based evaporative thermal management of high heat flux electronics. *J. Heat Transfer*, **127** (1), 66–75.

8. Faghri, A., and Zhang, Y. (2020) *Fundamentals of Multiphase Heat Transfer and Flow*, Springer International Publishing.

9. Thome, J.R. (2006) The new frontier in heat transfer: Microscale and nanoscale technologies. *Heat Transf. Eng.*, **27** (9), 1–3.

10. Plawsky, J.L., Fedorov, A.G., Garimella, S. V., Ma, H.B., Maroo, S.C., Chen, L., and Nam, Y. (2014) Nano-and microstructures for thin-film evaporation-A review. *Nanoscale Microscale Thermophys. Eng.*, **18** (3), 251–269.

11. Jihong, A.-G., and Traian, D. (2018) Nano-scale Heat Transfer in Nanostructures: Toward Understanding and Engineering Thermal Transport. *Springer Int. Publ. AG*, (May).

12. Shalf, J. (2020) The future of computing beyond Moore ' s Law Subject Areas : *Philos. Trans. R. Soc.*, **378** (20190061), 1–14.

13. Villegas, M., Zhang, Y., Abu Jarad, N., Soleymani, L., and Didar, T.F. (2019) Liquid-Infused Surfaces: A Review of Theory, Design, and Applications. *ACS Nano*, **13** (8), 8517–8536.

14. Farnham, T.A., and Khalil, K.S. (2016) *Lubricant-Impregnated Surfaces*, The Royal Society of Chemistry.

15. Wong, T.S., Kang, S.H., Tang, S.K.Y., Smythe, E.J., Hatton, B.D., Grinthal, A., and Aizenberg, J. (2011) Bioinspired self-repairing slippery surfaces with pressure-stable omniphobicity. *Nature*, **477** (7365), 443–447.

16. Geim, A.K., Dubonos, S. V., Grigorieva, I. V., Novoselov, K.S., Zhukov, A.A., and Shapoval, S.Y. (2003) Microfabricated adhesive mimicking gecko foot-hair. *Nat. Mater.*, **2** (7), 461–463.

17. Lee, S.J., Kim, H.N., Choi, W., Yoon, G.Y., and Seo, E. (2019) A nature-inspired lubricant-infused surface for sustainable drag reduction. *Soft Matter*, **15** (42), 8459–8467.

18. Ashrafi, Z., Lucia, L., and Krause, W. (2019) Nature-Inspired Liquid Infused Systems for Superwettable Surface Energies. *ACS Appl. Mater. Interfaces*, **11** (24), 21275–21293.

19. Wei, C., Zhang, G., Zhang, Q., Zhan, X., and Chen, F. (2016) Silicone Oil-Infused Slippery Surfaces Based on Sol-Gel Process-Induced Nanocomposite Coatings: A Facile Approach to Highly Stable Bioinspired Surface for Biofouling Resistance. *ACS Appl. Mater. Interfaces*, **8** (50), 34810–34819.

20. Yin, J.L., Mei, M.L., Li, Q.L., Xia, R., Zhang, Z.H., and Chu, C.H. (2016)

Self-cleaning and antibiofouling enamel surface by slippery liquid-infused technique. *Sci. Rep.*, **6**.

21. Jing, X., and Guo, Z. (2019) Durable Lubricant-Impregnated Surfaces for Water Collection under Extremely Severe Working Conditions. *ACS Appl. Mater. Interfaces*, **11** (39), 35949–35958.

22. Rosenberg, B.J., Van Buren, T., Fu, M.K., and Smits, A.J. (2016) Turbulent drag reduction over air- and liquid- impregnated surfaces. *Phys. Fluids*, **28** (1).

23. Hemeda, A.A., and Tafreshi, H.V. (2016) Liquid-Infused Surfaces with Trapped Air (LISTA) for Drag Force Reduction. *Langmuir*, **32** (12), 2955–2962.

24. Howell, C., Grinthal, A., Sunny, S., Aizenberg, M., and Aizenberg, J. (2018) Designing Liquid-Infused Surfaces for Medical Applications: A Review. *Adv. Mater.*, **30** (50), 1–26.

25. Lee, J., Lee, M.H., and Choi, C.H. (2022) Design of Robust Lubricant-Infused Surfaces for Anti-Corrosion. *ACS Appl. Mater. Interfaces*, **14** (1), 2411–2423.

26. Jiang, S., Zhang, H., Song, K., and Liu, X. (2021) Corrosion protection application of liquid-infused surface with self-healing via regional growth of

layered double hydroxide films on aluminum alloy. *Colloids Surfaces A Physicochem. Eng. Asp.*, **612** (September 2020), 125996.

27. Enright, R., Miljkovic, N., Alvarado, J.L., Kim, K., and Rose, J.W. (2014) Dropwise condensation on micro-and nanostructured surfaces. *Nanoscale Microscale Thermophys. Eng.*, **18** (3), 223–250.

28. Xiao, R., Miljkovic, N., Enright, R., and Wang, E.N. (2013) Immersion condensation on oil-infused heterogeneous surfaces for enhanced heat transfer. *Sci. Rep.*, **3**.

29. Chiera, S., Koch, V.M., Bleyer, G., Walter, T., Bittner, C., Bachmann, J., and Vogel, N. (2022) From Sticky to Slippery: Self-Functionalizing Lubricants for in Situ Fabrication of Liquid-Infused Surfaces. *ACS Appl. Mater. Interfaces*, **14** (14), 16735–16745.

30. Peppou-Chapman, S., Hong, J.K., Waterhouse, A., and Neto, C. (2020) Life and death of liquid-infused surfaces: A review on the choice, analysis and fate of the infused liquid layer. *Chem. Soc. Rev.*, **49** (11), 3688–3715.

31. Adera, S., Alvarenga, J., Shneidman, A. V., Zhang, C.T., Davitt, A., and Aizenberg, J. (2020) Depletion of Lubricant from Nanostructured Oil-Infused Surfaces by Pendant Condensate Droplets. *ACS Nano*, **14** (7), 8024–8035.

32. Wexler, J.S., Jacobi, I., and Stone, H.A. (2015) Shear-driven failure of liquid-

infused surfaces. *Phys. Rev. Lett.*, **114** (16), 1–5.

33. Nishimoto, S., and Bhushan, B. (2013) Bioinspired self-cleaning surfaces with superhydrophobicity, superoleophobicity, and superhydrophilicity. *RSC Adv.*, **3** (3), 671–690.

34. Zheng, S., Li, C., Fu, Q., Hu, W., Xiang, T., Wang, Q., Du, M., Liu, X., and Chen, Z. (2016) Development of stable superhydrophobic coatings on aluminum surface for corrosion-resistant, self-cleaning, and anti-icing applications. *Mater. Des.*, **93**, 261–270.

35. Zhang, Y., Zhang, Z., Yang, J., Yue, Y., and Zhang, H. (2022) A Review of Recent Advances in Superhydrophobic Surfaces and Their Applications in Drag Reduction and Heat Transfer.

36. Marlena, J., Tan, J.K.S., Lin, Z., Li, D.X., Zhao, B., Leo, H.L., Kim, S., and Yap, C.H. (2021) Monolithic polymeric porous superhydrophobic material with pneumatic plastron stabilization for functionally durable drag reduction in blood-contacting biomedical applications. *NPG Asia Mater.*, **13** (1).

37. Gu, H., Li, G., Li, P., Liu, H., Chadyagondo, T.T., Li, N., and Xiong, J. (2020) Superhydrophobic and breathable SiO2/polyurethane porous membrane for durable water repellent application and oil-water separation. *Appl. Surf. Sci.*, **512** (November 2019).

38. Zhou, X., Zhang, Z., Xu, X., Guo, F., Zhu, X., Men, X., and Ge, B. (2013) Robust and durable superhydrophobic cotton fabrics for oil/water separation. *ACS Appl. Mater. Interfaces*, **5** (15), 7208–7214.

39. Boinovich, L.B., and Emelyanenko, A.M. (2013) Anti-icing potential of superhydrophobic coatings. *Mendeleev Commun.*, **23** (1), 3–10.

40. Parent, O., and Ilinca, A. (2011) Anti-icing and de-icing techniques for wind turbines: Critical review. *Cold Reg. Sci. Technol.*, **65** (1), 88–96.

41. Liao, R., Zuo, Z., Guo, C., Yuan, Y., and Zhuang, A. (2014) Fabrication of superhydrophobic surface on aluminum by continuous chemical etching and its anti-icing property. *Appl. Surf. Sci.*, **317**, 701–709.

42. Cheng, Y.T., and Rodak, D.E. (2005) Is the lotus leaf superhydrophobic? *Appl. Phys. Lett.*, **86** (14), 1–3.

43. Feng, L., Zhang, Y., Xi, J., Zhu, Y., Wang, N., Xia, F., and Jiang, L. (2008) Petal effect: A superhydrophobic state with high adhesive force. *Langmuir*, **24** (8), 4114–4119.

44. Zheng, Y., Gao, X., and Jiang, L. (2007) Directional adhesion of superhydrophobic butterfly wings. *Soft Matter*, **3** (2), 178–182.

45. Parvate, S., Dixit, P., and Chattopadhyay, S. (2020) Superhydrophobic

Surfaces: Insights from Theory and Experiment. *J. Phys. Chem. B*, **124** (8), 1323–1360.

46. Cassie, B.D. (1944) Of porous surfaces,. (5), 546–551.

47. Wang, J.N., Zhang, Y.L., Liu, Y., Zheng, W., Lee, L.P., and Sun, H.B. (2015) Recent developments in superhydrophobic graphene and graphene-related materials: From preparation to potential applications. *Nanoscale*, **7** (16), 7101–7114.

48. Allahdini, A., Jafari, R., and Momen, G. (2022) Transparent non-fluorinated superhydrophobic coating with enhanced anti-icing performance. *Prog. Org. Coatings*, **165** (January), 106758.

49. Zhang, L., Zhou, A.G., Sun, B.R., Chen, K.S., and Yu, H.Z. (2021) Functional and versatile superhydrophobic coatings via stoichiometric silanization. *Nat. Commun.*, **12** (1), 1–7.

50. Sutar, R.S., Latthe, S.S., Nagappan, S., Ha, C.S., Sadasivuni, K.K., Liu, S., Xing, R., and Bhosale, A.K. (2021) Fabrication of robust self-cleaning superhydrophobic coating by deposition of polymer layer on candle soot surface. *J. Appl. Polym. Sci.*, **138** (9).

51. Li, M., Luo, W., Sun, H., Xu, J., Liu, Y., and Cheng, X. (2022) Superhydrophobic coatings fabricated by paraffin wax and silica

nanoparticles with enhanced adhesion stability. *Mater. Lett.*, **309** (November 2021), 131316.

52. Do, V.-T., and Chun, D.-M. (2022) Fabrication of large-scale, flexible, and robust superhydrophobic composite films using hydrophobic fumed silica nanoparticles and polydimethylsiloxane. *Polymer (Guildf).*, **244** (February), 124630.

53. Chakradhar, R.P.S., Kumar, V.D., Rao, J.L., and Basu, B.J. (2011) Fabrication of superhydrophobic surfaces based on ZnO-PDMS nanocomposite coatings and study of its wetting behaviour. *Appl. Surf. Sci.*, **257** (20), 8569–8575.

54. Wu, B., Cui, X., Jiang, H., Wu, N., Peng, C., Hu, Z., Liang, X., Yan, Y., Huang, J., and Li, D. (2021) A superhydrophobic coating harvesting mechanical robustness, passive anti-icing and active de-icing performances. *J. Colloid Interface Sci.*, **590**, 301–310.

55. Ma, W., Li, Y., Chao, C.Y.H., Tso, C.Y., Huang, B., Li, W., and Yao, S. (2021) Solar-assisted icephobicity down to −60°C with superhydrophobic selective surfaces. *Cell Reports Phys. Sci.*, **2** (3), 100384.

56. Li, J., Tian, J., Gao, Y., Qin, R., Pi, H., Li, M., and Yang, P. (2021) All-natural superhydrophobic coating for packaging and blood-repelling

materials. *Chem. Eng. J.*, **410** (December 2020), 128347.

57. Peng, C., Chen, Z., and Tiwari, M.K. (2018) All-organic superhydrophobic coatings with mechanochemical robustness and liquid impalement resistance. *Nat. Mater.*, **17** (4), 355–360.

58. Song, M., Hu, D., Zheng, X., Wang, L., Yu, Z., An, W., Na, R., Li, C., Li, N., Lu, Z., Dong, Z., Wang, Y., and Jiang, L. (2019) Enhancing Droplet Deposition on Wired and Curved Superhydrophobic Leaves. *ACS Nano*, **13** (7), 7966–7974.

59. Deng, X., Mammen, L., Butt, H.J., and Vollmer, D. (2012) Candle soot as a template for a transparent robust superamphiphobic coating. *Science (80-.).*, **335** (6064), 67–70.

60. Sheng, X., and Zhang, J. (2011) Air layer on superhydrophobic surface underwater. *Colloids Surfaces A Physicochem. Eng. Asp.*, **377** (1–3), 374–378.

61. Xiong, Z.C., Zhu, Y.J., Qin, D.D., and Yang, R.L. (2020) Flexible Salt-Rejecting Photothermal Paper Based on Reduced Graphene Oxide and Hydroxyapatite Nanowires for High-Efficiency Solar Energy-Driven Vapor Generation and Stable Desalination. *ACS Appl. Mater. Interfaces*, **12** (29), 32556–32565.

62. Elimelech, M., and Phillip, W.A. (2011) The future of seawater desalination: Energy, technology, and the environment. *Science (80-.).*, **333** (6043), 712–717.

63. Ziviani, D., Beyene, A., and Venturini, M. (2014) Advances and challenges in ORC systems modeling for low grade thermal energy recovery. *Appl. Energy*, **121**, 79–95.

64. Zhang, B.J., Zhang, Z.L., Liu, K., and Chen, Q.L. (2016) Network Modeling and Design for Low Grade Heat Recovery, Refrigeration, and Utilization in Industrial Parks. *Ind. Eng. Chem. Res.*, **55** (36), 9725–9737.

65. Fermanel, F., and Miriel, J. (1999) Air heating system: Influence of a humidifier on thermal comfort. *Appl. Therm. Eng.*, **19** (10), 1107–1127.

66. Chang, C., Tao, P., Xu, J., Fu, B., Song, C., Wu, J., Shang, W., and Deng, T. (2019) High-Efficiency Superheated Steam Generation for Portable Sterilization under Ambient Pressure and Low Solar Flux. *ACS Appl. Mater. Interfaces*, **11** (20), 18466–18474.

67. Kabir, E., Kumar, P., Kumar, S., Adelodun, A.A., and Kim, K.H. (2018) Solar energy: Potential and future prospects. *Renew. Sustain. Energy Rev.*, **82** (September 2017), 894–900.

68. Chang, C., Yang, C., Liu, Y., Tao, P., Song, C., Shang, W., Wu, J., and

Deng, T. (2016) Efficient solar-thermal energy harvest driven by interfacial plasmonic heating-assisted evaporation. *ACS Appl. Mater. Interfaces*, **8** (35), 23412–23418.

69. Grtzel, M., and Moser, J.E. (2008) Solar Energy Conversion. *Electron Transf. Chem.*, **5** (March), 589–644.

70. Amjad, M., Raza, G., Xin, Y., Pervaiz, S., Xu, J., Du, X., and Wen, D. (2017) Volumetric solar heating and steam generation via gold nanofluids. *Appl. Energy*, **206** (March), 393–400.

71. Neumann, O., Urban, A.S., Day, J., Lal, S., Nordlander, P., and Halas, N.J. (2013) Solar vapor generation enabled by nanoparticles. *ACS Nano*, **7** (1), 42–49.

72. Li, Y., Jin, X., Zheng, Y., Li, W., Zheng, F., Wang, W., Lin, T., and Zhu, Z. (2019) Tunable Water Delivery in Carbon-Coated Fabrics for High-Efficiency Solar Vapor Generation. *ACS Appl. Mater. Interfaces*, **11** (50), 46938–46946.

73. Cao, S., Jiang, Q., Wu, X., Ghim, D., Gholami Derami, H., Chou, P.I., Jun, Y.S., and Singamaneni, S. (2019) Advances in solar evaporator materials for freshwater generation. *J. Mater. Chem. A*, **7** (42), 24092–24123.

74. Yin, Z., Wang, H., Jian, M., Li, Y., Xia, K., Zhang, M., Wang, C., Wang, Q.,

Ma, M., Zheng, Q.S., and Zhang, Y. (2017) Extremely Black Vertically Aligned Carbon Nanotube Arrays for Solar Steam Generation. *ACS Appl. Mater. Interfaces*, **9** (34), 28596–28603.

75. Jiang, F., Liu, H., Li, Y., Kuang, Y., Xu, X., Chen, C., Huang, H., Jia, C., Zhao, X., Hitz, E., Zhou, Y., Yang, R., Cui, L., and Hu, L. (2018) Lightweight, Mesoporous, and Highly Absorptive All-Nanofiber Aerogel for Efficient Solar Steam Generation. *ACS Appl. Mater. Interfaces*, **10** (1), 1104–1112.

76. Ghasemi, H., Ni, G., Marconnet, A.M., Loomis, J., Yerci, S., Miljkovic, N., and Chen, G. (2014) Solar steam generation by heat localization. *Nat. Commun.*, **5**, 1–7.

77. Zhong, J., Huang, C., and Wu, D. (2018) Surrounding effects on the evaporation efficiency of a bi-layered structure for solar steam generation. *Appl. Therm. Eng.*, **144** (June), 331–341.

78. Go, K., Bae, K., Choi, H., Kim, H.Y., and Lee, K.J. (2019) Solar-to-Steam Generation via Porous Black Membranes with Tailored Pore Structures. *ACS Appl. Mater. Interfaces*, **11** (51), 48300–48308.

79. Tao, F., Valenzuela Garcia, A., Xiao, T., Zhang, Y., Yin, Y., and Chen, X. (2020) Interfacial Solar Vapor Generation: Introducing Students to

Experimental Procedures and Analysis for Efficiently Harvesting Energy and Generating Vapor at the Air-Water Interface. *J. Chem. Educ.*, **97** (4), 1093–1100.

80. Tao, P., Ni, G., Song, C., Shang, W., Wu, J., Zhu, J., Chen, G., and Deng, T. (2018) Solar-driven interfacial evaporation. *Nat. Energy*, **3** (12), 1031–1041.

81. Zhang, P., Liao, Q., Yao, H., Huang, Y., Cheng, H., and Qu, L. (2019) Direct solar steam generation system for clean water production. *Energy Storage Mater.*, **18** (August 2018), 429–446.

82. Zhu, L., Gao, M., Peh, C.K.N., and Ho, G.W. (2019) Recent progress in solar-driven interfacial water evaporation: Advanced designs and applications. *Nano Energy*, **57**, 507–518.

83. Yang, Z.P., Ci, L., Bur, J.A., Lin, S.Y., and Ajayan, P.M. (2008) Experimental observation of an extremely dark material made by a low-density nanotube array. *Nano Lett.*, **8** (2), 446–451.

84. Yuan, Q., Lin, C. Te, and Chee, K.W.A. (2019) All-carbon devices based on sp 2 -on-sp 3 configuration. *APL Mater.*, **7** (3).

85. Chen, T., Wang, S., Wu, Z., Wang, X., Peng, J., Wu, B., Cui, J., Fang, X., Xie, Y., and Zheng, N. (2018) A cake making strategy to prepare reduced graphene oxide wrapped plant fiber sponges for high-efficiency solar steam

generation. *J. Mater. Chem. A*, **6** (30), 14571–14576.

86. Zhang, P., Li, J., Lv, L., Zhao, Y., and Qu, L. (2017) Vertically Aligned Graphene Sheets Membrane for Highly Efficient Solar Thermal Generation of Clean Water. *ACS Nano*, **11** (5), 5087–5093.

87. Dao, V.-D., and Choi, H.-S. (2018) Carbon-Based Sunlight Absorbers in Solar-Driven Steam Generation Devices. *Glob. Challenges*, **2** (2), 1700094.

88. Guo, A., Ming, X., Fu, Y., Wang, G., and Wang, X. (2017) Fiber-Based, Double-Sided, Reduced Graphene Oxide Films for Efficient Solar Vapor Generation. *ACS Appl. Mater. Interfaces*, **9** (35), 29958–29964.

89. Sun, P., Zhang, W., Zada, I., Zhang, Y., Gu, J., Liu, Q., Su, H., Pantelić, D., Jelenković, B., and Zhang, D. (2020) 3D-Structured Carbonized Sunflower Heads for Improved Energy Efficiency in Solar Steam Generation. *ACS Appl. Mater. Interfaces*, **12** (2), 2171–2179.

90. Chen, S., Sun, Z., Xiang, W., Shen, C., Wang, Z., Jia, X., Sun, J., and Liu, C.J. (2020) Plasmonic wooden flower for highly efficient solar vapor generation. *Nano Energy*, **76** (June), 104998.

91. Tao, F., Zhang, Y., Yin, K., Cao, S., Chang, X., Lei, Y., Wang, D.S., Fan, R., Dong, L., Yin, Y., and Chen, X. (2018) Copper Sulfide-Based Plasmonic Photothermal Membrane for High-Efficiency Solar Vapor Generation. *ACS*

Appl. Mater. Interfaces, **10** (41), 35154–35163.

92. Shi, Y., Li, R., Jin, Y., Zhuo, S., Shi, L., Chang, J., Hong, S., Ng, K.C., and Wang, P. (2018) A 3D Photothermal Structure toward Improved Energy Efficiency in Solar Steam Generation. *Joule*, **2** (6), 1171–1186.

93. Zhu, G., Xu, J., Zhao, W., and Huang, F. (2016) Constructing black titania with unique nanocage structure for solar desalination. *ACS Appl. Mater. Interfaces*, **8** (46), 31716–31721.

94. Ranjan, R., Murthy, J.Y., and Garimella, S. V. (2009) Analysis of the wicking and thin-film evaporation characteristics of microstructures. *J. Heat Transfer*, **131** (10), 1–11.

95. Somasundaram, S., Zhu, Y., Lu, Z., Adera, S., Bin, H., Mengyao, W., Tan, C.S., and Wang, E.N. (2018) Thermal design optimization of evaporator micropillar wicks. *Int. J. Therm. Sci.*, **134** (March 2017), 179–187.

96. Adera, S., Antao, D., Raj, R., and Wang, E.N. (2016) Design of micropillar wicks for thin-film evaporation. *Int. J. Heat Mass Transf.*, **101**, 280–294.

97. Plawsky, J.L., Fedorov, A.G., Garimella, S. V, Ma, H.B., Maroo, S.C., Chen, L., Plawsky, J.L., Fedorov, A.G., Garimella, S. V, Ma, H.B., and Carolina, S. (2014) Nano- and Microstructures for Thin-Film Evaporation — A Review. **7265**.

98. Xiao, R., Maroo, S.C., and Wang, E.N. (2012) Thin film evaporation using nanoporous membranes for enhanced heat transfer. *ASME 2012 Heat Transf. Summer Conf. Collocated with ASME 2012 Fluids Eng. Div. Summer Meet. ASME 2012 10th Int. Conf. Nanochannels, Microchannels Minichannels, HT 2012*, **2**, 103–107.

99. Zheng, D., Choi, C.H., Sun, G., and Zhao, X. (2020) Superwicking on Nanoporous Micropillared Surfaces. *ACS Appl. Mater. Interfaces*, **12** (27), 30925–30931.

100. Băjenescu, T.M.I. (2021) Miniaturisation of electronic components and the problem of devices overheating. *EEA - Electroteh. Electron. Autom.*, **69** (2), 53–58.

101. Cho, J., and Goodson, K.E. (2015) Thermal transport: Cool electronics. *Nat. Mater.*, **14** (2), 136–137.

102. He, Z., Yan, Y., and Zhang, Z. (2021) Thermal management and temperature uniformity enhancement of electronic devices by micro heat sinks: A review. *Energy*, **216**, 119223.

103. Naqiuddin, N.H., Saw, L.H., Yew, M.C., Yusof, F., Ng, T.C., and Yew, M.K. (2018) Overview of micro-channel design for high heat flux application. *Renew. Sustain. Energy Rev.*, **82** (October 2017), 901–914.

104. Ribatski, G., Cabezas-Gómez, L., Navarro, H.A., and Saíz-Jabardo, J.M. (2007) the Advantages of Evaporation in Micro-Scale Channels To Cool Microeletronic Devices. *Rev. Eng. Térmica*, **6** (2), 34.

105. Zhang, N., Jiao, B., Ye, Y., Kong, Y., Du, X., Liu, R., Cong, B., Yu, L., Jia, S., and Jia, K. (2022) Embedded cooling method with configurability and replaceability for multi-chip electronic devices. *Energy Convers. Manag.*, **253** (December 2021), 115124.

106. Faghri, A. (2012) Review and advances in heat pipe science and technology. *J. Heat Transfer*, **134** (12), 1–18.

107. De Bock, H.P.J., Varanasi, K., Chamarthy, P., Deng, T., Kulkarni, A., Rush, B.M., Russ, B.A., Weaver, S.E., and Gerner, F.M. (2009) Experimental investigation of micro/nano heat pipe wick structures. *ASME Int. Mech. Eng. Congr. Expo. Proc.*, **10** (PART B), 991–996.

108. Subrina, S., Kotchetkov, D., and Balandin, A.A. (2009) Heat removal in silicon-on-insulator integrated circuits with graphene lateral heat spreaders. *IEEE Electron Device Lett.*, **30** (12), 1281–1283.

109. Nazari, M., Masoudi, A., Jafari, P., Irajizad, P., Kashyap, V., and Ghasemi, H. (2019) Ultrahigh Evaporative Heat Fluxes in Nanoconfined Geometries. *Langmuir*, **35** (1), 78–85.

110. Hanks, D.F., Lu, Z., Sircar, J., Salamon, T.R., Antao, D.S., Bagnall, K.R., Barabadi, B., and Wang, E.N. (2018) Nanoporous membrane device for ultra high heat flux thermal management. *Microsystems Nanoeng.*, **4** (1), 1–10.

111. Hanks, D.F., Lu, Z., Sircar, J., Kinefuchi, I., Bagnall, K.R., Salamon, T.R., Antao, D.S., Barabadi, B., and Wang, E.N. (2020) High heat flux evaporation of low surface tension liquids from nanoporous membranes. *ACS Appl. Mater. Interfaces*, **12** (6), 7232–7238.

112. Hsieh, S.S., Lee, R.Y., Shyu, J.C., and Chen, S.W. (2008) Thermal performance of flat vapor chamber heat spreader. *Energy Convers. Manag.*, **49** (6), 1774–1784.

113. Kumaresan, G., Venkatachalapathy, S., and Asirvatham, L.G. (2014) Experimental investigation on enhancement in thermal characteristics of sintered wick heat pipe using CuO nanofluids. *Int. J. Heat Mass Transf.*, **72**, 507–516.

114. Jafari, D., Wits, W.W., and Geurts, B.J. (2018) Metal 3D-printed wick structures for heat pipe application: Capillary performance analysis. *Appl. Therm. Eng.*, **143** (May), 403–414.

115. Kunugi, T., Muko, K., and Shibahara, M. (2004) Ultrahigh heat transfer enhancement using nano-porous layer. *Superlattices Microstruct.*, **35** (3–6),

531–542.

116. Li, Y., Alibakhshi, M.A., Zhao, Y., and Duan, C. (2017) Exploring Ultimate Water Capillary Evaporation in Nanoscale Conduits. *Nano Lett.*, **17** (8), 4813–4819.

117. Lu, Z., Salamon, T.R., Narayanan, S., Bagnall, K.R., Hanks, D.F., Antao, D.S., Barabadi, B., Sircar, J., Simon, M.E., and Wang, E.N. (2016) Design and modeling of membrane-based evaporative cooling devices for thermal management of high heat fluxes. *IEEE Trans. Components, Packag. Manuf. Technol.*, **6** (7), 1056–1065.

118. Mehta, K.K., Mehta, N., and Patel, V. (2019) Effect of operational parameters on the thermal performance of flat plate oscillating heat pipe. *J. Heat Transfer*, **141** (12), 1–8.

119. Zhang, X.M., Xu, J.L., and Zhou, Z.Q. (2004) Experimental study of a pulsating heat pipe using fc-72, ethanol, and water as working fluids. *Exp. Heat Transf.*, **17** (1), 47–67.

120. Narayanan, S., Fedorov, A.G., and Joshi, Y.K. (2009) Gas-assisted thin-film evaporation from confined spaces for dissipation of high heat fluxes. *Nanoscale Microscale Thermophys. Eng.*, **13** (1), 30–53.

121. Nahar, M.M., Ma, B., Guye, K., Chau, Q.H., Padilla, J., Iyengar, M., and

Agonafer, D. (2021) Review article: Microscale evaporative cooling technologies for high heat flux microelectronics devices: Background and recent advances. *Appl. Therm. Eng.*, **194** (April), 117109.

122. Ma, Q., Wang, W., and Dong, G. (2019) Facile fabrication of biomimetic liquid-infused slippery surface on carbon steel and its self-cleaning, anti-corrosion, anti-frosting and tribological properties. *Colloids Surfaces A Physicochem. Eng. Asp.*, **577** (March), 17–26.

123. Afonso, E., Martínez-Gómez, A., Tiemblo, P., and García, N. (2021) Industrially viable method for producing all-polymer hydrophobic surfaces apt for slippery liquid-infused substrates. *Appl. Surf. Sci.*, **535** (June 2020), 147728.

124. Tsuchiya, H., Tenjimbayashi, M., Moriya, T., Yoshikawa, R., Sasaki, K., Togasawa, R., Yamazaki, T., Manabe, K., and Shiratori, S. (2017) Liquid-Infused Smooth Surface for Improved Condensation Heat Transfer. *Langmuir*, **33** (36), 8950–8960.

125. Preston, D.J., Lu, Z., Song, Y., Zhao, Y., Wilke, K.L., Antao, D.S., Louis, M., and Wang, E.N. (2018) Heat Transfer Enhancement during Water and Hydrocarbon Condensation on Lubricant Infused Surfaces. *Sci. Rep.*, **8** (1), 1–9.

126. Gulfam, R., Huang, T. en, Lv, C., Orejon, D., and Zhang, P. (2022) Condensation heat transfer on phase change slippery liquid-infused porous surfaces. *Int. J. Heat Mass Transf.*, **185**, 122384.

127. Sett, S., Yan, X., Barac, G., Bolton, L.W., and Miljkovic, N. (2017) Lubricant-Infused Surfaces for Low-Surface-Tension Fluids: Promise versus Reality. *ACS Appl. Mater. Interfaces*, **9** (41), 36400–36408.

128. Wang, P., Zhang, D., Sun, S., Li, T., and Sun, Y. (2017) Fabrication of slippery lubricant-infused porous surface with high underwater transparency for the control of marine biofouling. *ACS Appl. Mater. Interfaces*, **9** (1), 972–982.

129. Goodband, S.J., Armstrong, S., Kusumaatmaja, H., and Vol¨tchovsky, K. (2020) Effect of Ageing on the Structure and Properties of Model Liquid-Infused Surfaces. *Langmuir*, **36** (13), 3461–3470.

130. Seiwert, J., Clanet, C., and Quéré, D. (2011) Coating of a textured solid. *J. Fluid Mech.*, **669**, 55–63.

131. Seo, D., Shim, J., Lee, C., and Nam, Y. (2020) Brushed lubricant-impregnated surfaces (BLIS) for long-lasting high condensation heat transfer. *Sci. Rep.*, **10** (1).

132. Zhang, Y., Zhang, L., Xiao, Z., Wang, S., and Yu, X. (2019) Fabrication of

robust and repairable superhydrophobic coatings by an immersion method. *Chem. Eng. J.*, **369**, 1–7.

133. Hoque, M.J., Sett, S., Yan, X., Liu, D., Rabbi, K.F., Qiu, H., Qureshi, M., Barac, G., Bolton, L., and Miljkovic, N. (2022) Life Span of Slippery Lubricant Infused Surfaces. *ACS Appl. Mater. Interfaces*, **14** (3), 4598–4611.

134. Rose, J.W. (2002) Dropwise condensation theory and experiment: A review. *Proc. Inst. Mech. Eng. Part A J. Power Energy*, **216** (2), 115–128.

135. Smith, J.D., Dhiman, R., Anand, S., Reza-Garduno, E., Cohen, R.E., McKinley, G.H., and Varanasi, K.K. (2013) Droplet mobility on lubricant-impregnated surfaces. *Soft Matter*, **9** (6), 1772–1780.

136. Minkowycz, W.J., and Sparrow, E.M. (1966) Heat Transfer Variable Diffusion in the Presence Resistance , and of Noncondensables , Interfacial. *Int. J. Heat Mass Transf.*, **9**, 1125–1144.

137. Tanner, D.W., Pope, D., Potter, C.J., and West, D. (1968) Heat transfer in dropwise condensation at low steam pressures in the absence and presence of non-condensable gas. *Int. J. Heat Mass Transf.*, **11** (2), 181–190.

138. Hu, H.W., Tang, G.H., and Niu, D. (2015) Experimental investigation of condensation heat transfer on hybrid wettability finned tube with large amount of noncondensable gas. *Int. J. Heat Mass Transf.*, **85**, 513–523.

139. Quan, X., Chen, S., Li, J., and Cheng, P. (2018) Enhanced dropwise condensation by oil infused nano-grass coatings on outer surface of a horizontal copper tube. *Int. Commun. Heat Mass Transf.*, **91** (December 2017), 11–16.

140. Poudel, S., Zou, A., and Maroo, S.C. (2019) Wicking in Cross-Connected Buried Nanochannels. *J. Phys. Chem. C*, **123** (38), 1–6.

141. Zou, A., Poudel, S., Raut, S.P., and Maroo, S.C. (2019) Pool Boiling Coupled with Nanoscale Evaporation Using Buried Nanochannels. *Langmuir*, **35** (39), 12689–12693.

142. Plasma treatment of silicon dioxide for imp.pdf.

143. (2004) Plasma treatment of allograft. *Res. Discl.*, (483), 1029.

144. Jiang, L., Li, S., Wang, J., Yang, L., Sun, Q., and Li, Z. (2014) Surface wettability of oxygen plasma treated porous silicon. *J. Nanomater.*, **2014**.

145. Keiser, A., Keiser, L., Clanet, C., and Quéré, D. (2017) Drop friction on liquid-infused materials. *Soft Matter*, **13** (39), 6981–6987.

146. Kim, P., Kreder, M.J., Alvarenga, J., and Aizenberg, J. (2013) Hierarchical or not? Effect of the length scale and hierarchy of the surface roughness on omniphobicity of lubricant-infused substrates. *Nano Lett.*, **13** (4), 1793–1799.

147. Kim, J.H., and Rothstein, J.P. (2016) Droplet Impact Dynamics on Lubricant-Infused Superhydrophobic Surfaces: The Role of Viscosity Ratio. *Langmuir*, **32** (40), 10166–10176.

148. Peppou-Chapman, S., and Neto, C. (2018) Mapping Depletion of Lubricant Films on Antibiofouling Wrinkled Slippery Surfaces. *ACS Appl. Mater. Interfaces*, **10** (39), 33669–33677.

149. Sasidharanpillai, A., Lee, Y., and Lee, S. (2022) Design of stable liquid infused surfaces: Influence of oil viscosity on stability. *Colloids Surfaces A Physicochem. Eng. Asp.*, **646** (March), 128923.

150. Gunjan, M.R., Kumar, A., and Raj, R. (2020) Droplets on Lubricant-Infused Surfaces: Combination of Constant Mean Curvature Interfaces with Neumann Triangle Boundary Conditions.

151. Hu, H.W., Tang, G.H., and Niu, D. (2015) Experimental investigation of condensation heat transfer on hybrid wettability finned tube with large amount of noncondensable gas. *Int. J. Heat Mass Transf.*, **85**, 513–523.

152. Yi, Q., Tian, M., Yan, W., Qu, X., and Chen, X. (2016) Visualization study of the influence of non-condensable gas on steam condensation heat transfer. *Appl. Therm. Eng.*, **106**, 13–21.

153. El Fouhaili, B., Ibrahim, A., Dietlin, C., Chemtob, A., Allonas, X., and

Croutxé-Barghorn, C. (2019) Single-step formation of superhydrophobic surfaces using photobase-catalyzed sol-gel process. *Prog. Org. Coatings*, **137** (March), 105293.

154. Li, J., Zhou, Y., Wang, W., Xu, C., and Ren, L. (2020) Superhydrophobic Copper Surface Textured by Laser for Delayed Icing Phenomenon. *Langmuir*, **36** (5), 1075–1082.

155. Saleh, T.A., and Baig, N. (2019) Efficient chemical etching procedure for the generation of superhydrophobic surfaces for separation of oil from water. *Prog. Org. Coatings*, **133** (April), 27–32.

156. Yan, Y.Y., Gao, N., and Barthlott, W. (2011) Mimicking natural superhydrophobic surfaces and grasping the wetting process: A review on recent progress in preparing superhydrophobic surfaces. *Adv. Colloid Interface Sci.*, **169** (2), 80–105.

157. Subeshan, B., Usta, A., and Asmatulu, R. (2020) Deicing and self-cleaning of plasma-treated superhydrophobic coatings on the surface of aluminum alloy sheets. *Surfaces and Interfaces*, **18** (January), 100429.

158. Zhang, X., Shi, F., Niu, J., Jiang, Y., and Wang, Z. (2008) Superhydrophobic surfaces: From structural control to functional application. *J. Mater. Chem.*, **18** (6), 621–633.

159. Lin, X., Park, S., Choi, D., Heo, J., and Hong, J. (2019) Mechanically durable superhydrophobic PDMS-candle soot composite coatings with high biocompatibility. *J. Ind. Eng. Chem.*, **74**, 79–85.

160. Zhang, P., and Wang, S. (2014) Designing fractal nanostructured biointerfaces for biomedical applications. *ChemPhysChem*, **15** (8), 1550–1561.

161. Mulay, M.R., Chauhan, A., Patel, S., Balakrishnan, V., Halder, A., and Vaish, R. (2019) Candle soot: Journey from a pollutant to a functional material. *Carbon N. Y.*, **144**, 684–712.

162. Xiao, L., Zeng, W., Liao, G., Yi, C., and Xu, Z. (2018) Thermally and Chemically Stable Candle Soot Superhydrophobic Surface with Excellent Self-Cleaning Properties in Air and Oil. *ACS Appl. Nano Mater.*, **1** (3), 1204–1211.

163. Wu, S., Du, Y., Alsaid, Y., Wu, D., Hua, M., Yan, Y., Yao, B., Ma, Y., Zhu, X., and He, X. (2020) Superhydrophobic photothermal icephobic surfaces based on candle soot. *Proc. Natl. Acad. Sci. U. S. A.*, **117** (21).

164. Seo, K., Kim, M., and Kim, D.H. (2014) Candle-based process for creating a stable superhydrophobic surface. *Carbon N. Y.*, **68**, 583–596.

165. Zhang, B., Duan, J., Huang, Y., and Hou, B. (2021) Double layered

superhydrophobic PDMS-Candle soot coating with durable corrosion resistance and thermal-mechanical robustness. *J. Mater. Sci. Technol.*, **71**, 1–11.

166. Jamil, M.I., Zhan, X., Chen, F., Cheng, D., and Zhang, Q. (2019) Durable and Scalable Candle Soot Icephobic Coating with Nucleation and Fracture Mechanism. *ACS Appl. Mater. Interfaces*, **11** (34), 31532–31542.

167. Yang, C., Li, Z., Huang, Y., Wang, K., Long, Y., Guo, Z., Li, X., and Wu, H. (2021) Continuous Roll-to-Roll Production of Carbon Nanoparticles from Candle Soot. *Nano Lett.*, **21** (7), 3198–3204.

168. Liu, X., Zhang, X., Chen, Q., Pan, Y., Liu, C., and Shen, C. (2021) A simple superhydrophobic/superhydrophilic Janus-paper with enhanced biocompatibility by PDMS and candle soot coating for actuator. *Chem. Eng. J.*, **406** (August 2020), 126532.

169. Lee, E., and Lee, K.H. (2018) Facile fabrication of superhydrophobic surfaces with hierarchical structures. *Sci. Rep.*, **8** (1), 1–7.

170. Iqbal, R., Majhy, B., and Sen, A.K. (2017) Facile Fabrication and Characterization of a PDMS-Derived Candle Soot Coated Stable Biocompatible Superhydrophobic and Superhemophobic Surface. *ACS Appl. Mater. Interfaces*, **9** (36), 31170–31180.

171. Shirtcliffe, N.J., McHale, G., Newton, M.I., Perry, C.C., and Pyatt, F.B. (2006) Plastron properties of a superhydrophobic surface. *Appl. Phys. Lett.*, **89** (10), 2005–2007.

172. Qu, M., Liu, S., He, J., Feng, J., Yao, Y., Hou, L., Ma, X., and Liu, X. (2016) Fabrication of recyclable superhydrophobic materials with self-cleaning and mechanically durable properties on various substrates by quartz sand and polyvinylchloride. *RSC Adv.*, **6** (82), 79238–79244.

173. Chaitanya, B., Gunjan, M.R., Sarangi, R., Raj, R., and Thakur, A.D. (2021) Per-fluorinated chemical free robust superhydrophobic copper surface using a scalable technique. *Mater. Chem. Phys.*, **278** (May 2021), 125667.

174. Martínez-Gómez, A., López, S., García, T., De Francisco, R., Tiemblo, P., and García, N. (2017) Long-Term Underwater Hydrophobicity: Exploring Topographic and Chemical Requirements. *ACS Omega*, **2** (12), 8928–8939.

175. THORPE, W.H. (1950) Plastron Respiration in Aquatic Insects. *Biol. Rev.*, **25** (3), 344–390.

176. Krumpfer, J.W., and McCarthy, T.J. (2011) Rediscovering silicones: “unreactive” silicones react with inorganic surfaces. *Langmuir*, **27** (18), 11514–11519.

177. Yang, C., Tartaglino, U., and Persson, B.N.J. (2006) Influence of surface

roughness on superhydrophobicity. *Phys. Rev. Lett.*, **97** (11), 1–4.

178. Ranjan, D., Zou, A., and Maroo, S.C. (2022) Durable and regenerative superhydrophobic surface using porous nanochannels. *Chem. Eng. J.*, **455** (September 2022), 140527.

179. Lv, C., Hao, P., Zhang, X., and He, F. (2016) Drop impact upon superhydrophobic surfaces with regular and hierarchical roughness. *Appl. Phys. Lett.*, **108** (14).

180. Khojasteh, D., Kazerooni, M., Salarian, S., and Kamali, R. (2016) Droplet impact on superhydrophobic surfaces: A review of recent developments. *J. Ind. Eng. Chem.*, **42**, 1–14.

181. Wei, Y., Qi, H., Gong, X., and Zhao, S. (2018) Specially Wettable Membranes for Oil–Water Separation. *Adv. Mater. Interfaces*, **5** (23).

182. Crafts, N. (2004) Steam as a general purpose technology: A growth accounting perspective. *Econ. J.*, **114** (495), 338–351.

183. Atack, J., Bateman, F., and Margo, R.A. (2008) Steam power, establishment size, and labor productivity growth in nineteenth century American manufacturing. *Explor. Econ. Hist.*, **45** (2), 185–198.

184. Ozaki, Y., Morisawa, Y., Ikehata, A., and Higashi, N. (2012) Far-ultraviolet

spectroscopy in the solid and liquid states: A review. *Appl. Spectrosc.*, **66** (1), 1–25.

185. Zhang, Y., Ravi, S.K., and Tan, S.C. (2019) Food-derived carbonaceous materials for solar desalination and thermo-electric power generation. *Nano Energy*, **65** (August), 104006.

186. Poudel, S., Zou, A., and Maroo, S.C. (2020) Evaporation Dynamics in Buried Nanochannels with Micropores. *Langmuir*, **36** (27), 7801–7807.

187. Ranjan, D., Zou, A.,and Maroo, S.C. Article Vapor generation via porous nanochannel wicks. *Cell Reports Phys. Sci.*, 100738.

188. Sartori, E. (2000) A critical review on equations employed for the calculation of the evaporation rate from free water surfaces. *Sol. Energy*, **68** (1), 77–89.

189. Zhou, L., Tan, Y., Ji, D., Zhu, B., Zhang, P., Xu, J., Gan, Q., Yu, Z., and Zhu, J. (2016) Self-assembly of highly efficient, broadband plasmonic absorbers for solar steam generation. *Sci. Adv.*, **2** (4).

190. Chen, C., Li, Y., Song, J., Yang, Z., Kuang, Y., Hitz, E., Jia, C., Gong, A., Jiang, F., Zhu, J.Y., Yang, B., Xie, J., and Hu, L. (2017) Highly Flexible and Efficient Solar Steam Generation Device. *Adv. Mater.*, **29** (30), 1–8.

191. Zhu, M., Li, Y., Chen, F., Zhu, X., Dai, J., Li, Y., Yang, Z., Yan, X., Song,

J., Wang, Y., Hitz, E., Luo, W., Lu, M., Yang, B., and Hu, L. (2018) Plasmonic Wood for High-Efficiency Solar Steam Generation. *Adv. Energy Mater.*, **8** (4).

192. Yang, P., Liu, K., Chen, Q., Li, J., Duan, J., Xue, G., Xu, Z., Xie, W., and Zhou, J. (2017) Solar-driven simultaneous steam production and electricity generation from salinity. *Energy Environ. Sci.*, **10** (9), 1923–1927.

193. Kim, S.M., and Mudawar, I. (2017) Thermal design and operational limits of two-phase micro-channel heat sinks. *Int. J. Heat Mass Transf.*, **106**, 861–876.

194. Guo, Z., Chen, Z., Shi, Z., Qian, J., Li, J., Mei, T., Wang, J., Wang, X., and Shen, P. (2020) Stable metallic 1T phase engineering of molybdenum disulfide for enhanced solar vapor generation. *Sol. Energy Mater. Sol. Cells*, **204** (September 2019), 110227.

195. Chen, H., Frankel, J.I., and Keyhani, M. (2017) Nonlinear inverse heat conduction: Digitally filtered space marching with phase-plane and cross-correlation analyses. *Numer. Heat Transf. Part B Fundam.*, **72** (2), 109–129.

196. HENDERSON-SELLERS, B. (1984) A new formula for latent heat of vaporization of water as a function of temperature. *Q. J. R. Meteorol. Soc.*, **110** (466), 1186–1190.

197. Minas, C., Carpenter, J., Freitag, J., Landrou, G., Tervoort, E., Habert, G.,

and Studart, A.R. (2019) Foaming of Recyclable Clays into Energy-Efficient Low-Cost Thermal Insulators. *ACS Sustain. Chem. Eng.*, **7** (18), 15597–15606.

198. Xu, N., Li, S., Li, Y., Xue, Z., Yuan, L., Zhang, J., and Wang, L. (2015) Preparation and properties of porous ceramic aggregates using electrical insulators waste. *Ceram. Int.*, **41** (4), 5807–5811.

199. Zhang, H., Fang, W.Z., Li, Y.M., and Tao, W.Q. (2017) Experimental study of the thermal conductivity of polyurethane foams. *Appl. Therm. Eng.*, **115**, 528–538.

200. Hanks, D.F., Lu, Z., Narayanan, S., Bagnall, K.R., Raj, R., Xiao, R., Enright, R., and Wang, E.N. (2014) Nanoporous evaporative device for advanced electronics thermal management. *Thermomechanical Phenom. Electron. Syst. -Proceedings Intersoc. Conf.*, 290–295.

201. Schonberg, J.A., DasGupta, S., and Wayner, P.C. (1995) An augmented Young-Laplace model of an evaporating meniscus in a microchannel with high heat flux. *Exp. Therm. Fluid Sci.*, **10** (2), 163–170.

202. Zheng, L., Plawsky, J.L., Wayner, P.C., and DasGupta, S. (2004) Stability and oscillations in an evaporating corner meniscus. *J. Heat Transfer*, **126** (2), 169–178.

203. Zou, A., Poudel, S., Gupta, M., and Maroo, S.C. (2021) Disjoining Pressure of Water in Nanochannels. *Nano Lett.*

204. Honschoten, J.W.V., Brunets, N., and Tas, N.R. (2010) Capillarity at the nanoscale. *Chem. Soc. Rev.*, **39** (3), 1096–1114.

205. Nazari, M., Davoodabadi, A., Huang, D., Luo, T., and Ghasemi, H. (2020) On interfacial viscosity in nanochannels. *Nanoscale*, **12** (27), 14626–14635.

206. Gardner, W. (1921) Note on the dynamics of capillary flow. *Phys. Rev.*, **18** (3), 206–209.

207. Tas, N.R., Haneveld, J., Jansen, H. V., Elwenspoek, M., and Van Den Berg, A. (2004) Capillary filling speed of water in nanochannels. *Appl. Phys. Lett.*, **85** (15), 3274–3276.

208. Tas, N.R., Mela, P., Kramer, T., Berenschot, J.W., and Van Den Berg, A. (2003) Capillarity Induced Negative Pressure of Water Plugs in Nanochannels. *Nano Lett.*, **3** (11), 1537–1540.

209. Gupta, M., and Maroo, S.C. (2022) Molecular dynamics simulation of bubble nucleation in hydrophilic nanochannels by surface heating. *Mol. Simul.*, **48** (15), 1356–1361.

210. Vanitha, V., Hemalatha, S., Pushpabharathi, N., Amudha, P., and

Jayalakshmi, M. (2017) Fabrication of nanoparticles using Annona squamosa leaf and assessment of its effect on liver (Hep G2) cancer cell line. *IOP Conf. Ser. Mater. Sci. Eng.*, **191** (1).

211. Kunjiappan, S., Chowdhury, R., and Bhattacharjee, C. (2013) Isolation and structural elucidation of flavonoids from aquatic fern Azolla microphylla and evaluation of free radical scavenging activity ISOLATION AND STRUCTURAL ELUCIDATION OF FLAVONOIDS FROM AQUATIC FERN AZOLLA. *Int. J. Pharm. Pharm. Sci.*, **5** (3), 743–749.

212. Ahmadizadeh Shendy, S., Babazadeh, M., Shahverdizadeh, G.H., Hosseinzadeh-Khanmiri, R., and Es'haghi, M. (2021) Synthesis of the quinazolinone derivatives using an acid-functionalized magnetic silica heterogeneous catalyst in terms of green chemistry. *Mol. Divers.*, **25** (2), 889–897.

213. Saravanan, S., and Dubey, R.S. (2020) Synthesis of SiO2 nanoparticles by sol-gel method and their optical and structural properties. *Rom. J. Inf. Sci. Technol.*, **23** (1), 105–112.

214. Javidparvar, A.A., Ramezanzadeh, B., and Ghasemi, E. (2016) Effect of various spinel ferrite nanopigments modified by amino propyl trimethoxy silane on the corrosion inhibition properties of the epoxy nanocomposites.

Corrosion, **72** (6), 761–774.

215. Tsamesidis, I., Lymperaki, E., Egwu, C.O., Pouroutzidou, G.K., Kazeli, K., Reybier, K., Bourgeade-Delmas, S., Valentin, A., and Kontonasaki, E. (2021) Effect of Silica Based Nanoparticles against Plasmodium falciparum and Leishmania infantum parasites. *J. Xenobiotics*, **11** (4), 155–162.

216. Sherstad, E.M. (1971) Use of Fluorescein To Measure the Composition of Waterdrop Splash. (4), 1020–1023.

Biography

Durgesh Ranjan is a Ph.D. Candidate in the Department of Mechanical and Aerospace Engineering at Syracuse University, NY. His research is focused on multiphase heat-transfer using micro/nano structured geometries. His research findings have been published in journals including Chemical Engineering Journal and Cell Reports Physical Science. He was born and brought up in India and completed his B.S. and M.S. in Mechanical Engineering from Cochin University and Indian Institute of Technology Patna, respectively. His research interest lies in the field of surface wettability and thermal management system. and He was the recipient of research excellence doctoral fellow for the year 2021-20222. He has won the First Prize Award for the best oral presentation during ECS research day 2022. A provisional patent has been granted for his innovation regarding a durable superhydrophobic surface. He is joining the University of Florida as a Postdoctoral Associate in March 2023. He plans to pursue his career in academia.